Alma Mater Studiorum · Università di Bologna

Dipartimento di Fisica e Astronomia
Dottorato di ricerca in Fisica
Ciclo XXVIII

Search for the $t\bar{t}H$ production in multi-leptonic final states with the ATLAS detector at LHC

Tesi Presentata da: **Federico Lasagni Manghi**

Coordinatore Dottorato:
Prof. Gastone Castellani

Relatore:
Chiar.mo Prof. Mauro Villa
Correlatore:
Dott. Antonio Sidoti

Settore Concorsuale di Afferenza: 02/A1

Settore Scientifico Disciplinare: FIS/01

Esame Finale - Anno 2016

Contents

Introduction

The Standard Model of particle physics is the most successful and comprehensive theory of the fundamental particles and forces ever conceived. With the discovery of the Higgs boson, by ATLAS and CMS in July 2012 that granted a Nobel Prize to P. Higgs and F. Englert, the model is complete in its self-consistent theoretical formulation. There are many indications, coming mainly from theory and cosmology, that there should be some mechanism beyond the Standard Model (SM) that might explain the characteristics of the observed universe and some puzzling results in particle physics. These SM extensions might become more and more important at higher energies, well beyond the TeV scale, where the experimental results are lacking and limited to cosmic ray studies. The Higgs and, in particular, the study of the Higgs couplings, is a privileged way to access these mechanisms and investigate some extensions of the Standard Model. The associated production $t\bar{t}H$ is extremely important in this context for several theoretical reasons.

The Large Hadron Collider is the only accelerator where this kind of study is possible, thanks to the unprecedented center-of-mass energy and interaction rate. The ATLAS experiment, built around one of the LHC interaction points, was conceived and built with the purpose of studying the products of the most interesting interactions.

At the Run I energy, $\sqrt{s} = 8\,TeV$, the $t\bar{t}H$ cross section is an order of magnitude below the inclusive Higgs production; the $L_{int} = 20\,fb^{-1}$ of data gathered by the ATLAS experiment in 2012 can provide a first experimental measurement of the cross-section. The higher (factor $\sim$4) cross section at the Run II energy of $\sqrt{s} = 13\,TeV$ allows for a similar result on the first $L_{int} = 3.3\,fb^{-1}$ gathered in 2015, in preparation for the main data-taking of 2016. This thesis is focused on the analysis chain and on the tools needed

to perform the $t\bar{t}H$ cross section measurement which, given the cross sections and the collected luminosity, will become statistically significant only on 2015-2016 ATLAS data. The thesis describes the analysis of the production of a Higgs boson in association with a top and anti-top quark couple and decay into multi-leptonic final states in ATLAS at LHC. The analysis is focused on the channel defined by two light leptons of the same sign and no hadronic tau leptons in both Run I and Run II. A large part of the thesis is dedicated to the data-driven estimation of the main background of this channel, fake leptons produced in meson decays, using a technique denominated *matrix method*. This method is an essential step for the differential and multi-variate analyses that will be performed later in Run II.

In the first chapter the Standard Model of particle physics is introduced. It starts by describing the fundamental particles and the field theories of Electromagnetic, Strong and Weak interactions and continues with a focus on the Electro-Weak symmetry breaking mechanism and the Higgs boson. It finishes introducing the theories beyond the Standard Model that have the strongest interaction with the Higgs.

In the second chapter the experimental set-up is described. In the first part the principles of particle acceleration, detection, identification and measurement are illustrated, focusing on High Energy Physics. In the second part the Large Hadron Collider and the ATLAS experiment are introduced, illustrating the structure of the detector, the sub-detectors and the acquisition and data-processing chain.

In chapter 3 the experimental search for the Higgs boson and the $t\bar{t}H$ production is explained. Starting with the description of the Higgs production at hadron colliders, its decay mechanisms and experimental signatures, it continues with a historical excursus on the direct and indirect searches for the Higgs boson and constraints on its mass, concluded with the discovery by ATLAS and CMS. In the end the $t\bar{t}H$ production in ATLAS, its properties and the results obtained in other analyses are described.

The fourth chapter describes the analysis of the Run I data at $\sqrt{s} = 8\,TeV$. I start from the signal and background simulations used to study the event topology and continue with the object selection and the experimental channel definition. The data-driven background estimation techniques are explained, with particular focus on the channel with two leptons of the same sign and no hadronic taus. A final comparison of the production

cross-section with the Standard Model is presented for each sub-channel and for their combination.

In chapter 5 the *matrix method* in the channel with two leptons of the same sign and no hadronic taus of the Run I analysis is described. The method is used to provide background shapes as a function of any kinematic or topological variable. In this case it is applied to the estimation of the signal region contamination due to leptons produced in hadron decays inside a particle jet. The theoretical frameworks and the different steps of the implementation are shown, together with the tests performed to reach an optimal estimation. Finally, the method is used to provide the total number of background events, used to produce a new analysis result.

Chapter 6 describes the analysis of the first Run II data acquired in 2015, underlining the differences with respect to Run I. The new implementation and optimization of the matrix method is explained in detail. At the moment of this writing the statistics available is not enough for a statistically sound measurement and therefore all the analysis has been performed to tune the tools and to evaluate the backgrounds only. The signal region is still locked in the blinded analysis.

Two appendices describe the work I carried out within the ATLAS to study and improve the detector performance. Appendix A describes my study of the luminosity measurement using Z boson counting, illustrating the analysis procedure, the luminosity measurement and the study of the luminosity systematic dependencies: on time and on the average number of interactions per bunch crossing. Appendix B describes the LUCID detector and its upgrade from Run I to Run II, focusing on the development of the firmware for the electronic boards, to which I contributed the most. In the end, the first results obtained with the LUCID in run II are shown.

Chapter 1

The Standard Model of Particle Physics

1.1 Introduction

The Standard Model of particle physics is, up to now, the most complete and predictive theory of subatomic scale phenomena. It was developed to include the Quantum Field Theories of three of the four known forces and their interaction with all known particles. The theory has a symmetry with the structure:

$$SU(3)_C \otimes SU(2)_L \otimes U(1)_Y \tag{1.1}$$

where $SU(2)_L \otimes U(1)_Y$ is the symmetry group associated with the electroweak theory and $SU(3)_C$ is the symmetry group associated with the strong interaction.
In this first chapter the basic concepts of the Standard Model are outlined. Firstly the definitions of fundamental particles and fields are introduced, then their characteristics are explained, from fermion families to vector and scalar bosons.
In the second part the main features of the gauge theories are illustrated. We start with Quantum Electro Dynamics, the modern formulation of electromagnetism that takes into account the Quantum Mechanics and Special Relativity Principles. After that, Quantum Chromo Dynamics is explained: the field theory approach to the strong interactions that

hold together the atomic nucleus. It describes how the fundamental components of nucleons, the quarks, interact with each other. In the last paragraph we introduce weak theory, the quantum field approach to the interaction first proposed by Fermi to explain β decay kinematics. The electroweak theory is, finally, outlined, a model developed from the unification of Quantum Electro Dynamics and the theory of weak interactions.
In the third section the Spontaneous Symmetry Breaking is introduced to explain the mass of the weak vector bosons and how this consequently gives rise to a new particle, the Higgs boson. After that, the Yukawa mechanism is outlined, where the interaction of the fermions with the Higgs boson grants them their mass. The characteristics of this new particle are, finally, explained, focusing in particular on its interaction with SM particles.

1.2 Fields and particles

In the Standard Model the fundamental entities are particles and fields. The definition of these entities has evolved in time and in particular through the early 20^{th} century. The first definition of a particle is that of a point-like fundamental object, while a field was defined as an entity of different type (scalar, vector or tensor) whose values were functions of the space-time coordinates [1], [2]. In Quantum Field Theory a particle is defined as any object that is invariant under Poincaré group transformations, which include all space and time transformations in the relativistic framework. This means that it is a well-defined object and that its properties do not depend on the framework of observation. A particle can be real or virtual. While a real particle can have a well defined lifetime, ranging from $10^{-32}s$ to infinite, a virtual particle is only allowed within the boundaries of the Heisenberg principle, that states that $\Delta t \Delta E \leq \frac{\hbar}{2}$. This means that in our experiments, where Δt goes to infinity in the final state, there cannot be energy excesses between initial and final states. For an unstable particle with a known mean lifetime τ, its mass is not exactly defined and can vary within the limits of the Heisenberg Uncertainty Principle. This is determined by the formula $\Gamma = \hbar/\tau$, where Γ is the full width at half height of the particle mass distribution and τ is its lifetime. When a particle is produced far from its nominal mass peak, it is called off-shell and

is marked with the symbol *. All of the known fundamental particles of the Standard Model are shown in figure 1.1.

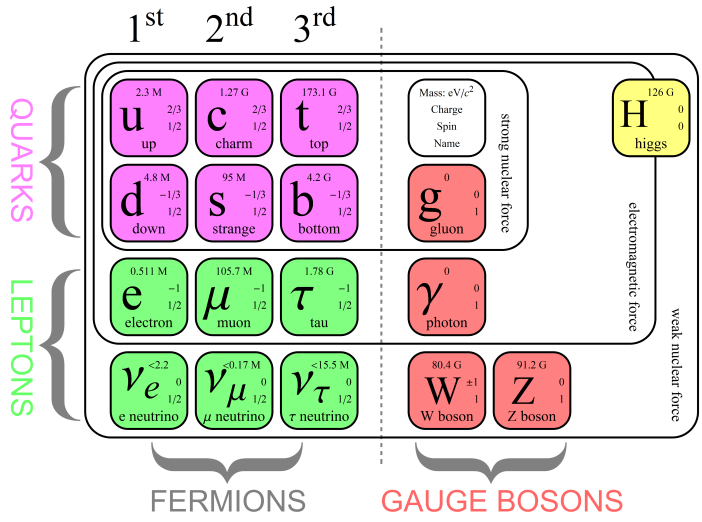

Figure 1.1: particles and fields of the Standard Model: fermions on the left and gauge bosons on the right. Fermions are also divided in leptons and quarks and organized in three families/generations

A first distinction between different kinds of particles arises from their spin, a quantum number that shares some properties with macroscopic angular momentum and is measured in quantized units of $\hbar$. Particles that have integer spin are called bosons because they respond to the Bose-Einstein statistics, meaning their states have completely symmetric waveforms; we distinguish between:

- scalar bosons, that have spin 0 (the only known fundamental one in the SM is the Higgs Boson); their free waveform is described by $(\Box + m^2)\phi = 0$;
- vector bosons, with a spin of 1, which are the carriers of the gauge interactions: γ (photons), $W^{\pm}$, Z and the eight G (gluons); their free wave function can be described by $(\Box + m^2)A_\mu = 0$ when $\partial^\mu A_\mu = 0$.

Since SM bosons are the mediators of the gauge interactions and the Higgs field, they are discussed in greater detail in the next paragraphs. Fermions are particles that present fractional spin $s = (2S + 1)/2$, in particular $s = \frac{1}{2}\hbar$ is characteristic of all known

fundamental fermions. They obey the Fermi-Dirac statistics, implying that they have an antisymmetric waveform, as described by the Dirac equation:

$$(i\gamma^{\mu}\partial_{\mu} - m)\psi = 0, \tag{1.2}$$

where $\partial_{\mu} = \frac{\partial}{\partial x_{\mu}}$ and γ^{μ} are the Dirac matrices [**?**]; the Dirac spinor ψ is usually separated into the left-handed and the right-handed spinors $\psi = \psi_L + \psi_R$, where R and L are the chirality of the particle. Chirality is equivalent to helicity, the projection of the spin along the direction of the movement, for massless particles; for massive ones it is a purely quantum value, with $\psi_R = \frac{1}{2}(1 + \gamma^5)\psi$. Every known fermion has an antimatter counterpart that shows similar characteristics but inverted charge and chirality. Fermions are divided into two different categories, based on their charge and interaction with the quantum fields: leptons and quarks.

Leptons

In the Standard Model we distinguish between charged, massive leptons and neutrinos. The most massive ones are the electrons, muons and taus; they all have the same charge and have a corresponding neutrino, a low mass fermion with charge 0 and the same *lepton number*. Charged leptons interact with the Electroweak force, while neutrinos only interact with the weak component. Due to this, their interaction probability with matter is very low and they cannot be efficiently detected by the high energy physics detectors described in this thesis.

The electron is the stable lepton that forms atoms and thus most of the known matter. Due to its low mass ($0.511\,MeV/c^2$) and charge, it looses a large amount of energy when it passes through matter (see chapter 2).

The muon is an unstable charged lepton, with a lifetime of $2.2\,\mu s$, that presents a greater mass than the electron ($105.7\,MeV/c^2$) and thus is less affected during its interaction with matter.

The tau is the heaviest of the known leptons ($1.78\,GeV/c^2$), characterized by a short lifetime ($2.9 \times 10^{-13}\,s$), so we can only observe its decay products in our detectors. In all the physical processes involving leptons, the three leptonic numbers (L_e, L_μ and L_τ) need to be conserved, considering that anti-particles have negative leptonic numbers.

For example the electron and its neutrino have $L_e = 1$, their anti-particles have $L_e = -1$ and all other leptons have $L_e = 0$. This means that a muon decay will produce a muon neutrino, an electron and an electron anti-neutrino, as shown in figure 1.2.

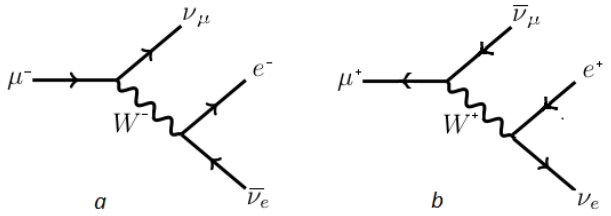

Figure 1.2: Muon (a) and anti-muon (b) weak decays. Lepton numbers $L_\mu = \pm 1$ and $L_e = 0$ are conserved in both processes.

Quarks

Quarks are the fundamental components of nucleons, their charge is a fraction of the fundamental electron charge and they interact with the strong force. They are divided into three families of increasing mass but otherwise similar properties. One of the essential properties of quarks derives from the Strong interaction: we cannot observe free quarks. We will expand on it in the next sections, but the main effect is that the quarks are always observed in composite states, called mesons ($q\bar{q}'$) and baryons ($qq'q$"). Examples of these states are the proton (uud), the neutron (udd)
The bottom (b) quark is the heaviest of the down-type quarks, with a mass of $4.2\,GeV/c^2$ and a lifetime of $\sim 10^{-12}\,s$. After hadronization it decays mainly into $b \to c + W$.
The most interesting quark for the scope of this thesis (and the ATLAS detector) is the top (t), for a series of reasons:

- it is the heaviest known particle ($M \sim 173\,GeV/c^2$) and thus has a large interaction with the Higgs field (end of chapter);
- it has a very short lifetime ($\sim 5 \times 10^{-25}\,s$), so it decays before hadronization, giving us access to the fundamental properties of naked quarks and strong interaction.

1.3 The Gauge Interactions

At the beginning of the 20^{th} century two fundamental interactions were known. These were gravity and electromagnetism, this last born from the unification of the electro-static force and the magnetic force. The Standard Model formulation starts with the integration of electromagnetism, special relativity and quantum mechanics, while attempts at including gravity in the same frame have been considered so far theoretically weak or inconsistent. In Quantum Field Theories any interaction is mediated by one or more particles that represent the quantized units of the classical force field. These are all vector bosons and every interaction has a number of them that depends of their group symmetries. The first interesting quantity that can be used to verify or falsify a theory in particle physics is the cross-section, the probability of observing a particular process given some fixed initial conditions.
As a general rule in High Energy Physics, the cross-sections of these theories are treated through a perturbative approach using Feynman diagrams [3]. This is not always true and we will treat these cases separately. Following Feynman's rules, we should draw all possible combinations of processes that from the initial condition give rise to the desired final states. Summing all these infinite contributions the exact cross-section can be computed:

$$\left(\frac{d\sigma}{d\Omega}\right) \propto \frac{1}{s}|\sum_{i}^{\infty} M_i|^2, \tag{1.3}$$

where $s = E_{CMS}^2$ and M_i is the sum of probability amplitude contributions of the diagrams at the same perturbative level i. These contributions are the product of the vertex and propagator contributions that compose it and are always complex numbers. When high order perturbations are small, we need to sum only the simplest diagrams, that give the largest contribution to cross-section. The probability amplitude M_i, in these cases, is proportional to $\sqrt{\alpha^n}$, where α is the coupling constant of the interaction and n is the number of vertices of the diagram. Since α_{EW} is always small for the electroweak interaction, the first order perturbative calculations are always a good first approximations, but this is not the case for the strong interactions, where $\alpha_S \sim 1$ at low energy scales.

Electromagnetic interaction

QED, Quantum Electro Dynamics, is the Field Theory of electromagnetism, the modern version of a theory that was developed through three centuries. It is based on a U(1) symmetry group, is mediated by a single vector boson, the photon, and interacts only with charged particles. This is described by the QED Lagrangian density (from here on referred to as just Lagrangian):

$$\mathcal{L}_{QED} = \bar{\psi}(i\gamma^{\mu}D_{\mu} + m)\psi - \frac{1}{4}F_{\mu\nu}F^{\mu\nu}, \tag{1.4}$$

where $D_{\mu} = \partial_{\mu} + ieA_{\mu}$ and $F_{\mu\nu}$ is the electromagnetic field tensor.
In the Feynman diagrams the free photon and fermion propagator is represented by figure 1.3.a and .b and corresponds to a contribution shown to the side. The simplest possible QED vertex is shown in figure 1.3.c and contributes to the cross-section as shown in the same figure.

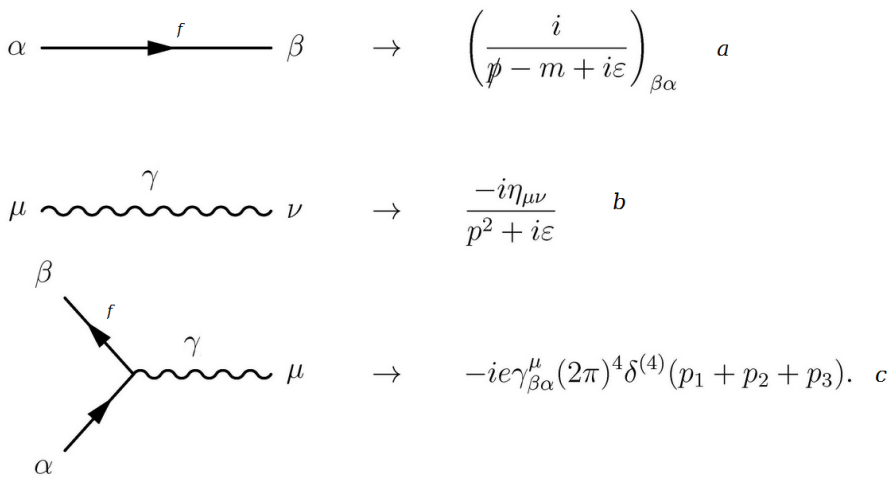

Figure 1.3: Fermion propagator (a), γ propagator (b) and QED vertex (c), with the factor with which they contribute to the coupling amplitude.

The value of $\alpha_{EM} = e^2 \sim 1/137$ at low energy, using $\hbar = c = 1$, is so low that the perturbative approach gives good results even at the first orders and makes QED the most precise physics theory in the history of mankind. An interesting feature of α_{EM} is that it depends off the interaction energy, growing as energy increases. This is due to the

effect called vacuum polarization that occurs in the proximity of the charges; here the electrostatic field polarizes the virtual quantum fluctuations of the vacuum, effectively screening the real charge of the particle.

Strong theory

The theory of strong interactions is born from the necessity to explain the nuclear forces that keep together the nucleus and the components of the nucleons despite the presence of electric charges of the same sign. In its most fundamental formulation, the Strong theory is called Quantum Chromo Dynamics (QCD), a gauge interaction based on a new quantum number, the "charge" of the interaction, the colour. Three possible values of colour can be associated to a quark, conventionally called red, blue and green, with the anti-particles carrying the opposite values. Each quark carries a colour, while the massless gauge vector bosons of the interaction, the gluons, carry two colour charges. Since these are the charges of the interaction, they are conserved in every process involving quarks and gluons and, as a particular property of the QCD, the charges must be exchanged in every interaction. SU(3) is the symmetry group for QCD, which gives rise to 9 different vector bosons: 8 from the possible colour combinations and a colour singlet, that does not interact with matter. The Lagrangian of the interacting theory can be summarized as:

$$\mathcal{L}_{QCD} = -\frac{1}{4}F^a_{\mu\nu}F^{a\mu\nu} - \bar{\psi}(\gamma^\mu D_\mu + m)\psi, \tag{1.5}$$

where $D_\mu = \partial_\mu + \frac{i}{2}\sqrt{4\pi\alpha_s}\lambda_a A^a_\mu$, A^a_μ are the gauge potentials of the theory, $F^a_{\mu\nu}$ are the gluon field tensors tensor and λ_a are the Gell-Mann 3×3 matrices of the SU(3) symmetry group. From this we get the vertices and propagators of the theory, shown in figure 1.4 with their cross-section contributions, where we define $g_s = \sqrt{4\pi\alpha_s}$. Thanks to the fact that gluons carry colour charges, we can see that some self-interacting vertices have appeared, giving rise to the peculiar properties of QCD: confinement and asymptotic freedom. Due to the interference between different vertex contributions, the value of α_S varies with the momentum transferred in the interaction. This is shown in the following formula valid at the first perturbative loop level:

$$\alpha_s(q^2) = \alpha_s(\mu^2)[1 + \frac{\alpha_s(\mu^2)}{12\pi}\log(\frac{-q^2}{\mu^2})(2n_f - 11N) + O(\alpha_s^2)], \tag{1.6}$$

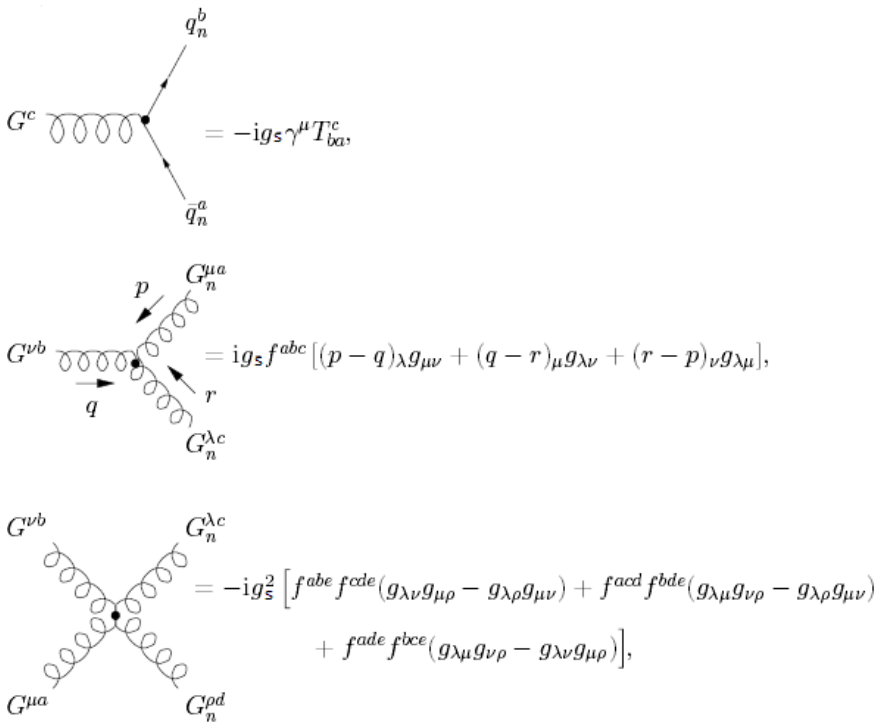

Figure 1.4: QCD vertices and their couplings

where μ^2 is some space-like re-normalization momentum point, n_f the number of quark flavours and N the number of colours. These last two terms represent the conflicting fermion and gluon loops, respectively (figure 1.5). When the value of $-q^2$ is low, $\alpha_S \sim 1$[1],

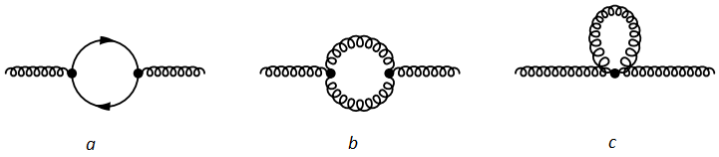

Figure 1.5: Lowest order QCD loops that affect the gluon propagator: a) fermion loop, b) and c) gluon loops

which means that, at long range, the theory is not perturbative any more and different approaches are necessary. At the same time, for isolated quarks and gluons the strength of the interaction increases with the distance. If the interaction potential energy becomes equal to the mass of a particle, that particle can become real, forming bound states called mesons and baryons, that are colour singlets and show only short-ranged ($\sim fm$) multipole interactions. Due to this, quarks and gluons are always observed in a bound state and the strong force on the nuclear scale can be described as mediated by the exchange of virtual mesons. On the other hand, the self-interaction vertices also cause the coupling constant to be reduced at high energy. This is called asymptotic freedom and makes the theory perturbative at high energies, such as those involved in HEP experiments.

Weak and Electroweak theory

The theory of weak interactions was born in the 30's to account for the 3-particle rare decays like the β decays. In the first formulation, developed by E. Fermi, the Matrix element of the interaction had the form:

$$M = \frac{G_F}{\sqrt{2}}[\bar{u_P}\gamma_\mu u_N][\bar{u_e}\gamma_\nu u_\nu], \tag{1.7}$$

where G_F is the Fermi constant. During the following years to the vectorial theory introduced by Fermi an axial component was added, that explained the flavour changing

[1]This happens when $q^2 \sim 1\,GeV$

processes. Starting from 1961, the theory was completed by Glashow, Weinberg and Salam [4], who unified it with the Quantum Electro Dynamics into the Electroweak theory. To do this they introduced a connection between electric charge Q, the third component of the weak isospin T_3 and the weak hypercharge Y, invariant for gauge transformations SU(2) and U(1). The free Lagrangian of the interaction of the weak and electromagnetic fields can be written as the sum of the one related to the scalar U(1) field B_μ and the three SU(2) vector fields $W_{i\mu}$.

$$\mathcal{L} = -\frac{1}{4} F^i_{W\mu\nu} F^{i\mu\nu}_W - \frac{1}{4} F_{B\mu\nu} F^{\mu\nu}_B, \tag{1.8}$$

with the tensor fields defined as usual:

$$F^i_{W\mu\nu} = \partial_\mu W^i_\nu - \partial_\nu W^i_\mu + g\epsilon^{ijk} W_{j\mu} W_{k\nu}, \tag{1.9}$$

$$F_{B\mu\nu} = \partial_\mu B_\nu - \partial_\nu B_\mu, \tag{1.10}$$

where ϵ^{ijk} is the Levi-Cita symbol. The components 1 and 2 of the W triplet are combined to get $W^\pm_\mu = \frac{1}{2}(W^1_\mu \mp W^2_\mu)$, while the B and W_3 are rotated by the so-called Weinberg angle θ_W to generate the EM vector potential and the neutral weak vector potential Z:

$$A_\mu = B_\mu \cos\theta_W + W^3_\mu \sin\theta_W, \tag{1.11}$$

$$Z_\mu = -B_\mu \sin\theta_W + W^3_\mu \cos\theta_W, \tag{1.12}$$

From this arise the weak vector bosons, W and Z, and it becomes clear that the electromagnetism is only a different, massless expression of the same interaction. The "weakness" of the interaction is thus explained by the propagator of the vector bosons that differs form the QED for the mass of the vector boson: figure 1.3. This explains how the

$$\overset{Z}{- - - - - - - - \rightarrow} \quad \rightarrow \frac{-i(\eta_{\mu\nu} - q_\mu q_\nu / M^2}{q^2 + M^2}$$

Figure 1.6: Massive vector boson propagator

coupling constant of an interaction that does not take into account the massive vector boson becomes very low at low energies, $G_F/\sqrt{2} = g^2/8M^2_W$. Several possible vertices

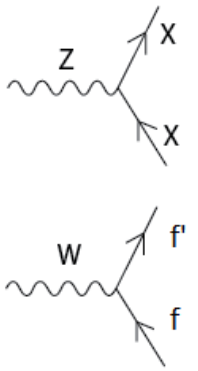

$$\rightarrow i(v_X + a_X\gamma^5)\gamma^\mu \qquad a$$

$$\rightarrow ig_w(1+\gamma^5)\gamma^\mu \qquad b$$

Figure 1.7: The Z and W vertices that couple to fermions with their cross-section ampitude contributions. Here g_w is the W coupling, v_X is the vectorial Z coupling constant and a_X is the axial Z coupling constant

arise from the electroweak interaction: the most relevant ones are shown in figure 1.7 together with their cross-section contributions. Among the peculiar properties of weak interaction, there is the quark mixing, a mismatch between the quarks that respond to the weak interaction and those that respond to the strong interaction. For the purposes of the weak interaction, the quarks are a mix of different families, as shown in the Cabibbo-Kobayashi-Maskawa matrix, that conventionally considers down-type quarks to mix:

$$\begin{pmatrix} d & s & b \end{pmatrix} = \begin{pmatrix} c_{12}c_{13} & s_{12}c_{13} & s_{13}e^{-i\delta_{13}} \\ -s_{12}c_{23} - c_{12}s_{23}s_{13}e^{i\delta_{13}} & c_{12}c_{23} - s_{12}s_{23}s_{13}e^{i\delta_{13}} & s_{23}c_{13} \\ s_{12}s_{23} - c_{12}c_{23}s_{13}e^{i\delta_{13}} & -c_{12}s_{23} - s_{12}c_{23}s_{13}e^{i\delta_{13}} & c_{23}c_{13} \end{pmatrix} \begin{pmatrix} d \\ s \\ b \end{pmatrix} \tag{1.13}$$

where we can find 3 mixing angles and a phase δ. The consequence of the Matrix is that there are preferred decays between quarks, as exemplified in figure 1.8.

Up to now we have only considered the interaction of the weak vector bosons with fermions, but there is nothing in the theory that forbids the existence of self-interacting vertices. This leads to an alteration of the effective interaction that would make it diverge. Under certain conditions, the Higgs mechanism cancels this contribution, as we will see in the next section.

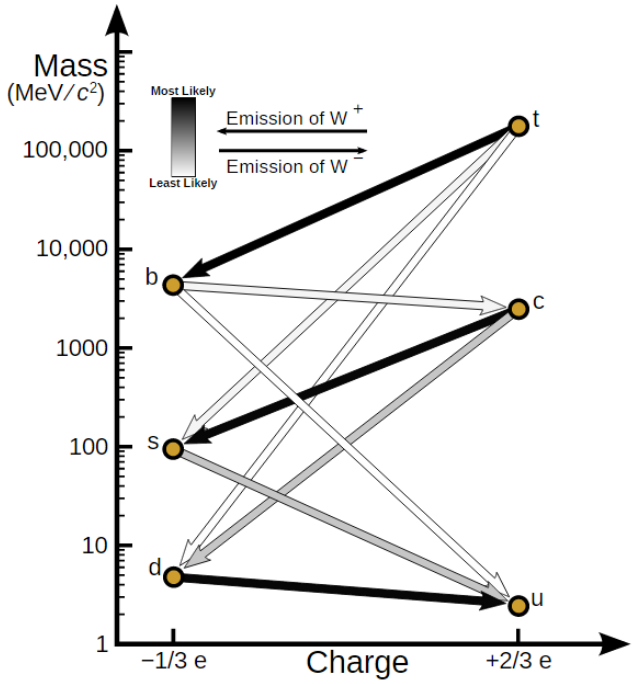

Figure 1.8: Since the CKM matrix has low non-diagonal values, decays tend to follow the $t \to b \to c \to s \to u$ chain, but there is a non-0 chance of mixed decays.

1.4 the Higgs mechanism

The mass of the gauge bosons

Since the first formulations of the EW theory, it became clear that the gauge bosons $W^{\pm}$ and Z needed a mass to explain the behavior of the effective potential previously used to describe the interaction. In the EW Lagrangian, though, non-dynamic mass terms in the form $M_Z^2 Z_\mu Z^\mu$ would violate the gauge invariance $SU(2)_L \times U(1)_Y$ and be non-renormalizable at high energy. To solve these problems, dynamic mass terms can be introduced by adding more scalar fields. If the Lagrangian of a theory possesses a symmetry, but its physical vacuum state does not, the symmetry is said to be spontaneously broken. In Quantum Field Theory, in case of broken continuous symmetries, the Nambu-Goldstone theorem [5] predicts the existence of N massless and spinless particles, where N = number of broken symmetries. These particles, called Goldstone bosons, can become part of the gauge bosons providing them new degrees of freedom. This translates in the gauge bosons acquiring a new longitudinal polarization, which is directly correlated to its mass. In figure 1.9 the interaction with the Goldstone bosons from the paper by Brout and Englert [6] is shown. In the simple U(1) case, this is accomplished

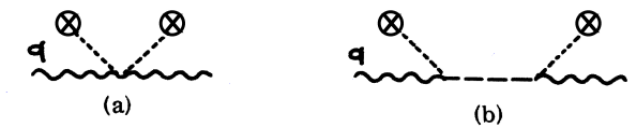

FIG. 1. Broken-symmetry diagram leading to a mass for the gauge field. Short-dashed line, $\langle\varphi_1\rangle$; long-dashed line, φ_2 propagator; wavy line, A_μ propagator. (a) $\rightarrow (2\pi)^4 ie^2 g_{\mu\nu}\langle\varphi_1\rangle^2$, (b) $\rightarrow -(2\pi)^4 ie^2(q_\mu q_\nu/q^2) \times\langle\varphi_1\rangle^2$.

Figure 1.9: Brout-Englert original paper

by adding to the Lagrangian a complex scalar field $\phi = \frac{1}{\sqrt{2}}(\phi_1(x) + i\phi_2(x))$ in the form:

$$V = \mu^2|\phi^2| + \lambda|\phi|^4, \tag{1.14}$$

where μ and λ are real parameters. This vacuum state can now have different shapes depending on the sign of μ^2. In the case $\mu^2 > 0$ the symmetry of vacuum potential

remains unbroken. To break the vacuum state symmetry we need $\mu^2 < 0$. The effect of this can be shown in a three-dimensional representation as in figure 1.10. The shape formed by the potential is called "Mexican hat" and ensures that the vacuum fundamental state, the lowest energy one, is degenerate. This way the U(1) gauge symmetry is

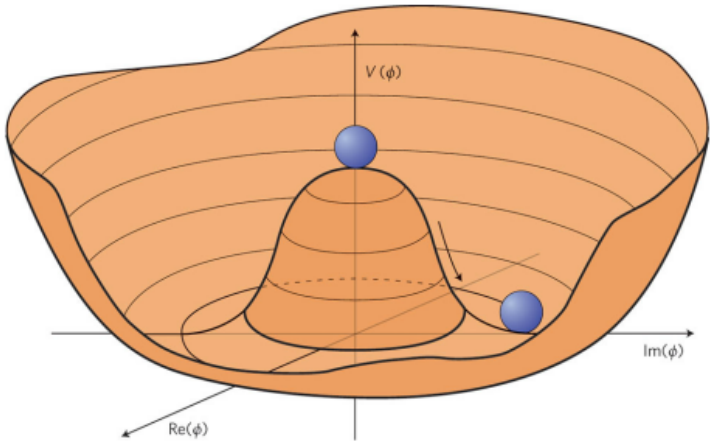

Figure 1.10: "Mexican hat" vacuum potential. The ground state is degenerate, breaking the EW symmetry.

spontaneously broken. We can parametrize ϕ as

$$\phi = \frac{v+h}{\sqrt{2}} e^{i\frac{\chi}{v}}, \tag{1.15}$$

where h and χ are called the Higgs boson [7] and the Goldstone boson. By choosing a particular gauge, called unitary gauge $A_\mu \to A_\mu - \frac{1}{ev}\partial_\mu \chi$, the Lagrangian becomes:

$$\mathcal{L} = -\frac{1}{4} F_{\mu\nu} F^{\mu\nu} + \frac{q\nu}{2} A_\mu A^\mu + \frac{1}{2}\partial_\mu h \partial^\mu h - \mu^2 h^2 + O(...) \tag{1.16}$$

The Goldstone boson χ has completely disappeared from the theory giving the "photon" a longitudinal polarization and a mass. Another, complementary, way to interpret this is to imply that the Goldstone bosons would be there if the gauge bosons had no mass and longitudinal polarization and we would be able to observe them. This Lagrangian now describes a theory with a photon of mass $m_A = qv$ and a scalar Higgs boson h with $m_h = \sqrt{2}\mu = \sqrt{2}\lambda v$. In the case of the Standard Model it is necessary to add a complex

SU(2) doublet of scalar fields of hypercharge Y = 1 and accomplish the spontaneous breaking of the gauge symmetry. This consists in choosing a particular ground state, around which the Higgs field $\Phi(x)$ is expanded. In this case, the particular vacuum chosen is $\Phi_0 = \begin{pmatrix} 0 \\ v \end{pmatrix}$ and the expanded form becomes:

$$\Phi = \begin{pmatrix} 0 \\ v + h(x) \end{pmatrix}, \tag{1.17}$$

that is invariant under $SU(2)_L \times U(1)_Y$ transformations but breaks the two separately. Since the doublet has no colour charge, the Strong sector is not affected. After a few manipulations the bosonic components of the Electroweak + Higgs Lagrangian can be summarized as:

$$\begin{aligned} \mathcal{L} = \frac{1}{2}\partial_\mu h \partial^\mu h - \mu^2 h^2 &\rightarrow h \\ -\frac{1}{4}W^i_{\mu\nu}W^{i\mu\nu} + \frac{g^2v^2}{4}W_{i\mu}W^{i\mu} &\rightarrow W \\ -\frac{1}{4}Z_{\mu\nu}Z^{\mu\nu} + \frac{g^2v^2}{4\cos^2\theta_w}Z_\mu Z^\mu &\rightarrow Z \\ -\frac{1}{4}F_{\mu\nu}F^{\mu\nu} &\rightarrow \gamma \end{aligned}$$

where the mass of the SM bosons is expressed by the second term in each line and the photon is massless. The mass of the W boson is then $m_W = vg/2$ and $m_Z = vg/2\cos\theta_w$. On the contrary, since λ is a free parameter of the theory, it is not possible to foresee the mass of the Higgs boson from the knowledge of the coupling constants or other known parameters.

The Yukawa coupling

In the Lagrangians seen up to now, no term expressing the mass of the fermions can be observed. To introduce this mass term, a Yukawa coupling needs to be implemented, adding the Lagrangian

$$\mathcal{L}_Y = -G_l[(\bar{l}_L\Phi)l_R + \bar{l}_R(\Phi^\dagger l_L)] \tag{1.18}$$

to the SM Lagrangian, expressing the coupling of the Higgs doublet with $\bar{l}_L l_R$. By explicitly inserting the Φ doublet as in expression 1.4, this becomes

$$-\frac{G_L}{\sqrt{2}(v\bar{l}l + l\bar{l}h)}, \tag{1.19}$$

where the fermion mass can be explicitly shown defining $m_l = G_l v/\sqrt{2}$: This expression is valid for leptons and down-like quarks, while for up-type quarks it is necessary to use a different doublet, defined as $-i\tau_2\Phi$.

The Higgs boson

In this chapter a new scalar boson was introduced in the EW symmetry breaking mechanism, called the Higgs boson. An essential point of the mechanism is that the introduction of the new particle solves the EW divergences at high energy by introducing new vertices: hWW, hZZ and hff. The couplings of these diagrams must have exactly the values show in figure 1.11, at tree level, for the SM to be consistent. Since the Higgs

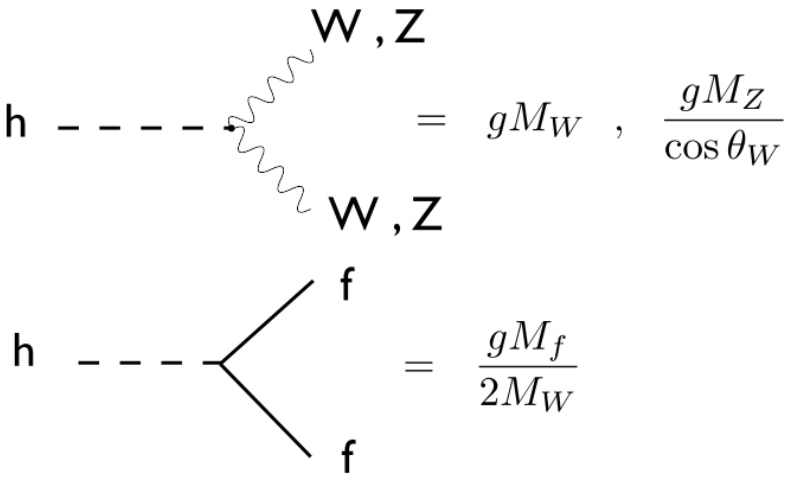

Figure 1.11: Higgs boson vertex couplings to W, Z and fermions

boson is responsible for the mass of the other particles, the strength of the interaction with them must depend on their mass. It is particularly interesting to notice that the theory can again be interpreted inversely: introducing a virtual Higgs field that couples

with particles grants them a mass proportional to the coupling.
The discovery of a new particle with the main features of the Higgs boson, by ATLAS and CMS in July 2012 [8], has shifted the focus of the Higgs studies to confirming all the properties and couplings expected by the theory.

1.5 Beyond Standard Model

The Standard Model is a highly successful theory that gives good predictions of what happens in High Energy Physics and at particle level in general. This is true on the energy scales that we can reach in the most modern accelerators and in the most frequent phenomena, but there is a number of problems that are hard to face with the current formulation of the Standard Model:

- above the known scales, the Higgs coupling corrections diverge and give infinite results;
- astrophysical phenomena unexplained by current models have been observed, like galactic rotation gradients and accelerated universe expansion; the theories of dark matter, inflation and dark energy have been proposed to explain these phenomena;
- neutrino oscillations have been confirmed, implying a non-zero neutrino mass, a result outside the SM;
- the gravitational interaction and general relativity are not taken into account in the model;
- reasons for the values of physics constants, the number of lepton families and the reason why certain mechanisms (such as CP violation) exist are all still unknowns of the theory;
- the strengths of the four interactions are very different from each other and the reason for this is unknown, as well.

Due to these issues, the Standard Model needs to be expanded or improved. For the purposes of this thesis, only the first two phenomena are treated. Several proposals have

been advanced over the years, but in this thesis we are mainly interested in how these theories are correlated to the Higgs sector.

The hierarchy problem

The spontaneous symmetry breaking mechanism through which particles acquire their mass is valid in perturbation theory at tree level, where only the simplest diagram is accounted for. Considering higher order diagrams, such as one-loop diagrams, a correction to the fermionic mass is necessary [9], as shown in figure 1.5 The mass of the fermion

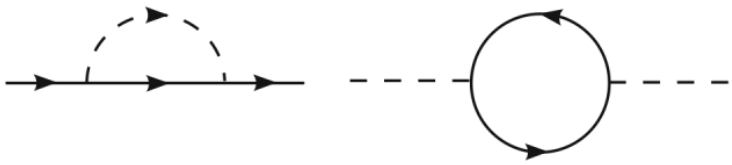

Figure 1.12: Lowest level loop corrections to the Higgs-fermion coupling and consequently to the mass

computed as: $m_f = m(0)_f + \delta m_f$, where $m(0)_f$ is given by the Higgs mechanism and the additional term

$$\delta m_f = -\frac{3\lambda_f^2 m_f}{64\pi^2} \log \frac{\Lambda^2}{m_f^2} + .. \tag{1.20}$$

depends on the introduction of a cut-off parameter Λ to the theory, ignoring additional terms that diverge when $\Lambda \to \infty$ or are independent on Λ. Just like for fermions, the scalar particle mass has to be corrected to account for the scalar-fermion loop terms, as shown here:

$$\delta m_h = \frac{\lambda_f^2}{8\pi^2}[\Lambda^2 - 6m_f^2 \log \frac{\Lambda}{m_f} + 2m_f^2 + ..], \tag{1.21}$$

quadratically divergent with the cut-off Λ. Since the Higgs boson discovered in 2012 has a mass of $M_H \sim 125\,GeV$, these quadratic divergences would indicate a large problem: corrections should be of the order of the Plank scale, if we assume the theory is valid up to those energies, well above the mass itself at the lowest perturbative order. A counter term to cancel these quadratic divergences could solve the problem, but such large cancellations would be highly unnatural. The cut-off could otherwise be adjusted

down to $\sim 1\,TeV$, but that would mean the theory ceases to be valid above this energy scale. This is called the hierarchy problem and points to new physics above the TeV scale. A possible solution to this problem could lie in Super Symmetry (SUSY) [10], a set of models that extend the SM by introducing a new discrete symmetry related to spin. To each $\frac{1}{2}\hbar$-spin fermion corresponds a 0-spin particle, thus a boson, called sfermion, to every gauge boson corresponds a $\frac{1}{2}\hbar$-spin particle called gaugino and to the Higgs boson h an additional 0-spin Higgs H and two higgsinos ($s = \frac{1}{2}\hbar$) are added. SUSY models would explain the spin structure of the particles we observe, but could also solve the Hierarchy problem by giving counter-terms to the SM divergences, ensuring renormalization up to the Plank scale.

Astrophysical considerations

Impressive advancements in astrophysics in the last twenty years have changed dramatically the way we see the universe. Recent analyses combining galaxy cluster dynamics, supernova data and precise measurements of the Cosmic Microwave Background radiation have given us a deeper insight on the composition of the universe. The large-scale structure of the universe is apparently incompatible with the measured mass (atoms and neutrinos) and energy (photons and neutrino kinematic energy) by a significant factor. Apparently, the observable matter contributes only by 5% to the total energy and matter of the universe: 95% of the universe is of unknown origin. Estimates done using galaxy cluster rotation, for example [11, 12], reveal that 23% of the universe could be justified by some form or dark matter that does not couple with electromagnetism. The remaining 72% of he universe is generally attributed to Dark Energy, an unknown form of energy responsible for the accelerated expansion of the universe. This composition should be found also in particle physics. Dark Matter, in particular, should be explained in Quantum Field Theory and observed experimentally. Among the proposed candidates for Dark Matter, two are particularly interesting: WIMPs (Weakly Interactive Massive Particles) and Axions. The first are massive particles, generally around the TeV scale, that interact only gravitationally and weakly, thus being very hard to observe. A possible candidate for this role is some kind of massive or sterile neutrino that cannot be observed by the normal neutrino detectors. On the other hand, there are other theories

that go beyond the Standard Model that could provide Dark Matter candidates. The most interesting is, again, Super Symmetry, in which some of the new foreseen particles, neutralino and gravitino, would have most of the required characteristics of WIMPs. The Axion, on the other hand, is a product of the Peccei and Quinn theory [13] elaborated to solve the strong CP violation problem.

Searches in the Higgs sector

There is a large number of models that try to solve the issues of the Standard Model. Most of these include new massive particles, beyond the TeV scale. Since coupling with the Higgs depends on the mass of the particles, this is a privileged channel to search for new phenomena. This could be a direct search, like $pp \to X+Y \to X+hh$ resonances, or an indirect search, looking for discrepancies in Higgs couplings, with theory and between different production processes. For the purposes of this thesis, indirect searches in the Higgs sector are the most interesting. Assuming a large new physics scale, $\Lambda \times m_W$, we can write: $\mathcal{L}_{eff} = \mathcal{L}_{SM} + \sum_i \frac{c_i}{\Lambda^2} O_i$, where O_i can be any process that deviates from the Standard Model. Using dimension-six operators there are several possible deviations from the SM that involve in the final states only known particles and are valid for any kind of Beyond Standard Model (BSM) process that involves massive particles. In what follows we show some of these operators and the processes they would influence [14]:

$$|\Phi|^2 G^i_{\mu\nu} G^{i\mu\nu} \to GG \to h \tag{1.22}$$

$$|\Phi|^2 B_{\mu\nu} B^{\mu\nu} \to h \to \gamma\gamma \tag{1.23}$$

$$|\Phi|^2 W^i_{\mu\nu} W^{i\mu\nu} \to h \to Z\gamma \tag{1.24}$$

$$|\Phi|^2 |D\mu\Phi|^2 \to h \to VV^* \tag{1.25}$$

$$|\Phi|^6 \to GG \to hh \tag{1.26}$$

$$|\Phi|^2 \bar{f}_L \Phi f_R + h.c. \to GG \to t\bar{t}h \tag{1.27}$$

The last process is of particular interest for this thesis, since it affects the $t\bar{t}h$ associated production. In addition to these, there are effects that on the vacuum, $\phi = v$, give a redefinition of the SM couplings but could still affect Higgs physics.

Conclusions

In chapter 1 we reviewed the main features of the Standard Model of particle physics and its last addition, the EW symmetry breaking sector that gives mass to weak vector bosons and fermions. This introduced a new particle, the Higgs boson, and we have seen that its interaction with fundamental particles is bound to their mass. This makes it a very interesting instrument to investigate theories that go beyond the SM and predict new massive particles. In the next chapter we will introduce the instruments used to study the SM, to search for the Higgs boson and to study its properties, gaining access to Beyond SM physics.

Chapter 2

The experiment: LHC and ATLAS

2.1 Introduction

Experimental evidence is the first and most essential component of the process of discovering the fundamental laws of our universe. Setting up a High Energy Physics experiment is a complex, challenging and expensive task. The first step consists in accelerating common particles into focused beams and making them collide on each other or on a fixed target. In the collision point every kind of physics process occurs, producing both stable and unstable particles. Unstable ones decay into stable products within a very short time, leaving only long-living particles in the final state. Around the interaction point the detector is built, detecting the passage of most particles produced in the interaction and measuring their kinematic properties. In the first section of this chapter we illustrate the basic principles of particle acceleration, particle detection, reconstruction and identification. In the following sections the Large Hadron Collider (LHC) and the main components of the ATLAS experiment are detailed, focusing in particular on those that are used in the analysis.

2.2 Particle acceleration, detection and identification

2.2.1 Particle acceleration

To study the most fundamental laws of nature it is necessary to achieve very high energies [15], [2]. This is due to two physical properties:

- The De Broglie relation. Quantum physics objects show both particle and wave properties, that are related by the equation $\lambda = h/p$, where p is the particle momentum. To interact with the smallest components of matter, particle or radiation probes need to have comparable (or smaller) wavelengths, thus requiring higher energies.

- Einstein's relation. In special relativity energy and matter are bound by the equation $E = mc^2$; this means that to produce (and thus observe) massive new particles from small, stable ones, an energy greater than its mass is necessary in the center of mass frame.

The basic components of a HEP accelerator are the source, the vacuum tube, the accelerating components and, possibly, the magnetic system.
Since acceleration is accomplished through the electromagnetic interaction, only charged particles can be accelerated. Thus the source needs to either be ionized gas or some electron emitter. Some accelerators can produce collisions of anti-particles and neutral particles, too. This is accomplished not by having a source of these, but rather by having charged particles collide with a fixed target and the products selected and/or accelerated afterwards. The Large Hadron Collider is a proton and ion accelerator, so the source is ionized gas.
During every acceleration step, the particles need to remain in good ($\sim 10^{-10} torr$ at LHC) vacuum not to loose energy and focus interacting with the gas medium. Several important effects need to be taken into consideration when building the vacuum tube of a high energy accelerator: mechanical and thermal behaviour, weight, toxicity, cost and evaporation under vacuum pressure, essential to have a clean vacuum. Even the passage of charged particles themselves could lead to out-gassing from the tube walls induced by synchrotron radiation or ions impacting on the walls. The emitted particles can be

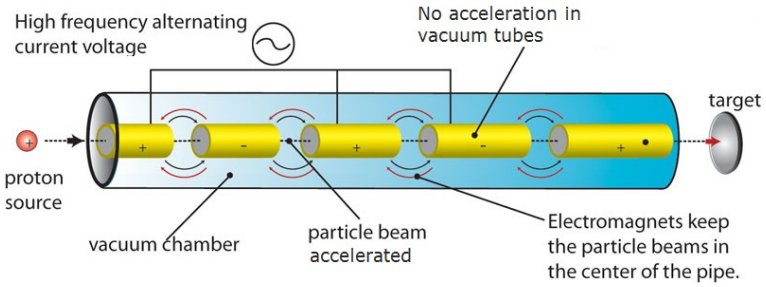

Figure 2.1: Basic princple of linear accelerators: ion packats are accelerated.

partially accelerated and lead to secondary interactions with the detector, increasing the background noise.

Three main accelerating techniques have been developed in this field. Electro-static acceleration consisted in placing the ion source close to the source of electrostatic fields and letting them be accelerated away from it. The final energy achieved could at most be $E = Vq$, where V is the electrostatic potential and q the charge of the particle. Some improvements lead to an increase of this energy by small factors over the years.

Linear and circular accelerators were afterwards developed to further rise the achievable energy. In linear accelerators, the beams of charged particles are divided into tight packets, called bunches, and accelerated through alternatively charged tubes. Since the acceleration is limited by the length of the accelerator, every tube needs to be conceived to transfer the maximum possible impulse to the particles. To accelerate multiple packets and take into account the increasing speeds of the particles along the accelerator, the charged tubes need to have variable distances and lengths, as shown in figure 2.1.

The basic principle of circular accelerators is that a small ΔV can be used multiple times to accelerate the bunches. To do that, a magnetic field bends their trajectory into a circular one, as for the Lorentz force $\vec{F} = \vec{v} \times \vec{B}$. The first example, invented by Lawrence in 1930, was the cyclotron, where a single magnet covers all the accelerating area. As the speed of the particles grows, their trajectories becomes larger, but their rotation phase remains the same, allowing for continuous bunch injection and acceleration. When relativistic effects become significant, this synchronization at different energies is lost. And two possible solutions have been developed: the synchrotron and the synchro-cyclotron. The latter simply changes the accelerating frequency of a typical cyclotron design. Of

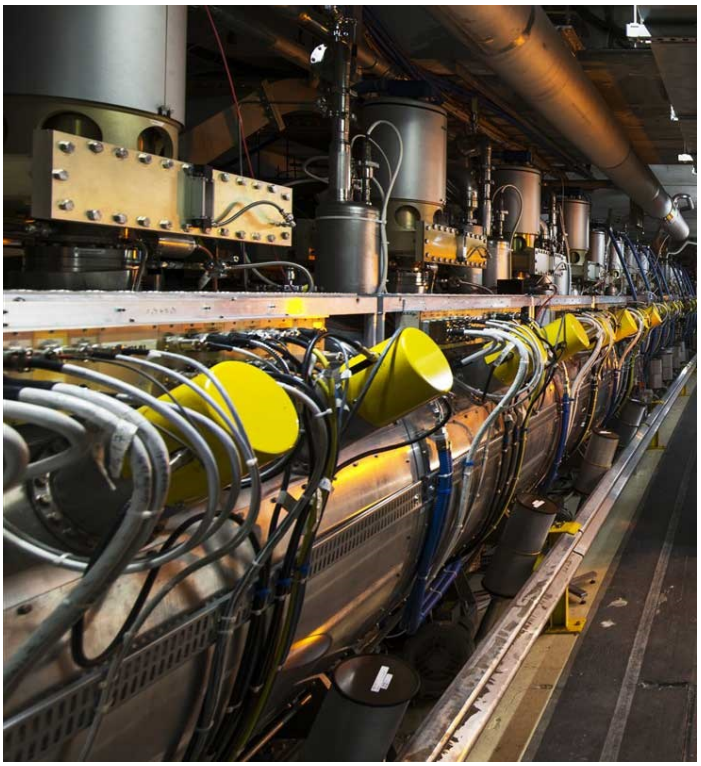

Figure 2.2: LHC radiofrequency cavities

far wider usage is the synchrotron design, which the LHC belongs to and has been most used over the last 60 years.
The synchrotron is a ring-shaped accelerator where several magnets curve the trajectory of the charged particles. These are injected together, so they all have the same energy. In short, straight parts of the ring, the accelerating devices, called radio-frequency cavities, give a small energy boost to the passing particles. LHC accelerating cavities are shown in figure 2.2. To be accelerated, particles need to be in phase with the cavities, but small phase variations are recovered by their design, slowing down faster ones and further accelerating slower ones. This is the Synchrotron oscillation, a periodic longitudinal variation of particle position, and energy, around their bunch.

The magnetic system is a vital component of circular accelerators. It has two main functions: bending and focusing beams. The importance of bending has already been discussed, enabling synchrotrons to reach a maximum momentum $|p| \propto BR$, but focusing

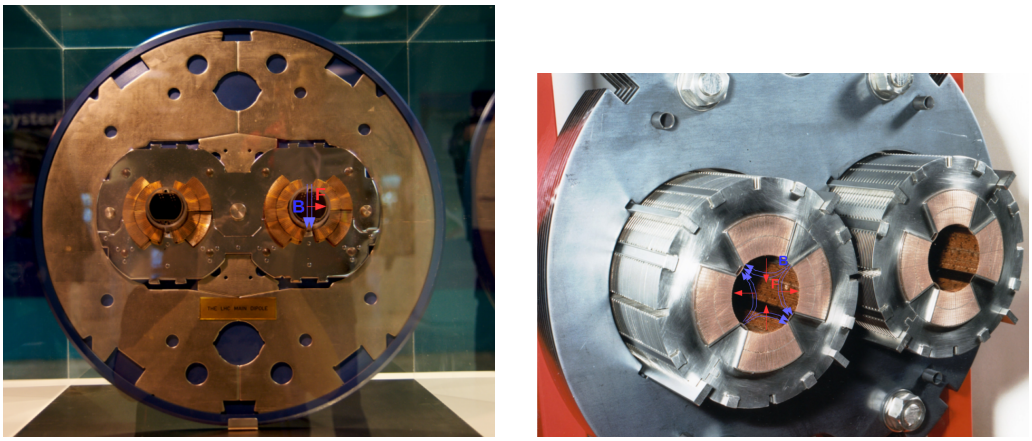

Figure 2.3: LHC dipole (a) and quadrupole (b) magnets. Dipole magnets influence every particle, exerting a force towards the center of the accelerator. Quadrupole magnets influence particles out of the beam axis, focusing them in a direction and defocusing in the perpendicular one.

is just as important for several reasons:

- charged particles tend to spread due to Coulomb repulsion;
- the source has an initial thermal energy that results in particle scattering;
- the beam interacts with the beam-pipe;
- to obtain maximum beam density in the interaction point.

At the beginning of particle acceleration, focusing was accomplished with the very same magnets used for bending: by using variable shapes and intensities of the fields it is possible to achieve a weak focus. On the other hand, separate quadrupole focusing is much more powerful. Figure 2.3 shows the mechanics of dipole (a) and quadrupole (b) magnets. Higher multi-pole systems are used for different purposes. The correcting effect of focusing on particles leads to the Betatron oscillation, a periodic axial variation of particle position around the beam axis.

A distinctive limiting factor of circular colliders is the Synchrotron radiation: a particle bent in some direction can emit high energy γ radiation along its trajectory, leading to

energy loss. The power loss in a circular accelerator depends on the relativistic γ_R of the particle:

$$P = \frac{2}{3}\frac{e^2 c}{4\pi\epsilon_0}\frac{\beta^4\gamma_R^4}{r^2}, \tag{2.1}$$

where $\gamma = E/m_0$, e is the charge of the particle, ϵ_0 the electric void conductivity and r is the curve radius. Since $E = \gamma_R mc^2$, at a given energy this effect depends from the mass of the particle. At LEP [16], an $e^+ e^-$ collider, the energy loss per revolution was $\Delta E \sim 2\,GeV$, while at LHC, in the same tunnel, the loss is $\Delta E \sim 4\,keV$. this energy loss turns out to be one of the main limiting factors of electron colliders.

2.2.2 Detecting particles

The human eye is the most essential component of our perception ability and thus the main input for the analysis process that takes place in the human brain. It is sensitive to light, photons, in a limited range of frequencies, making it totally inapt at detecting fundamental particles in all possible energy ranges [17] [18] [2]. Detectors transform particles into signals that can be processed by human beings and to do this they exploit the different ways particles interact with matter. In the final states of any high-energy collider process there are only a few observable objects that reach the detectors: $e^{\pm}$, $\mu^{\pm}$, γ, νs and hadrons. The way these interact with matter shall be briefly outlined in what follows.
Charged objects mainly react with the medium they cross in several ways, loosing variable amounts of energy in the process:

- Ionization and excitation of the atoms, produced by the inelastic scattering with the orbital electrons, absorbs a small amount of energy from the particle, but due to the high density medium of matter, this is the process that contributes most to energy loss. The Bethe-Bloch formula describes it very well in the typical kinematic ranges of nuclear and particle physics:

$$-\frac{dE}{dx} = 2\pi N_a r_e^2 m_e c^2 \rho \cdot \frac{Z}{A} \cdot \frac{z^2}{\beta^2} \cdot \left[\ln\left(\frac{2m_e\gamma_{REL}^2 v^2 W_{MAX}}{I^2}\right) - 2\beta^2 - \delta - 2\frac{C}{Z}\right] \tag{2.2}$$

where where c is the speed of light, Z is the atomic number of the medium, A is the number of nucleons of the medium, r_e and m_e the electron classical radius and rest mass respectively, W_{MAX} is the maximum energy transfer per collision, I is the mean excitation potential and δ and C are the density and shell corrections. Since electrons and positrons interact with same-mass objects, the formula is slightly modified for them.

- Elastic scattering with the nuclei leads to a trajectory change with minimal energy loss due to the usually high mass of the medium nuclei. The probability of a collision with the nucleus are proportional to $1/\sin^4\frac{\theta}{2}$ leading mainly to small angle deflections and rare, high angle scatterings.

- Emission of Cherenkov radiation, produced by the polarization of the electric field when a particle travels faster than the speed of light in the medium it is crossing: $v = c/n$, where n is the refraction index of the medium results in small energy loss.

- Nuclear and weak inelastic reactions, albeit very rare in most materials, can lead to nuclear fission and particle emission.

- Bremsstrahlung consists in the emission of γ radiation due to deceleration in electromagnetic fields. The process is practically relevant only for electrons and positrons, since the emission probability goes as $\sigma \propto (e^2/mc^2)^2$. Crossing matter, this introduces an extra component to their energy loss in matter, small at low energies but becomes dominant at higher ones, as shown in figure 2.4.

- When a particle traverses a region of varying dielectric constant, radiation is emitted during the transition. This has an intensity proportional to γ of the particle and has a sharp emission peak at $\theta \sim 1/\gamma$, thus mainly relevant for light objects.

In HEP we define a characteristic of the material called radiation length: the distance an electron has to cross inside it to emit enough radiation that its energy is reduced by a factor $1/e$, where e is Euler's number.

Photons are the gauge bosons of the electromagnetic interaction, but are neutral with respect to the interaction itself. Having no mass, their behaviour is strongly dependent from quantum effects. They interact with matter in three ways:

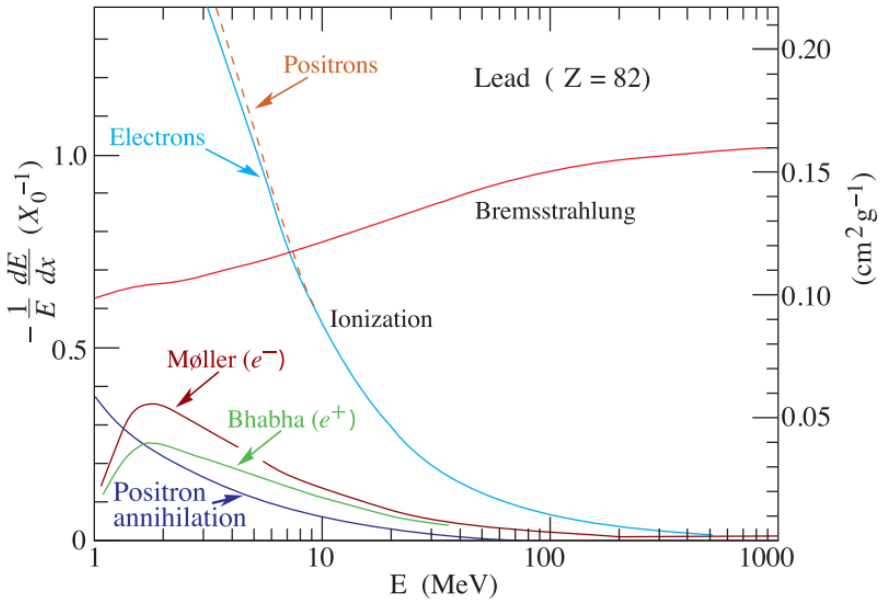

Figure 2.4: Electron energy loss processes compared. While ionization loss is the only relevant process at low energies, bremsstrahlung dominates higher ones.

- Photoelectric effect, where a photon is absorbed by an atom exciting or ionizing one of its electrons. In this latter case, the e^- is emitted with an energy of $E = h\nu - B.E.$, where B.E. is the binding energy of the state it previously occupied.

- Compton scattering, where the γ interacts with a free electron (a good approximation even for bound electrons in HEP) and changes its frequency.

- Pair production: the photon transforms into a e^+e^- pair, where each has half the energy of the photon. The cross section of this process is proportional to that of electron bremsstrahlung, resulting in an alternation of pair production and γ emission of its products.

The cross section of these processes is small, if compared to charged particles inelastic scattering, thus yielding a greater penetration of γ inside matter.
Neutrons and neutral hadrons interact only through the strong force, that is significant solely in a short range ($\sim 1\,fm$) around the nucleus and thus yields low cross sections. This is a secondary process also for charged hadrons. The interaction can result in a few

outcomes:

- Elastic scattering on the nucleus is the most common process involving neutral particles and it determines a change of trajectory and a loss of energy that depends from the recoiling material. When the nucleus has similar mass to the neutron, this recoils back taking a significant part of the incoming energy with it. This is called moderation.

- Inelastic reaction with the nucleus or its component includes processes that range from neutron capture to hadronic shower emission. This latter case is relevant only for high energy hadrons.

Neutrinos in the SM interact only with the weak force and conserve the lepton number . They are not directly observed in collider experiments, but they can be pinpointed by a lack of energy in apparently unbalanced processes.

2.2.3 Detectors and Identification

Identifying particles and more complex objects is essential to understand the underlying physics that produced them. Particle detectors that make up an experiment usually measure a single kinematic or position property of a particle. Trajectory, speed and energy are usually measured by gathering some electric or light signal emitted by the particle when crossing the active detector matter. In gas or liquid detectors, charged particles and photons produce free ions and electrons, that drift due to an electric field to some anodes and cathodes, producing an electric signal. In semiconductors, passing particles produce holes and excited electrons that drift towards opposite sides of the depletion region, generating a current. In transparent scintillation materials, the recombination of ionized particles and the excitation of electron states produce light that can be detected by dedicated instruments, for example photomultipliers. These are also used to detect Cherenkov light. Neutral particles are mainly revealed by detecting recoiling ionized atoms or charged products of inelastic reactions. The final step is undertaken by front-end electronics, part of a larger trigger and data-acquisition system that must read, combine, select and store potentially interesting information for complete off-line analysis.

Combining several position measurements the trajectory of a particle is reconstructed. Coupled with a magnetic field this yields good results in momentum measurement and provides the first information on the event topology. Time-of-flight and Cherenkov detectors can measure the speed of low (non relativistic) and high speed particles respectively. The energy is usually measured by complete absorption of the particle from detectors called calorimeters.
This information can be combined to obtain the mass of the detected particles, which in most cases is its most important identifying trait: $E^2 = p^2c^2 + m^2c^4$. The second important quantity we want to obtain is the charge of the particle. This is usually provided by the trajectory measurement, since the particle charge determines the bending of the particle trajectories inside a magnetic field. This is easily accomplished for low energy objects, but can be difficult for high-momentum ones, since they will have a nearly straight trajectory.

2.3 The Large Hadron Collider

The LHC (Large Hadron Collider) [15] CERN project is a $27km$ collider ring, installed $100\,m$ under the surface of Switzerland and France, inside the tunnel previously hosting the LEP collider (figure 2.5). In 2012 the machine has accelerated protons to a center of mass energy $\sqrt{s} = 8\,TeV$ and lead ions for a center-of-mass energy of $\sqrt{s} = 2.76\,TeV$ per nucleon. The peak luminosity for p-p collisions has varied widely from the first runs in 2010, reaching a value of $L_{peak} = 7.73 \times 10^{33}\,cm^{-2}s^{-1}$ in the last runs of 2012, high enough to bring to their limit the current detectors, but still lower than the target luminosity for the LHC. During the recent shut-down period, the accelerator has been improved to reach the center-of-mass energy of 13 TeV and a peak luminosity of $3 \times 10^{34}\,cm^{-2}s^{-1}$ is expected in 2016.

Two opposite proton beams are circulating in the LHC ring, segmented in a structure of 3564 bunch positions out of which up to 2808 can be filled at the same time. In the working conditions bunches collide at the ATLAS impact point every 25 ns. To curve the trajectories of the beams and keep them inside the accelerator, 1232 superconducting dipole magnets are positioned along the track. They are based on the Nb-Ti supercon-

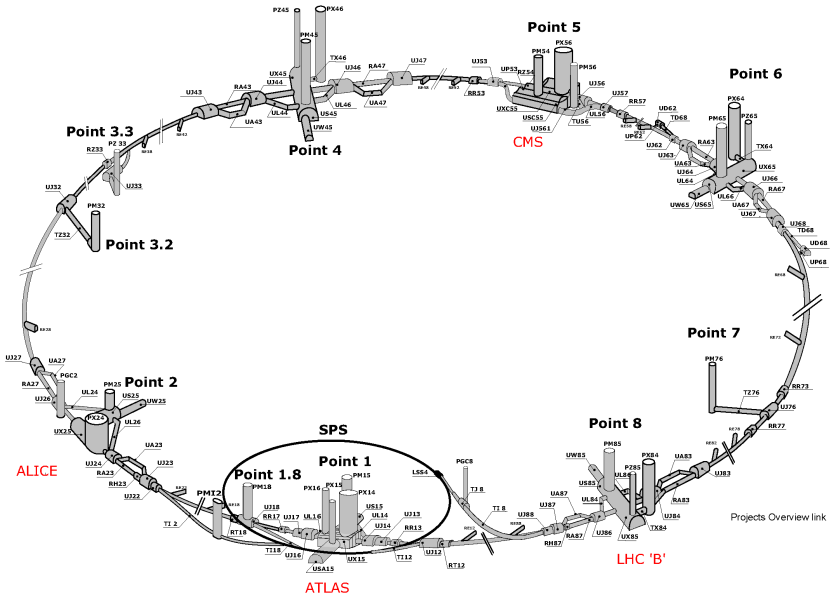

Figure 2.5: The Large Hadron Collider and the four main experiments.

ductor, working at a current of $11.85\,kA$ and a temperature of $1.9\,K$, maintained by a liquid-helium refrigerating system, generating a magnetic field of up to $8.4\,T$. The focusing system consists of 392 superconducting quadrupole magnets producing a $6.8\,T$ field. The beams circulate in two separate vacuum cavities kept at a pressure lower than $10^{-10}\,torr$.

The proton or lead acceleration chain starts in the Linac 2 linear accelerator and passes through three synchrotrons, the Proton Synchrotron Booster (PSB), the Proton Synchrotron (PS) and the Super Proton Synchrotron (SPS), pre-accelerating the beams to the energy of $450\,GeV$. Inside the LHC beam pipe, the protons are accelerated by 16 radiofrequency cavities with an electric field that reaches up to $5.5\,MV/m$.

Four main experiments are hosted at the interaction points:

- ATLAS (A Toroidal Lhc ApparatuS) is a multi-purpose detector, characterized by toroidal magnets which add to the central one, aimed at the discovery of new phenomena in particle physics.

- CMS (Compact Muon Solenoid) is another multi-purpose detector which looks for

the same traces of new physics ATLAS looks for, but does so using different and complementary technologies.

- ALICE (A Large Ion Collider Experiment) is an experiment built mainly to study the characteristics of quark-gluon plasma produced during heavy ion collisions, working at lower luminosities, but higher track multiplicities.

- LHCb is the most specific experiment, built to investigate the CP violation in Standard Model processes through the study of the physics of the B mesons.

2.4 ATLAS

The ATLAS [19] experiment is, as stated in the previous section, a multi-purpose detector installed at the interaction point 1 of the LHC, $100\,m$ underground. It is cylindrically symmetric, with a radius of $11\,m$ and a length of $42\,m$, covering the full 2π angle around the beam axis, in the polar ϕ coordinate, and an almost complete π coverage in the angle transverse to the beam axis.
Both at the 2012 energy of $8\,TeV$ and at the recently achieved energy of $13\,TeV$, the cross sections of the most interesting new-physics phenomena is very small, if compared to the total cross section of the p-p interactions. A very high luminosity is needed to see these rare events and high precision detectors are necessary to measure their properties. For ATLAS it means the following requirements:

- large acceptance in pseudorapidity ($\eta = -\ln(\tan\theta)$) and an almost full azimuthal angle (ϕ) coverage; this allows for the detection of total and missing transverse energy, for neutrino and neutral new physics identification;

- efficient tracking system for high transverse momentum (p_T) measurement at high luminosity and full event reconstruction at lower luminosities; the track reconstruction precision must be of the order of tenths of μm, to ensure the distinction between different interactions and early decay vertices.

- excellent electromagnetic calorimetry for electron and photon identification and hadron calorimetry for jet and missing transverse energy (E_T^{miss}) measurements;

- high precision muon detectors, able to guarantee accurate momentum measurements at design luminosities without the assistance of the innermost detectors;
- an extremely efficient and fast trigger, selecting only the most interesting events to be written on disk.

The ATLAS detector is composed by a large number of sub-detectors, as shown in figure 2.6, and electronic components, that can be regrouped as:

- the magnetic system, composed of a central super-conducting magnet and three toroidal magnets, to bend the particle trajectories;
- the inner detector, providing tracking near close to the interaction point;
- the calorimeter system, divided in electromagnetic and hadron calorimeter;
- a muon system to track muons in the outer layer of the detector;
- luminosity monitors, to provide on-line and integrated luminosity;
- a triggering system that limits the amount of data saved and stored to the most interesting events;
- the data acquisition and distributed analysis system to cope with the huge amount of data produced by the detector.

2.5 The Magnetic System

The momentum of the particles produced at the interaction point and detected by the ATLAS experiment is determined by bending their trajectories with a magnetinc field and inverting Lorentz's law $\vec{F} = q\vec{B} \times \vec{v}$. The magnetic system of the ATLAS experiment [20] is composed of:

- the Central Solenoid (CS);
- the Barrel Toroid (BT);

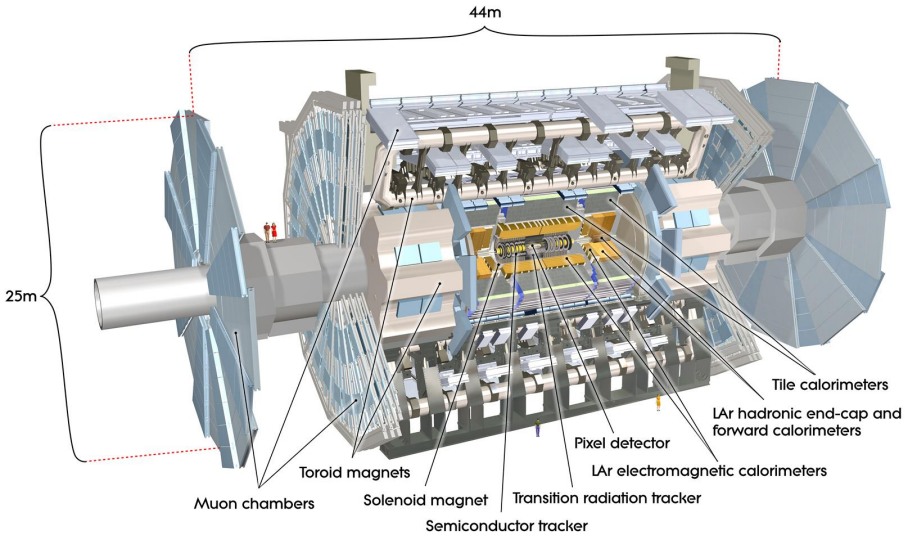

Figure 2.6: The ATLAS experiment.

- the two End-Cap Toroids (ECT);

The Central Solenoid, displayed in figure 2.7, is a super-conducting solenoid providing a nominal magnetic field of $2\,T$, installed around the inner detector with a radius of $1.2\,m$ and a length of $5.3\,m$. The energy absorption of the solenoid is minimized through the use of a very thin coil and the sharing of the same vacuum vessel with the LAr calorimeter, in order not to alter significantly the performance of the calorimeters themselves.

The Barrel Toroid (BT, figure 2.8) and the two End-Cap Toroids (ECT) form a super-conducting toroid system that provides a $\sim 4\,T$ magnetic field mostly orthogonal to the muon trajectories, to guarantee a better measurement of the muon characteristics. Each one of them is composed of eight coils, super-conducting and air-core, with an open structure to minimize the multiple scattering effects. The BT is $25\,m$ long, with an inner core of $9.4\,m$ and an outer diameter of $20.1\,m$, while the ECT is $5\,m$ long, with an inner core of $1.64\,m$ and an outer diameter of $10.7\,m$. The BTs generate the magnetic field in the region $|\eta| \leq 1$, the ECTs in the region $1.4 < |\eta| < 2.7$, while the so-called transition region, $1 < |\eta| < 1.4$, is characterized by a superimposition of the two fields.

Figure 2.7: The Central Solenoid of the ATLAS experiment.

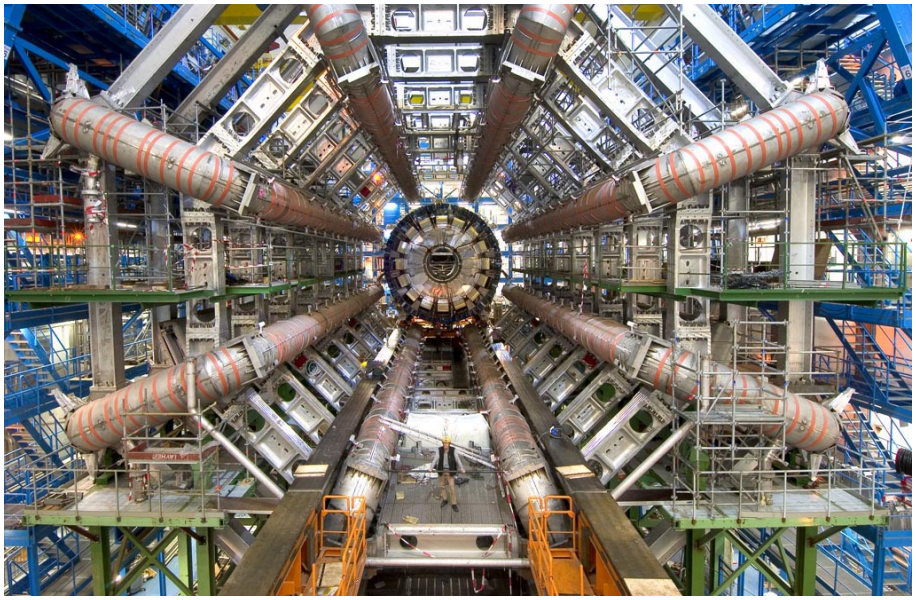

Figure 2.8: The Barrel Toroid magnet of the ATLAS experiment.

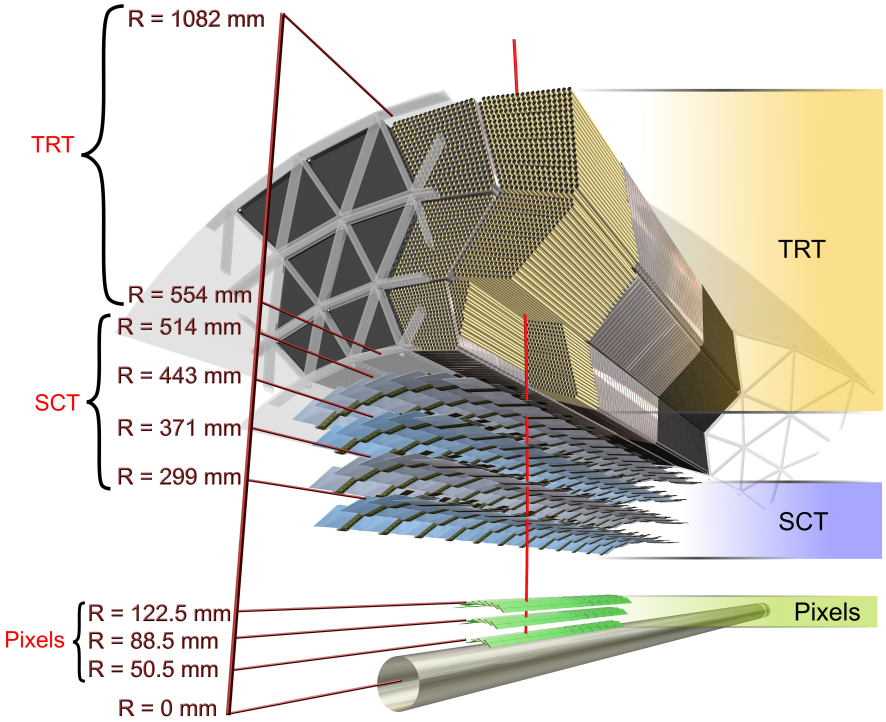

Figure 2.9: The inner detector of the ATLAS experiment.

2.6 The Inner Detector

The inner detector (ID) [21] provides the tracking of particles in the inner region, next to the interaction points. It contributes to particle identification and gives essential information to identify rapidly decaying particles. Given the high track densities of the LHC, the momentum and vertex resolution requirements from physics call for high precision measurements, to be realized through fine-granularity detectors. Figure 2.9 shows a section of the inner detector, constituted mainly of successive layers of sub-detectors placed in a cylindical configuration around the beam pipe.

The highest granularity is achieved in the innermost region using three semiconductor pixel detectors, while the following layers are made of semiconductor strip layers and

a transition radiation tracker (TRT) that provides near-continuous track-following with less material, limiting the cost and the energy loss. The high precision of the silicon detectors, together with the high number of points coming from the TRT allows for high resolution tracking and measurements in the ϕ and z coordinates. This is essential for the identification of a secondary vertex produced by the decay of a B quark or a τ lepton, signature of some of the most interesting events observable at ATLAS. The outer radius of the ID cavity is $115cm$ and the full length is $7m$. Its structure is divided in three units: a barrel part extending in the $\pm 80\,cm$ region in z, closed at the extremities by two identical end-caps. The precision tracking elements are contained within a radius of $56cm$, followed by the TRT and the supporting and read-out services. The overall layout provides tracking in the $|\eta| < 2.5$ region, including impact parameter measurements and vertexing for heavy flavour and τ tagging.

2.6.1 Pixel Detector

The pixel detector is designed to provide a very high-granularity, high-precision set of measurements as close as possible to the interaction point. It is based on silicon p-on-n pixels where the current produced by the drift of electrons and holes excited by a passing particle is read by separate electronics for each element. The two-dimensional segmentation of the sensors gives space points without the ambiguities of the strip detectors, but requires a high number of connections. The readout is accomplished by chips of large area, with individual circuits for every pixel of the detector, including buffers to store the data waiting for the Level 1 trigger decision; these chips have to be radiation hard, to withstand over $300kGy$ of ionizing radiation and 5×10^{14} neutrons per cm^2 over ten years of operations. The system contains a total of 140 million pixels, each $50\,\mu m$ in the ϕ direction and $300\,\mu m$ in the z coordinate, distributed on three barrels at the average radii of $4\,cm$, $10\,cm$ and $13\,cm$ and five disks on each side, between radii of $11\,cm$ and $20\,cm$, which complete the angular coverage. The thickness of each layer is estimated to be about 1.7% of a radiation length at normal incidence. During the long shut-down between Run I (the 2010, 2011 and 2012 data tanking) and Run II (2015 and 2016 data-taking), an additional layer, called "b-layer" was inserted between the old Pixel Detector and the beam pipe.

2.6.2 Semiconductor Tracker

The SCT is designed to provide eight precision measurements per track in the intermediate radial region, contributing to the measurement of momentum, impact parameter and vertex position, as well as providing good pattern recognition thanks to its high granularity. The barrel SCT uses eight layers of silicon microstrip detectors to provide precise position measurements in the ϕ and z coordinates. Each silicon detector is $6.36 \times 6.60\, cm^2$ with 768 readout strips of $80\, \mu m$ pitch. Each module consists of four single-sided p-on-n silicon detectors. On each side of the module, two detectors are wire-bonded together to form $12.8\, cm$ long strips. Two of these structures are then glued together back to back with an angle of $40\, mrad$ between each other. The readout is realized by a front-end amplifier and discriminator, followed by a binary pipeline to store the hits above threshold, waiting for the trigger decision. The end-cap modules are similarly assembled, but they use tapered strips, with one set aligned radially. The detector contains $61\, m^2$ of silicon detectors, read by 6.2 million channels, providing a spatial resolution of $16\, \mu m$ in ϕ and $580\, \mu m$ in z, values that allow a correct identification for tracks separated by more than $\sim 200\, \mu m$. The four barrel layers are mounted on barrels at the radii of 30.0, 37.3, 44.7 and $52.0\, cm$, while the end-cap modules are mounted in three rings onto nine wheels, providing the pseudorapidity coverage $|\eta| \leq 2.5$.

2.6.3 Transition Radiation Tracker

The TRT is based on the use of straw detectors, that can operate at the very high rates required by the LHC. Electron identification is provided by using xenon gas ionization to detect transition-radiation photons created in a radiator between the straws. This technique is intrinsically radiation hard and allows a large number of measurements, typically 36, to be made on every track at a relatively low cost. Every straw is $4\, mm$ in diameter and equipped with a $30\, \mu m$ diameter gold-plated wire, giving a fast response while maintaining good mechanical and electrical properties. The barrel contains about 50000 straws, each divided in two at the center, with read-out at each end; the end-caps contain 320000 radial straws, with the read-out at the outer radius. The total number of electronic channels is 420000, providing drift-time measurements, with a spatial res-

olution of $170\,\mu m$ per straw, and two independent thresholds, to discriminate between tracking hits and transition-radiation hits. The TRT is operated with a gas mixture of $70\%Xe$, $20\%CO_2$ and $10\%CF_4$. A good pattern recognition is assured by the continuous tracking: within the radial space available, the straw spacing has been optimized for tracking at the expense of electron identification, which would be improved by a greater path length in the radiator material and fewer straw detectors. A total measurement accuracy of better than $50\,\mu m$ at the LHC design luminosity is achieved, thanks to the large number of straw hits per track.

2.7 The Calorimeters

Calorimetry consists in measuring particle energy through complete absorption. A signal output (voltage or current) proportional to the released energy is read by front-end electronics and processed to recontruct the initial energy value. In ATLAS this is accomplished through an electromagnetic calorimeter and a hadronic calorimeter, as shown in figure 2.10.

Before reaching the calorimeters, the particles are expected to cross an average $1.5\,X_0$ radiation lengths, losing energy in the material preceding the calorimeter. To correct for this energy loss, a pre-sampling detector is used, made of a thin $(0.5 \div 1\,mm)$ layer of liquid argon that gets ionized by incoming particles. It is coupled in the end-caps with a scintillation plate. It detects showers of low-energy particles produced in the preceding material that would otherwise be absorbed by the passive absorber layers.

2.7.1 The Electromagnetic Calorimeter

The ECAL [22] is a Pb - LAr calorimeter that uses Liquid Argon as active medium and Lead as absorber. It covers a region in pseudorapidity $|\eta| < 3.2$, divided in Barrel ($|\eta| < 1.475$) and End Caps ($1.375 < |\eta| < 3.2$); the thickness of the absorber is modulated as a function of pseudorapidity to improve the linearity of the calorimeter, that is better then 0.5%. In the region $|\eta| < 2.5$ the ECAL is segmented longitudinally in three sections, of respectively $\sim 6\,X_0$, $\sim 18\,X_0$ and $\sim 2 \div 12\,X_0$ radiation lengths. The first section acts as a pre-shower detector to improve particle identification and measure-

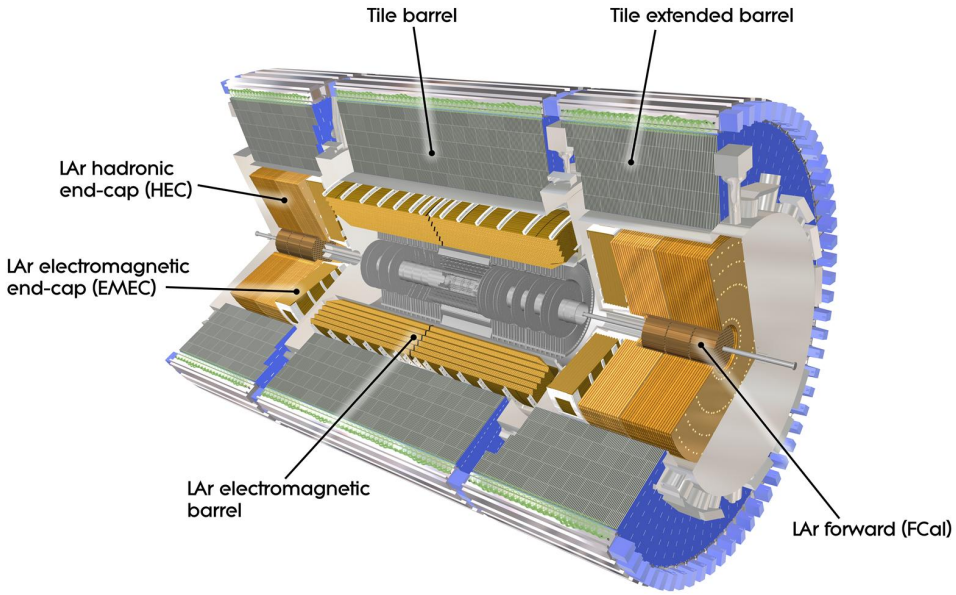

Figure 2.10: The Calorimeters of the ATLAS experiment.

ments in the η coordinate. This is accomplished through a row of strips disposed in the η direction. The second section is segmented into towers of $\Delta\eta \times \Delta\phi = 0.025 \times 0.025$, while the last one has a granularity of $\Delta\eta \times \Delta\phi = 0.05 \times 0.025$. The total number of electronic channels that read the calorimeter is around 200000. The energy resolution of this calorimeter has been measured in electron test beams, obtaining $\frac{\Delta E}{E} = \frac{9.4\%}{\sqrt{E}} + 0.1\%$ (energy in GeV) [23] with negligible uncertainty.

2.7.2 The Hadronic Calorimeter

The HCAL is divided in three different sections that use different detection techniques, depending on the environmental radiation levels. The Tile calorimeter is made of iron plates alternated with scintillator layers as active material, covering the barrel in the pseudorapidity region $|\eta| < 1.7$. The second region ($1.5 < |\eta| < 3.2$) is covered by a liquid argon calorimeter (HEC) that uses $(25 \div 50\, mm)$-thick copper plates as absorber. Two frontal forward calorimeters (FCAL) gather data in the region ($3.1 < |\eta| < 4.9$);

they are divided in three sections, using tubes and rods filled with liquid argon as active medium alternated with the metal plates: copper in the first section and tungsten in the others.
The energy resolutions of the different sections have been measured i test-beams using pions and electrons (energies in GeVs), fitting the equation $\frac{\Delta E}{E} = \frac{a}{\sqrt{E}}\% + b\%$, with the following results:

- for the barrel tile calorimeter, using pions $a = 52.7 \pm 0.9\sqrt{GeV}$ and $b = 5.7 \pm 0.2$, with $e/h = 1.33 \pm 0.6 \pm 0.4$ [24];
- for the end-caps calorimeter with pions, tests using a signal weighting approach yielded $a = 84.6 \pm 0.3\sqrt{GeV}$ for π^- and $a = 81.7 \pm 0.4\sqrt{GeV}$ for π^+ with negligible b [25];
- for the forward hadronic calorimeter we have $a = 94.2 \pm 1.6\sqrt{GeV}$, $b = 7.5 \pm 0.4$ in pion test-beams [26].

2.8 The Muon System

The structure of the Muon Spectrometer is shown in figure 2.11. It is based on the magnetic deflection of the muon tracks in the large superconducting toroid magnets, instrumented with separate trigger and high precision tracking chambers.

In the barrel region, tracks are measured in chambers arranged in three cylindrical layers, called stations, around the beam axis; in the transition and end-caps regions, the Chambers are installed vertically, again in three stations. The precision tracking is provided by the Monitored Drift Tubes (MDTs) and Cathode Strip Chambers (CSCs) detectors, while the trigger system, that covers the pseudorapidity range $|\eta| \leq 2.4$, uses Resistive Plate Chambers (RPCs) in the barrel and Thin Gap Chambers (TGCs) in the end-cap regions. The trigger system of the muon spectrometer is designed to serve three different scopes in ATLAS:

- bunch crossing identification, separating events with a time resolution better than $25\,ns$;

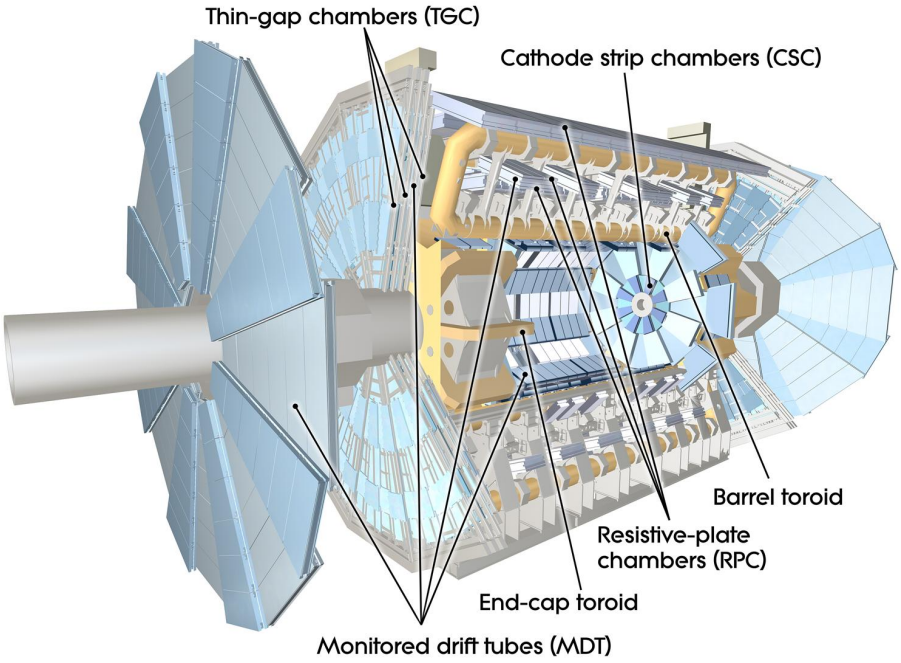

Figure 2.11: The Muon System of the ATLAS experiment.

- triggering with well-defined p_T cut-offs in moderate magnetic fields;
- measurements of the second coordinate in the direction orthogonal to that measured by the precision chambers, with a resolution of $5 \div 10\,mm$

In the barrel region MDTs and RPCs are arranged in three concentric layers at 5, 7.5 and $10\,m$ from the beam axis. In the end-caps and transition regions the MDTs and TGCs are arranged in four wheels at 7, 10, 14 and $21 \div 23\,m$ from the interaction point. The CSC chambers are mounted between the calorimeter and the magnet at high pseudorapidities. This global arrangement is such that particles from the interaction point cross three stations before leaving the detector. The structure is kept under control by a sophisticated optical alignment system. The RPC is a gaseous parallel electrode-plate detector, with no wires. Each of the two rectangular detector layers that form the RPC chamber is read out by two orthogonal series of pick-up strips: the η strips are parallel to the MDT wires and provide the bending view of the trigger detector, while the ϕ strips are orthogonal to the MDT wires, providing the second coordinate

measurement. The RPCs combine a spatial resolution of $1\,cm$ with a time resolution of $1\,ns$. The basic RPC unit is a narrow gas gap that divides two parallel resistive Bakelite plates, separated by insulating spacers. The primary ionization electrons are multiplied into avalanche by a high electric field of about $4.5\,kV/mm$ in a gas mixture based on tetrafluoroethane ($C_2H_2F_4$) with some small admixture of SF_6.
The TCG are very thin Multiwire Proportional Chambers, with the difference that the anode wire pitch is larger than the cathode-anode distance. Signals form the anode wires, arranged parallel to the MDT wires, provide the trigger information together with read-out strips arranged orthogonal to the wires, used for the measurement of the second coordinate, too. This setting allows a very short drift time and a fast response of the detector ($20\,ns$), enough to identify muons at the expected rate of $40\,MHz$. Operated with a highly quenching gas mixture of $55\%CO_2$ and $45\%n - C_5H_{12}$ at a tension of $3.1\,kV$, this detector permits operation in saturated mode, with a number of advantages:

- small sensitivity to mechanical deformations;
- small dependence of the pulse height on the incident angle;
- nearly Gaussian pulse height distribution and no streamer formation.

Over most of the η range, the precision measurement of the track coordinates in the principal bending direction of the magnetic field is provided by the MDT detector, which is based on drift chambers consisting in two multi-layer drift tubes (3-4 layers) where each drift cell is enclosed in an aluminium tube to improve the mechanical stability of the chambers. The tubes are operated with a mixture of $93\%Ar$ and $7\%CO_2$ at $3\,bar$ pressure, for a total volume of $800\,m^3$. This working point provides a non-linear space-time relation, with a maximum drift time of $700\,ns$, a small Lorentz angle and excellent ageing properties. The single-wire resolution is around $\sim 80\,\mu m$ when operated at high gas pressure, thanks to the mechanical isolation of each sense wire from its neighbours.
The CSCs are multi-wire proportional chambers with cathode strip readout and with a symmetric cell in which the anode-cathode spacing is equal to the anode wire pitch.They operate at high pseudorapidities ($2 < |\eta| < 2.7$), complementing the MDTs, with a larger granularity. The precision coordinate is obtained by measuring the charge induced on the segmented cathode by the avalanche formed on the anode wire. Good spatial resolution

-	Year	Energy	$L_{peak}(10^{33}cm^{-2}s^{-1})$	peak $<\mu>_{LB}$	$L_{int}(fb^{-1})$
Run I	2010	$7\,TeV$	0.2	∼5	0.047
-	2011	$7\,TeV$	3.6	∼20	5.5
-	2012	$8\,TeV$	7.7	∼40	22.7
Run II	2015	$13\,TeV$	5	∼35	4.2
-	2016-2018	$13\,TeV$	exp. ∼20	exp ∼60	exp. ∼ 100

Table 2.1: The luminosity acquired by the ATLAS experiment and the expected Run II luminosity.

is obtained through segmentation of the cathode and by charge interpolation between neighbouring strips. The CSC gas admixture contains $30\%Ar, 50\%CO_2$ and $20\%CF_4$, containing no hydrogen to reduce significantly the neutron background. With this set-up it's possible to achieve a spatial resolution better than $60\,\mu m$, small electron drift times ($30\,ns$), good time resolution ($7\,ns$) and a good two-track separation.

2.9 Luminosity Measurement

Luminosity Measurement is an essential aspect of the ATLAS experiment because of the impact it has on the measurement of the production rate of any physical phenomena analysed during the lifetime of the experiment [27]. The peak instantaneous luminosity, the maximum average interactions per Bunch Crossing $<\mu>_{LB}$ and the integrated luminosity acquired by the ATLAS experiment, including the future expected schedule, are summarized in table 2.1.

For a precise measurement of the cross-section of these processes, we require a high-precision time-integrated luminosity, due to the relation between number of signal events, luminosity and cross-section $N = L \times \sigma$. This is obtained off-line through a wide number of different methods that include:

- using the optical theorem and elastic collisions;
- extrapolating it from beam parameters in dedicated runs;

- inverting the above equation using the information of the detectors;

However, for precision measurements and on-line control of the detector, the bunch-by-bunch luminosity is also needed (figure 2.12). The proper knowledge of the pile-up (interactions per bunch crossing) for individual bunches and on short term intervals of time (1-2 minutes) helps to introduce small corrections and to tune pre-scaling coefficients for those detectors than show non-linearity responses at high luminosities (see appendix A). The detectors that can provide online luminosity measurements (at different accuracy

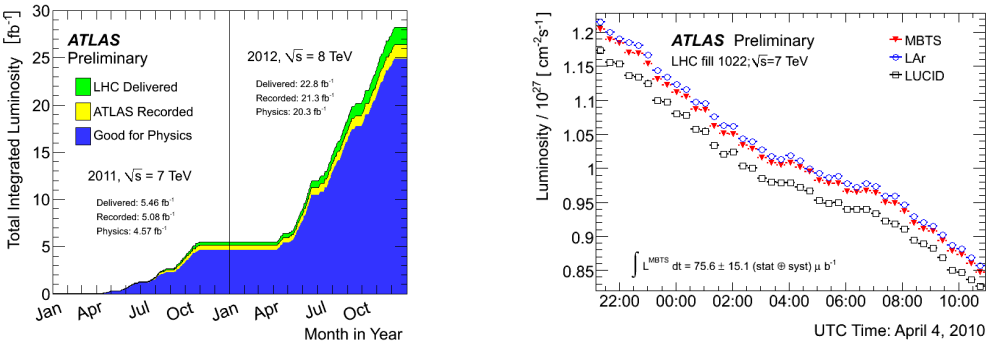

Figure 2.12: Integrated luminosity registered during stable-beam runs in 2011/2012 and comparison of three different luminosity measurements obtained during the 2010 tests.

levels and pseudorapidities) with bunch-crossing separation are:

- BCM (Beam Condition Monitor, $|\eta| \sim 4.2$) provides radiation monitoring to protect the inner detector, but also provides precise information on the condition of the beams and is thus used to calculate luminosity, but cannot work properly at the $25\,ns$ bunch-spacing;

- LUCID (Luminosity Cherenkov Integrating Detector, $5.6 < |\eta| < 5.9$), a forward Cherenkov threshold detector, designed to sustain a high event rate and high radiation doses, it can work at design luminosity, separating the contribution for each bunch (see Appendix B);

- MBTS (Minimum Bias Trigger Scintillator, $5.6 < |\eta| < 5.9$), another forward detector, based on scintillator plates, used in the first, low-luminosity measurements;

- track counting using the ID information can provide similar measurements using an algorithm that assumes luminosity to be proportional to the number of tracks, but in the 2012 beam conditions this method showed low accuracy and is used only as integrated of BC's.

The calorimeters are used to measure on-line luminosity integrated over the LB's and are essential to provide a stable reference to study the behaviour of the dedicated luminometers:

- The End-Cap Electromagnetic Calorimeter (EMEC, $1.5 < |\eta| < 3.2$), the end-cap portion of the Electromagnetic Liquid Argon (LAr) calorimeter;
- The Forward Calorimeter (FCal, $3.2 < |\eta| < 4.9$), the high-η portion of the Electromagnetic Liquid Argon calorimeter;
- The Tile calorimeter (TileCal, $|\eta| < 1.7$), the barrel portion of the Hadronic Calorimeter (HCal).

These are calibrated through several methods, that exploit beam characteristics and known physics processes. The first calibration and most used calibration technique is performed using beam conditions in a Van Der Meer scan [27]: to measure the overlap area, the two colliding beams are moved, in subsequent steps, from a non-overlapping state to a full overlapping state and again to another non-overlapping state, both on the X and on the Y axis. When the superimposition is complete, the full beam luminosity is achieved (known from beam parameters). The scans are repeated several times to test the calibration stability. This kind of calibration has an uncertainty that depends on beam parameter uncertainty (beam current in particular) and on the extrapolation to the higher luminosity regimes; this has improved over the Run I data-taking, reaching a value of 1.9% [28]. Calibration through physics channels, in particular the W and Z bosons, yields an uncertainty that depends on the limited knowledge of the parton distribution functions (PDF), a value that has improved over the run and is now ~ 3, depending on the process used (see appendix B). Finally, calibration through a dedicated detector (ALFA[1]) [29] that measures the flux of protons scattered elastically should fur-

[1]The ALFA detector measures the total elastic cross-section in dedicated runs, but can, under certain conditions, be used for luminosity calibration

ther lower the uncertainty.

2.10 ATLAS Trigger System

The triggering system of a detector that works at high luminosity and high energy is essential to reduce the huge amount of data it takes every second to a flux that can be saved on disk for the forthcoming analysis.
The ATLAS Trigger and Data AcQuisition system (TDAQ) is based on three levels of on-line selection. Each trigger level refines the decisions taken at the previous level and applies additional selection criteria, progressively increasing the selection accuracy and decreasing the rate of accepted events (figure 2.13). The initial bunch crossing rate of $\sim 40\,MHz$ at the design luminosity of $10^{34}\,cm^{-2}s^{-1}$ has to be reduced to the permanent storage rate of $\sim 100\,Hz$. The event selection is complicated by the fact that for each bunch crossing multiple proton-proton interactions can occur, usually not very interesting, the so-called *pile-up*. To evaluate the rate of minimum bias interactions we have to use the cross-section $\sigma \sim 10^{-25}\,cm^2$ and the design luminosity $L \sim 10^{34}\,cm^{-2}s^{-1}$, yielding an interaction rate of $\sim 1\,GHz$. So a 10^7 rejection of *minimum-bias* events has to be achieved, while maintaining a good efficiency for the most interesting physical phenomena. Taking into account that nearly half of the bunches are empty, ~ 40 pile-up interactions are expected in each bunch crossing event. The three levels of ATLAS trigger systems are called Level 1 (LVL1), Level 2 (LVL2) and Event Filter (EF). Together, the Event Filter and the LVL 2 trigger are called High Level Trigger (HLT), now unified into a single farm.
Level 1: the first level is based on hardware boards, requiring several conditions in coincidence or veto. The selection is based on reduced-granularity information from several sub-detectors: high transverse-momentum (p_T) muons are identified in the trigger chambers of the muon spectrometer, RPCs in the barrel and TCGs in the end-caps, while the calorimeter trigger searches for high-p_T electrons and photons in the ECAL and jets and τ-leptons decaying into hadrons in the hadronic calorimeter, in all these cases optional energy isolation criteria can be applied; furthermore, large missing energies

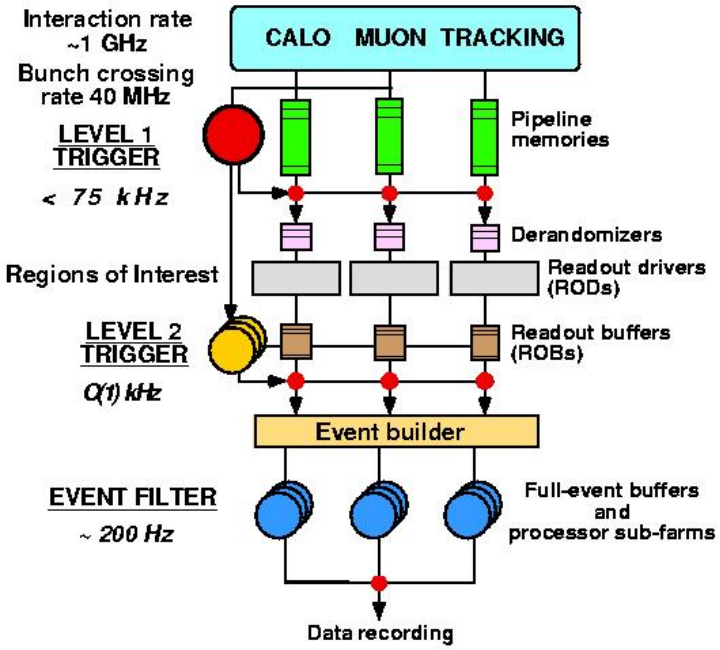

Figure 2.13: ATLAS trigger levels.

and high total transverse energies are among the selection criteria. Several different p_T thresholds can be set and their decisions are saved even if those values are not used for triggering. Primary (used for the decision) and secondary Regions of Interest (RoIs) are made available by the LVL 1 to improve the decision of the LVL 2, telling it where to find the most interesting events. The LVL1 provides trigger decisions at the rate of $40\,MHz$ with a latency of $\sim 1\,\mu s$. An essential requirement on the LVL 1 trigger is that it should uniquely identify the bunch crossings of interest. Due to the short bunch crossing interval ($25\,ns$) and the sheer distance between some detectors and the pulse length in the calorimeters (that can extend over several bunch crossings), this is a non-trivial request. It means that reducing the rate to the $75 \div 100\,kHz$ required by the front-end systems will be an extremely difficult task as the luminosity approaches the design value.

Level 2: the second trigger level consists of a farm of PCs that can receive data coming from the regions of interest found in LVL 1 at the rate of $100\,kHz$ and has to lower the output rate to a value of $\sim 1\,kHz$. The RoIs point Read Out Buffers (ROBs) containing

interesting data, and the LVL2 gathers them and applies selection algorithms very similar to the ones used off-line. With the Regions of Interest mechanism the data that has to be processed by LVL2 is decreased by a factor of 10. The latency of the LVL 2 varies with each event, but it is expected to be in the range $1 \div 10\,ms$. In the case of muon triggers, the LVL 2 sharpens and, if necessary, raises the p_T thresholds imposed at LVL 1 and applies isolation requirements; to do this it uses the information from the precision chambers, the inner detector and the calorimeters. For isolated electrons, LVL 2 uses full-granularity calorimeter information and matches this information with tracks from the ID. For photons, rejection is harder due to their lack of charge and consequent low probability of detection in the ID; in this case, two photons in coincidence can be required to select some of the most interesting phenomena. For the hadronic/τ trigger, LVL 2 rejection is achieved through a match of an ID track with an isolated calorimeter cluster analyzed at full granularity. Jets are harder to reject and the only possible requirements are increased thresholds and b-tagging through secondary vertex identification in the ID, still under study.

Event Filter (EF): the last High Level Trigger has to limit the data rate to $\sim 100\,Hz$, using algorithms similar to those of LVL 2 and off-line selection, but more refined and extended to the information coming from the whole ATLAS detector. The final output data is around $100\,MB/s$.

Events selected by LVL 1 are read out from the front-end electronics systems of the detector onto ReadOut Drivers (RODs) and then into ReadOut Buffers (ROBs); a large number of front-end electronics are multiplexed into each ROB. All the data for the bunch crossing accepted by LVL 1 are held in the ROBs until the event is rejected by LVL 2 or it is accepted and successfully transferred by the DAQ system to storage associated with the Event Filter (EF), the third level of event selection. This transfer is called event building, and it involves composing the many fragments of each event to store them in a single memory accessible by an EF processor.

Conclusions

How can men investigate the smallest components of matter and the interactions that bind them all together? In this chapter we started to answer this question. We started from the production of the fundamental particles in the accelerators, later focusing on the Large Hadron Collider. We followed with particle interaction with matter, examining how it can be used to detect and measure the products of interesting phenomena. Finally, we expanded on the ATLAS experiment, one of the most advanced instruments in the field, that has been used for this thesis.
In the following chapter we will see in detail what happens at LHC, which are the production and decay channels of the Higgs boson at $\sqrt{s} = 8$ and $13 TeV$. Object reconstruction and analysis techniques will complete the preliminary chapters.

Chapter 3

The Higgs boson and the associated production $t\bar{t}H$ in ATLAS

In Chapter 1 we reviewed the Standard Model of Particle Physics and introduced the EW Symmetry Breaking mechanism. The Higgs boson has then been introduced as a consequence of this theory effectively giving rise to a new kind of interaction, one based on particle mass. In Chapter 2 we have seen the techniques that are currently used to study the Higgs boson and the fundamental principles upon which they are based. In the first section of Chapter 3 we briefly list the first searches for the new boson and the constraints put on its mass by previous experiments. In section 3.2 the main production processes at LHC are explained, followed by its decay channels and their signatures in ATLAS. Section 3.4 illustrates the discovery, announced on the 12th of July 2012, of the Higgs boson. The experimental procedure and results are briefly outlined. Finally, Section 3.5 illustrates the main features and characteristics, including the theoretical production cross-section, of the associated production ($t\bar{t}H$) channel, together with its most important branching ratios.

3.1 Constraints on the Higgs boson mass

Since its first formulation, the EW Symmetry Breaking mechanism has been regarded as a means to provide the mass to fundamental particles. After the discovery of the W

and Z bosons in 1983 [30] [31] [32] and of the top quark [33] [34], the Higgs boson discovery became the next great objectives in High Energy Physics. Several experiments tried to first determine the mass of the Higgs boson from Standard Model constraints and then to search for it directly [35].

The first constraints are purely theoretical: the Higgs boson is necessary to introduce cancellation of the self-interaction divergences of the W boson in the vertex WW→WW, as explained in Chapter 1. The introduction of the Higgs allows the cancellation if this contribution and removes the divergences. This is valid only if the mass of the boson is comparable to the EW scale ($M_{Hmax} \sim 700\,GeV$) [36]. Moreover, at high M_H, the theory becomes non-renormalizable due to the divergence of the Higgs self-coupling term over a scale which would become the scale of new physics. On the contrary, a low-mass boson would produce an unstable or meta-stable EW vacuum, indicating that the minimum vacuum energy is a false minimum and that there is, instead, a lower level below some boundary. This also depends from the top mass, as displayed in figure 3.1 with the latest measurements.

From an experimental point of view, before the LHC era, Higgs boson direct and indirect searches have been performed at LEP [38] and Tevatron [39]. There, stringent constraints on the Higgs mass have been evaluated.

Indirect searches exploit the dependence of the SM measurements from the Higgs mass. A global χ^2 fit is then performed and constraints on M_H and properties are computed. An example is given by formula 3.1, where we can see the logarithmic dependence of M_W from the Higgs mass due to corrections to one (and partial two) loop order [40], as the ones shown in figure 3.2.

$$m_W = 80.409 - 0.507\left(\frac{\Delta\alpha_h}{0.02767} - 1\right) + 0.542\left[\left(\frac{m_t}{178}\right)^2 - 1\right] - 0.05719\ln(m_H/100) - 0.00898\ln^2(m_H/100), \quad (3.1)$$

where $\Delta\alpha_h = 0.02767(16)$ is the hadronic contribution to the shift in the fine structure constant; missing units are in GeV.

Direct searches are dependent on the decay channels: due to resonances and available decay energy, these have different branching ratios, as shown in figure 3.3, changing the experimental signature accordingly.

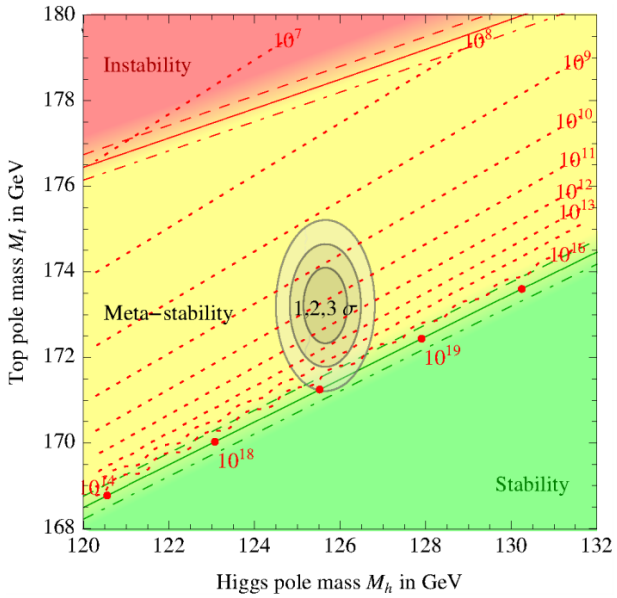

Figure 3.1: SM phase diagram in terms of Higgs and top pole masses. The plane is divided into regions of absolute stability, meta-stability, instability of the SM vacuum, and nonperturbativity of the Higgs quartic coupling. The dotted contour-lines show the instability scale Λ in GeV assuming $\alpha_S(M_Z) = 0.1184$. The image is a zoom in the region of the preferred experimental range of M_H and M_t (the grey areas denote the allowed region at 1, 2, and 3 σ). Plot taken from [37]

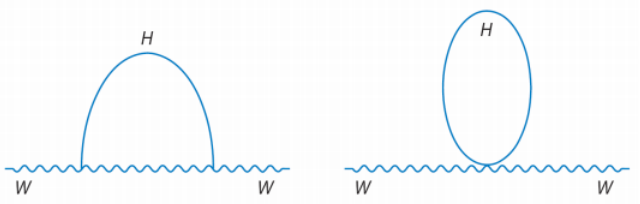

Figure 3.2: Higgs correction to the W boson mass propagator and, consequently, to its mass.

The measurements performed at LEP and Tevatron have different sensitivities to the

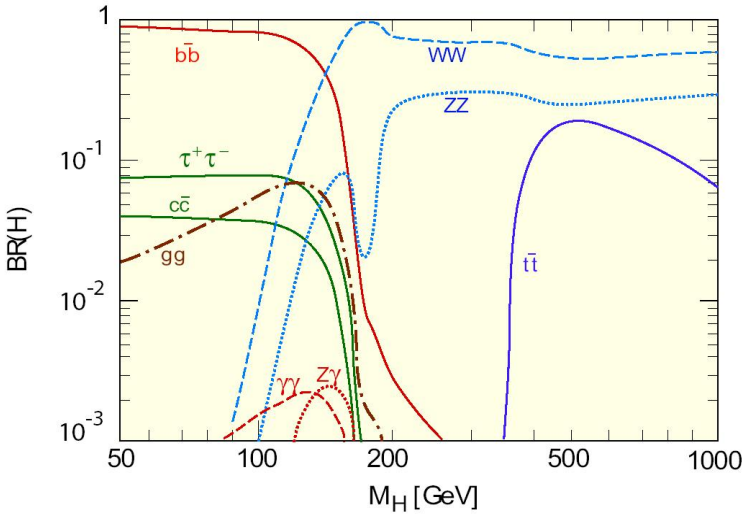

Figure 3.3: Higgs decay branching ratios as a function of its mass.

Higgs mass and properties.

The Large Electron Positron (LEP) was an e^+e^- collider built at CERN in the same tunnel that now hosts the LHC. Due to the low mass of the reacting particles, their coupling with the Higgs is very small. The main production channel in this kind of interaction is called Higgs-strahlung, where a high energy Z boson emits a H before decay. Since LEP energy reached a peak $\sqrt{s} = 209\,GeV$ (in 2000), it could only investigate H boson masses below $209 - Z_{mass} = 118\,GeV$, where the main decay channel is $H \to b\bar{b}$. The experimental signature was, thus, four jets or two leptons and two jets, with two jets from b-quark decay, where the Z boson could either go into a $q\bar{q}$ or l^+l^- pair (figure 3.4).

Tevatron, on the other hand, was a $p\bar{p}$ collider operating at the peak energy of $1.96\,TeV$ since 2001. Hadron colliders can investigate a wider variety of signals and can achieve higher reaction energies, at the cost of a much more pronounced background and a greater uncertainty on the initial interaction energy. Here the main production channel is the gluon-gluon fusion, but since the subsequent decay with the largest BR ($H \to b\bar{b}$) (section 3.3) is swamped by QCD bb production, the most sensitive channel at Tevatron is the associate WH production: $pp \to HW \to b\bar{b}l\nu$, as shown in figure 3.5. Thanks

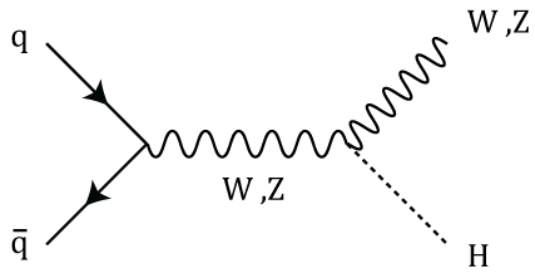

Figure 3.4: Higgs production through the Higgsstrahlung mechanism.

to the higher cross-section and luminosity, rarer H decay channels could be explored at Tevatron: $H \to \gamma\gamma$ and $H \to W^+W^-$. The experimental signatures thus multiply: an electroweak boson is identified, with its different leptonic decay modes, together with $b\bar{b}$, $\gamma\gamma$, $l\nu l\nu$, $l\nu q\bar{q}'$ and $q\bar{q}'q'\bar{q}$.

Figure 3.6 shows the final confidence level results obtained as a combination of the

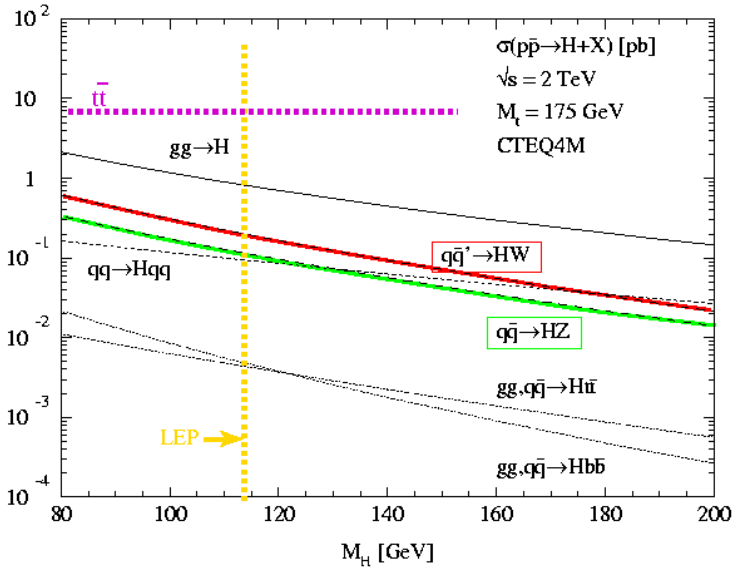

Figure 3.5: Higgs production at the Tevatron collider at $\sqrt{s} = 2\,TeV$.

experiments at LEP (left) and at Tevatron (right), with no significant excess from the Standard Model background [41, 42].

The global fit of the SM parameters and the direct research constraints are sum-

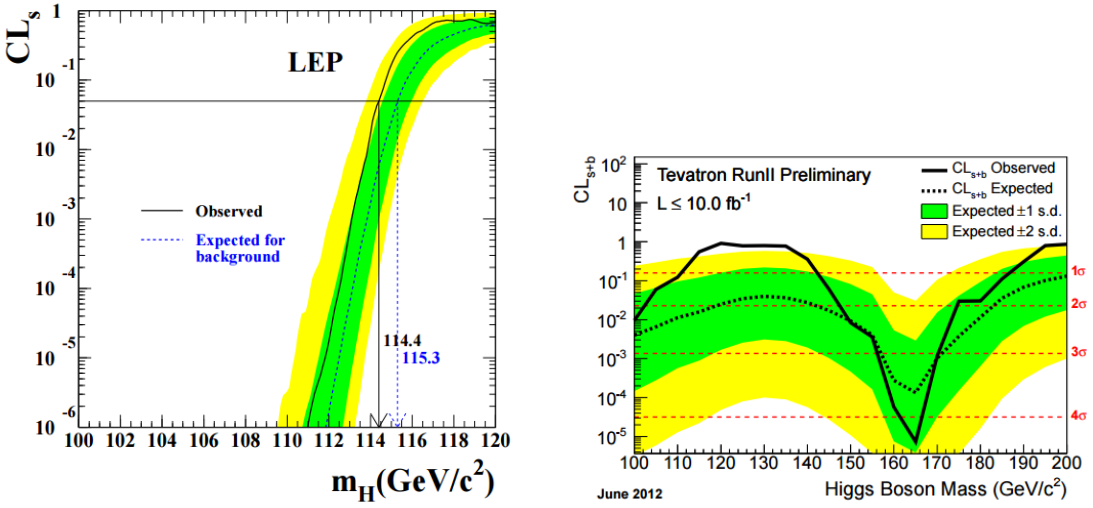

Figure 3.6: The ratio $CL_s = CL_{s+b}/CL_b$ for the signal plus background hypothesis (left). Solid line: observation; dashed line: median background expectation. The signal p-values CL_{s+b} as a function of the Higgs boson mass (in steps of $5\,GeV/c^2$), for the combination of the CDF and D0 analyses (right). Results from [?, 41]

marized in figure 3.7. Even though these results were investigating a parameter-space region close to the actual Higgs mass, the accelerators had reached their limits and were ultimately shut down and, in LEP case, dismantled to host the LHC.

3.2 Higgs production at LHC

In Chapter 2 we have seen the main characteristics of LHC. What we have omitted is how the accelerated particles interact and produce the rare processes shown in Chapter 1. In hadron colliders, like LHC and Tevatron, the interacting entities are not the accelerated particles themselves, but rather their components, gluons and quarks, either valence ones or in the vacuum sea. These only carry a fraction x of the proton momentum, that varies with the momentum transferred in the collision, as shown in figure 3.8.

All cross sections calculated in the perturbabive QCD (pQCD) framework for hadronic colliders like LHC use the factorization theorem, that separates the process-dependent

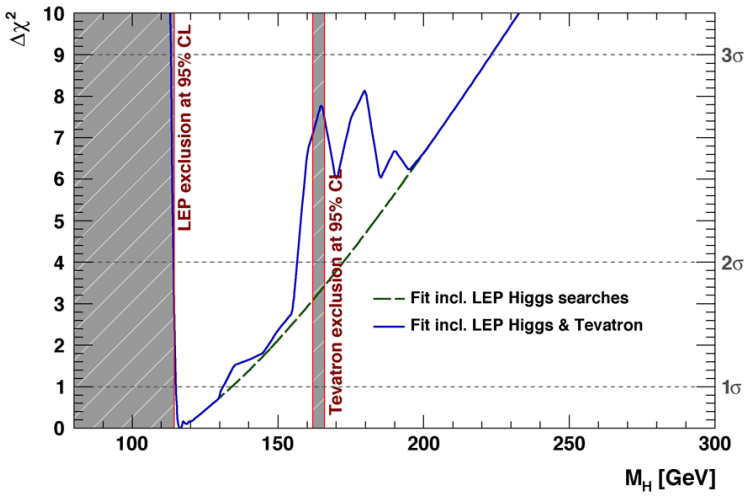

Figure 3.7: Global fit to all published data sensitive to the Higgs boson mass. This comprises direct searches as well as electroweak precision data. The left vertical axis shows goodness-of-fit relative to the minimum χ^2 value, while the right vertical axis shows σ values as a function of Higgs mass. The dashed line shows the situation before the Tevatron publications, while they are included in the solid line. The left shaded portion is the mass range excluded by LEP, and the central shaded region is the range excluded by the Tevatron. High masses are excluded by precision measurements of the weak mixing angle and the W mass, leaving only the range $115 - 150\,GeV/c^2$ for the mass of the Higgs boson [43].

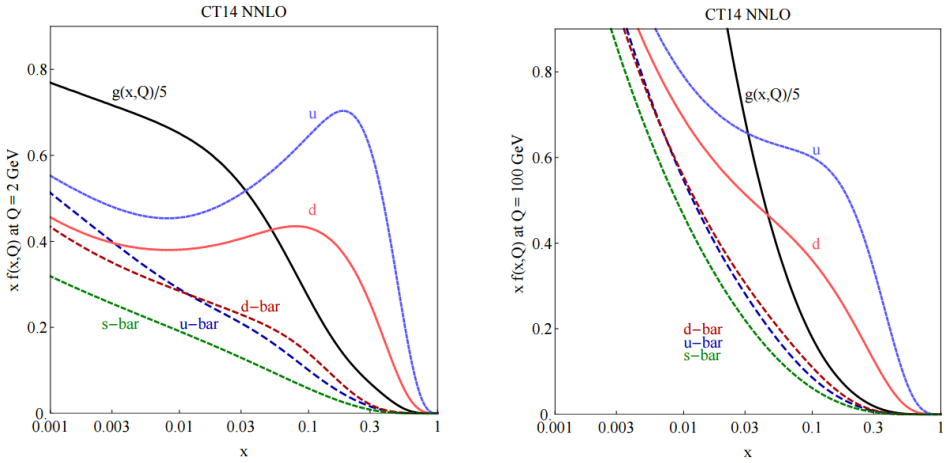

Figure 3.8: The CT14 parton distribution functions at $Q = 2GeV$ and $Q = 100GeV$ for $u, \bar{u}, d, \bar{d}, s = \bar{s}$, and g.

perturbative QCD calculable short-distance parton cross section and the universal long-distance functions through the factorization scale μ. This latter factor is taken into account by the parton distribution functions (PDF's), that map the probability of every virtual and valence component to have a given fraction x of the proton momentum. At leading order the rapidity of the reaction is $y = 0.5\ \ln(x_1/x_2)$, where x_i represents the fraction of the longitudinal momentum carried by a parton, and the center-of-mass energy is $\sqrt{s} = \sqrt{x_1 x_2 s_{pp}}$. The cross-section of the pp process is, then, the convolution of the Quantum Field Theory parton prediction with the PDF:

$$\sigma = \int dx_1 f_{q/p}(x_1, \mu^2) \int dx_2 f_{\bar{q}/\bar{p}}(x_2, \mu^2) \hat{\sigma}(x_1 p_1, x_2 p_2, \frac{Q^2}{\mu^2}). \tag{3.2}$$

PDFs have been an important part hadron collider measurements for the last decades, leading to to several dedicated experiments and measurements [44]:

- Deep Inelastic Scattering (DIS) experiments probe the low-energy, high-x region with very high statistics;

- the ZEUS and H1 experiments at the Hera $p-e$ collider [45] cover higher transferred momentum Q regions at lower x;

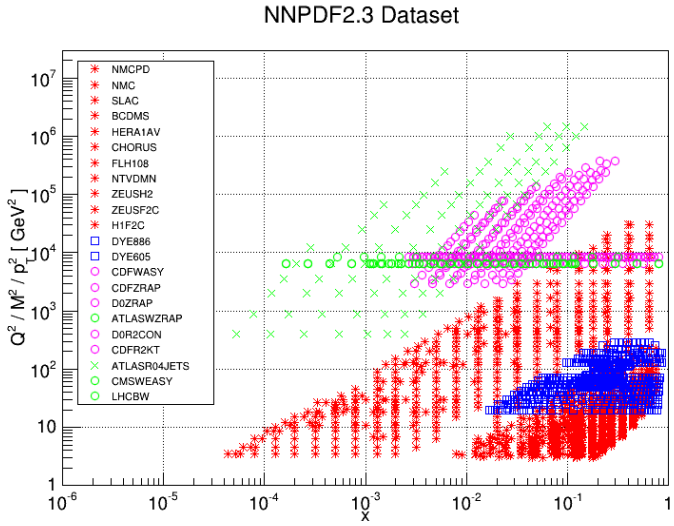

Figure 3.9: The kinematical coverage of the experimental data used in the NNPDF2.3 PDF determination [46].

- Tevatron and LHC precision measurements are providing precious inputs to the PDF modelling at higher energies, exploring high x ranges; this shows how well-known processes can help in reducing the uncertainty on rare measurements.

Figure 3.9 summarizes the regions covered by PDF experiments and LHC in the $x - Q$ plane [46], showing that a part of the regions probed at LHC is not covered by experimental measurements. Theoretical predictions cover the gap using DGLAP equations [47] at Next-to-Leading Order. The PDF sets used in this thesis are the MRST [48], NNPDF [46] and CTEQ [49] collaborations, that continue improving their predictions using new LHC data and experimenting new modellings.

Due to the topology of pp collisions, the main leading order production channels at LHC are:

- gluon-gluon fusion;
- vector boson fusion;
- Higgs-strahlung;

- associated production $t\bar{t}H$ (or $t\bar{t}$ fusion).

Figure 3.10 shows the Feynman diagrams for the aforesaid processes at tree level and figure 3.11 displays the production cross-section as a function of the mass of the Higgs boson.

For the scope of this thesis the process of interest is the $t\bar{t}H$ channel (in the dominant

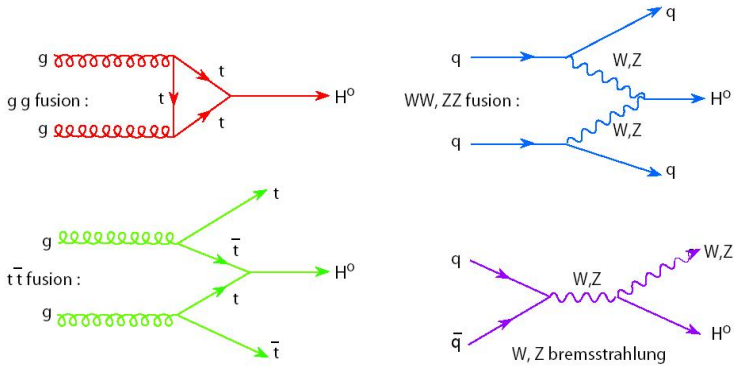

Figure 3.10: The production modes of the Higgs boson at LHC

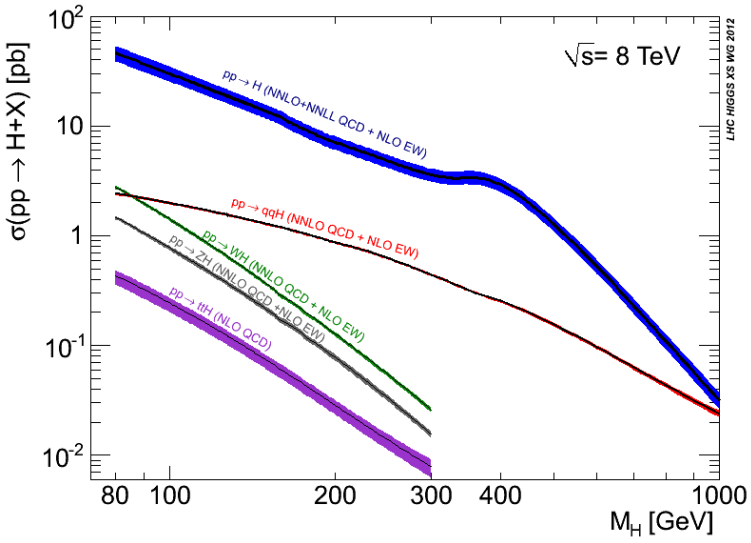

Figure 3.11: The production modes of the Higgs boson at LHC

gluon component) process. The Matrix Element that appears in this production cross

section is computed at Leading Order (LO) as:

$$M_{LO}^{gg} = \left(\frac{2}{3}C_1^{gg} + C_2^{gg} + C_3^{gg}\right)\left(M_{direct} + \frac{1}{2}M_{fusion}\right) + \\ + \left(\frac{2}{3}C_1^{gg} - C_2^{gg} + C_3^{gg}\right)\left(M_{crossed} - \frac{1}{2}M_{fusion}\right) \quad (3.3)$$

where C_1^{gg} corresponds to a coefficient for the colour-singlet state of the $t\bar{t}$ system, while C_2^{gg} and C_3^{gg} are the coefficients for the two different octet states; the matrix element terms proportional to M_{direct} correspond to the three "direct graphs", where two parallel gluons couple to the top-quark line (as in figure 3.10), the terms proportional to $M_{crossed}$ result from the direct graphs by crossing (interchanging) the two gluons and the terms proportional to M_{fusion} correspond to the gluon-fusion graphs. Form more details see [50].

The production cross-section of the different processes is calculated at 2 TeV, 7 TeV, 8 TeV and 14 TeV for a Higgs with mass $M_H = 125\,GeV$ in Table 3.1, showing that the largest contribution to inclusive analyses mostly derive from gluon-gluon fusion. The increase in cross-section for the $t\bar{t}H$ process between 8 and 14 TeV shows the potential of this channel in Run 2: With $\sim 1/5$ of the data taken at $\sqrt{s} = 8\,TeV$ it should be possible to have the same S/B significance with the $14\,TeV$ data.

$\sqrt{s}(TeV)$	Production cross section (in pb) for $m_H = 125\,GeV$					
-	ggF	VBF	WH	ZH	$t\bar{t}H$	total
1.96	$0.95^{+17\%}_{-17\%}$	$0.065^{+8\%}_{-7\%}$	$0.13^{+8\%}_{-8\%}$	$0.079^{+8\%}_{-8\%}$	$0.004^{+10\%}_{-10\%}$	1.23
7	$15.1^{+15\%}_{-15\%}$	$1.22^{+3\%}_{-2\%}$	$0.58^{+4\%}_{-4\%}$	$0.33^{+6\%}_{-6\%}$	$0.09^{+12\%}_{-18\%}$	17.4
8	$19.3^{+15\%}_{-15\%}$	$1.58^{+3\%}_{-2\%}$	$0.70^{+4\%}_{-5\%}$	$0.41^{+6\%}_{-6\%}$	$0.13^{+12\%}_{-18\%}$	22.1
14	$49.8^{+20\%}_{-15\%}$	$4.18^{+3\%}_{-3\%}$	$1.50^{+4\%}_{-4\%}$	$0.88^{+6\%}_{-5\%}$	$0.61^{+15\%}_{-28\%}$	57.0

Table 3.1: The SM Higgs boson production cross sections for $m_H = 125\,GeV$ in pp collisions, as a function of the centre of mass energy, $\sqrt{s}$ [51]

Decay channel	Branching ratio	Rel. uncertainty
$H \to \gamma\gamma$	2.28×10^{-3}	$^{+5.0\%}_{-4.9\%}$
$H \to ZZ$	2.64×10^{-2}	$^{+4.3\%}_{-4.1\%}$
$H \to W^+W^-$	2.15×10^{-1}	$^{+4.3\%}_{-4.2\%}$
$H \to \tau\tau$	6.32×10^{-2}	$^{+5.7\%}_{-5.7\%}$
$H \to b\bar{b}$	5.77×10^{-1}	$^{+3.2\%}_{-3.3\%}$
$H \to Z\gamma$	1.54×10^{-3}	$^{+9.0\%}_{-8.9\%}$
$H \to \mu\mu$	2.19×10^{-4}	$^{+6.0\%}_{-5.9\%}$

Table 3.2: The branching ratios and the relative uncertainty for a SM Higgs boson with $m_H = 125\,GeV$ [51]

3.3 The Higgs decay channels

The Higgs boson is a particle with a very short lifetime. It decays in many different ways, each with a probability, the so-called Branching Ratio (BR), that depends on the boson and fermion couplings described in chapter 1. Higher masses lead to higher BR's, off-shell decays are suppressed and vector boson decays are enhanced due to the quartic mass dependence of boson couplings. Moreover, small branching ratios can be found for Higgs decays into photons and gluons only because of loop diagrams, thus yielding a lower order contribution to the Higgs decay width. The BR of the Higgs boson as a function of its mass are shown in figure 3.3.
For a Higgs boson mass of $125.5 \pm 1\,GeV$ by ATLAS and CMS, the theoretical BRs are fixed to the values displayed in Table 3.2.

The different experimental analysis channels are identified on the base of the Higgs decays, since each provides a different experimental signature.

3.4 The discovery by ATLAS and CMS

In 2009 the first proton started to circulate in the Large Hadron Collider and its experiments started taking data. In 2010 LHC reached the energy of $\sqrt{s} = 7\,TeV$, which was increased to $8\,TeV$ at the end of 2011. In this phase, the first and simplest analy-

sis were already pointing out an unknown resonance that could correspond to the new particle, but it was in only 2012 that the discovery could be officially claimed. In July the amount of gathered data was sufficient to produce a significant result and the analysis were accurate enough to ensure low systematic uncertainties and good background prediction. Thanks to the clean signal, the first published channels were $H \to \gamma\gamma$ and $H \to ZZ^*$ [8] [52], both produced in the gluon-gluon fusion channel, that has the highest cross-section at $7 - 8\,TeV$. The signature for these channels are, respectively, two back-to-back photons and 4 isolated leptons in the $l^+l^-l'^+l'^-$ topology. Figure 3.12 shows the ATLAS invariant mass distribution in the $H \to \gamma\gamma$ and $H \to ZZ^* \to 4l$ channel. These have a high resolution in mass reconstruction, since there are no jets or neutrinos in the final state. The higher-statistics $H \to WW*$ was used to confirm the results, but its mass resolution is poor due to the missing energy component. The 5σ signal over background excess threshold was reached for a mass of $126.0 \pm 0.4 \pm 0.4\,GeV$.

The cross section $\sigma \times BR$ was also measured and compared with the SM prediction in the combined channel. The signal strength $\mu = \sigma_{exp}/\sigma_{SM} = 1.4 \pm 0.3$ was observed, as displayed in figure 3.13, showing that data are compatible with the SM prediction.

With the discovery of the Higgs boson and the measurement of its parameters, the SM is completed but it remains to be seen is it is valid up to much higher energies. Moreover, the Higgs introduces a new sort interaction, based on the mass of the particle: processes involving Higgs bosons become new probes to test the SM and study BSM physics.

3.5 The associated production $t\bar{t}H$

In chapter 1 we have seen the importance of Higgs couplings and Beyond Standard Model (BSM) effective theories measurements. The $t\bar{t}H$ channel is especially useful in this field, since the production cross section is the only one dependent, at tree level, from the SM top quark coupling. Going into greater detail than Section 3.2, the $t\bar{t}H$ associated production cross section at a centre of mass energy $\sqrt{s} = 8\,TeV$ is calculated [54] to be:

$$\sigma = 129^{+5}_{-12}(\text{scale}) \pm 10(\text{PDF})fb \tag{3.4}$$

At $\sqrt{s} = 13\,TeV$, this grows by approximately a factor 4, the largest increase among any SM process. In ATLAS we differentiate analysis on the basis of the event topology,

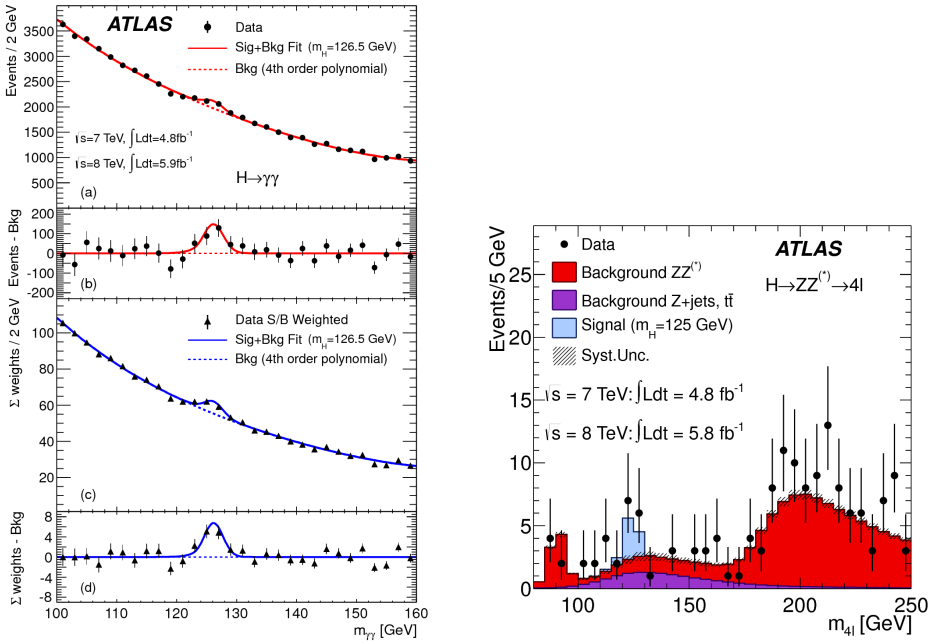

Figure 3.12: On the left, we show the distributions of the invariant mass of diphoton candidates after all selections for the combined 7 TeV and 8 TeV data sample. The inclusive sample is shown at the top and a weighted version of the same sample at the bottom; the weights are explained in [8]. The result of a fit to the data of the sum of a signal component fixed to $m_H = 126.5\,GeV$ and a background component described by a fourth-order Bernstein polynomial is superimposed. The residuals of the data and weighted data with respect to the respective fitted background component are displayed in b) and d). On the right, distribution of the four-lepton invariant mass, m_{4l}, for the selected candidates, compared to the background expectation in the 80 to 250 GeV mass range, for the combination of the $\sqrt{s} = 7\,TeV$ and $\sqrt{s} = 8\,TeV$ data. The signal expectation for a SM Higgs with $m_H = 125\,GeV$ is also shown [8].

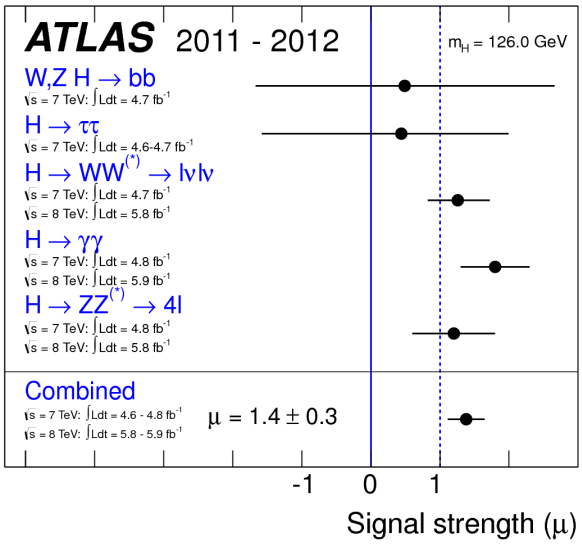

Figure 3.13: Measurements of the signal strength parameter μ for $m_H = 126\,GeV$ for the individual channels and their combination [53].

in particular on the Higgs decays. The first results on this production channel were published for the channels:

- $H \to \gamma\gamma$ [55], considered the "golden" one for single-Higgs due to the clean signature given by the two almost back-to-back energy deposits in the Electromagnetic Calorimeter. The low branching ratio, on the other hand, reduces the statistic gathered by the experiment. Depending on top decays we distinguish between leptonic (single and double) and pure hadronic channels. The cut-based analysis of the $20.3 fb^{-1}$ data gathered in 2012 yields the results in figure 3.14, where we observe no excess over the background expected in the Standard Model. A combined 95% CL limit is set on $t\bar{t}H$ $(H \to \gamma\gamma)$ production cross-section 5-6 times the SM prediction.

- $H \to b\bar{b}$ [56], the main decay channel of the Higgs boson yields high statistics but a high background due to $t\bar{t}$ + jet (in particular $b\bar{b}$) events. Due to the complicated background, multi-variate methods are exploited. In particular, Neural Networks implemented by the NeuroBayes [57] package are used. The events are categorized

on three bases: number of jets, number of b-jets and single lepton and di-lepton distinction. Figure 3.15 shows no excess from Standard Model predictions, with a signal strength $\mu = \sigma/\sigma_{SM} = 1.7 \pm 1.4$. Consequently, a 95% confidence level limit of 4.1 times the SM cross-section prediction is set.

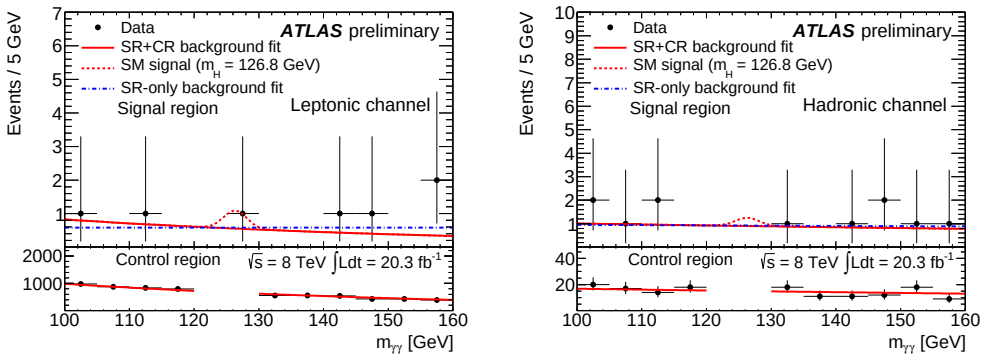

(a) (b)

Figure 3.14: The observed number of signal and background events in the $t\bar{t}H$, $H \to \gamma\gamma$ channel, together with the expected signal from the theory. Leptonic and hadronic refer to $t\bar{t}$ decays.

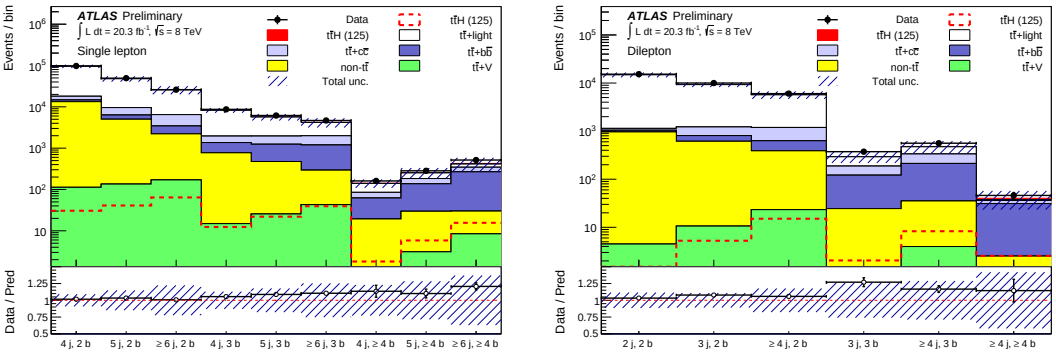

(a) (b)

Figure 3.15: The observed number of signal and background events in the $t\bar{t}H$, $H \to b\bar{b}$ channel, for the different analysis signatures [56]

Both analyses thus pose limits on the SM parameters, but these are not particularly stringent due to the limited Run 1 statistics. To improve this result, the multi-leptonic channels are also analysed, the main topic of the next chapter. The Higgs boson decay contributions to this channel are: $H \to ZZ^*$, $H \to WW^*$ and $H \to \tau\tau$. Another group of decay channels under study is the "all-hadronic", in which τ leptons and vector bosons all decay hadronically and produce jets. The advantage of these channels is the low missing energy, thus having the possibility to reconstruct the mass of the parent particles, but they are limited by a very high background. We will see in the next chapter how the ttH multiletpon channel will sensibly improve the limits found in the $H \to \gamma\gamma$ and $H \to b\bar{b}$ analyses.

Chapter 4

Search for $t\bar{t}H$ in multi-lepton final states in Run I

4.1 Introduction

As we have seen in the previous chapters, the observation of the associated production of a Higgs boson with a pair of top quarks would allow a direct tree-level measurement of the top-Higgs Yukawa coupling, otherwise accessible only through loop effects. After the searches in the $H \to \gamma\gamma$ and $H \to b\bar{b}$ decay channels, the analysis is extended to the multileptonic final states [58]. The integrated luminosity is not yet enough, considering the low $8\,TeV$ cross-section, to produce really significant result, so the whole analysis is also a preparation for the Run II data-taking, where the number of signal events is expected to rise by a factor of ~ 20. The five final states considered are: two same-sign (SS) light leptons (e or μ) with no additional hadronically decaying tau ($2lSS0\tau$); three light leptons ($3l$); two same-sign light leptons with one hadronically decaying tau ($2lSS1\tau$); four light leptons ($4l$); one light lepton with two hadronically-decaying tau candidates ($1l2\tau$). Requesting large jet multiplicity and the presence of at least one b-tagged jet suppresses the boson and diboson backgrounds, while asking for SS or a high number of leptons reduces QCD and t and $t\bar{t}$ backgrounds. The analysis is not exclusive in the Higgs decay channels, but the ones that produce these experimental signatures are mainly $H \to WW^*$, $\tau\tau$ and ZZ^*; a great care has been given to the orthogonality of

these channels. The analysis uses the data collected by ATLAS in 2012 at $\sqrt{s} = 8\,TeV$, for a total integrated luminosity of $20.3\,fb^{-1}$. The final measurement we want to obtain is the signal strength $\mu = \sigma_{t\bar{t}H\to\text{multileptons}}/\sigma_{SM}$, representing the deviation of the experimental data from the theory (SM hypothesis: $\mu = 1$).
In section 4.1 the theoretical framework and the Monte Carlo simulations used are detailed. In the following section the object selection is explained, together with the reconstruction techniques used for those objects. Section 4.3 details the event selection for the different signal channels, followed by sections 4.4 and 4.5 that contain respectively the methods used for background estimation and the systematic uncertainty studies. Final results are shown in section 4.6.

4.2 Theoretical studies and MC production

The production cross section for the $t\bar{t}H$ production at LHC has been introduced in chapter 3. For this analysis the calculation was done at next-to-leading order (NLO), yielding $\sigma(t\bar{t}H) = 129^{+5}_{-12}(\text{scale}) \pm 10(\text{PDF})\,fb$ at $\sqrt{s} = 8\,TeV$, with the Higgs branching ratios computed at next-to-next-to-leading order (NNLO), considering $M_H = 125\,GeV$. The uncertainties on these calculations were evaluated increasing and decreasing renormalization and factorization scales by a factor 2 with respect to the nominal values and taking into account the uncertainty associated with the PDF's [54].
The choice of a different Monte Carlo event generator at the different generation levels (matrix-element, showering or hadronization) or PDF set for any given process is determined by two factors: availability of the higher order samples (in particular NLO have become available for many process recently) and comparison with data in dedicated control regions, performed by the analysis team or in other analyses.
In this analysis every process except $t\bar{t}H \to$ multileptons is considered background and set to its SM rate, including the associated production of a Higgs with a single top quark such as $tHqb$ and tHW, whose cross-sections are calculated using MG5_AMC@NLO [59]. The results are, respectively, $\sigma(tHqb) = 17.2^{+0.8+1.2}_{-1.4-0.9}\,fb$ and $\sigma(tHW) = 4.7^{+0.4+0.8}_{-0.3-0.6}\,fb$. The production of $t\bar{t}V$, where $V = W$ or $Z/\gamma^* \to ll$ is a major irreducible background to

our signal. NLO cross sections are used for $t\bar{t}V$ [60,61], with MG5_AMC@NLO used to produce the QCD scale and PDF-related uncertainties, yielding $\sigma(t\bar{t}W) = 232 \pm 28 \pm 18\, fb$ and $\sigma(t\bar{t}Z) = 206 \pm 23 \pm 18\, fb$. The associated production of a single top quark and a Z boson is also a background source for some channels. The NLO calculations for the relevant processes are $\sigma(tZ) = 160 \pm 7 \pm 11\, fb$ and $\sigma(\bar{t}Z) = 76 \pm 4 \pm 5\, fb$. The leading order cross-section for the tWZ production is computed with MadGraph v5 [62], yielding $\sigma = 4.1\, fb$.

The cross section for the production of diboson pairs is computed using MCFM [63], including contributions from virtual photons and off-shell bosons. The uncertainty on these processes is dominated by the acceptance in the signal and control regions.

The $t\bar{t}$ process is one of the most important background processes in our analysis, so its cross section is determined at NNLO in QCD, including resummation of next-to-next-to-leading logarithmic soft gluon terms using Top++ [64]. At $8\, TeV$ this results in $\sigma(t\bar{t}) = 253^{+13}_{-15}\, pb$. Single top samples are normalized to the NNLO theoretical cross section using the PDF set MSTW2008 and V+jets samples are normalized using NNLO cross sections computed by FEWZ [65].

Monte Carlo samples are produced for each signal and background process using different generators, depending on how accurate these simulations need to be. For the $t\bar{t}H$ signal the PowHel [66] framework, that combines the POWHEG-Box [67] and the HELAC-NLO package [68] samples, is used, containing all Higgs boson decays with branching ratios at NNLO values. The PDF sets used to produce them are CT10 NLO [69], using $M_H = 125\, GeV$ and $M_t = 172.5\, GeV$. PowHel uses matrix elements from HELAC-Oneloop [68], interfacing the with Pythia 8.1 [70] through Powheg BOX 1.0 [67] for showering and hadronization, where Pythia uses the CTEQ6L1 PDF's [71]and AU2 [72] underlying event tune.

Concerning tH events, the $tHqb$ sample is generated at LO using MadGraph + Pythia8.1, while tHW events are produced at NLO using MG5_AMC@NLO + Herwig++ [73] for parton showering. The CT10 PDF set is used.

$t\bar{t}V$ events are generated with MadGraph+Pythia 6.425 using CTEQ6L1 PDF's and the AUET2B tune. For $t\bar{t}W$, the events are generated with up to two extra partons, while for $t\bar{t}Z$ only up to a single extra parton at Matrix Element is generated. The tZ process

is similarly generated, but without extra partons. Since these processes are particularly important, being an irreducible background, additional simulations were generated using different generators: MG5_AMC@NLO at NLO +Pythia8.1 and Herwig++ and in addition Sherpa2.1.1 [74] in both LO merged and NLO mode matched to the internal parton shower.

Diboson WW and ZZ production is simulated using Sherpa1.4, while Powheg+Pythia8.1 is used for $q\bar{q}, qg \to ZZ$ and GG2ZZ2.0 [75] for $gg \to ZZ$. Vector boson fusion with diboson final states is generated with Sherpa, including γ^* and off-shell Z contributions as well as additional partons in the final state and b and c quark mass effects. Comparisons made by the analysis team showed that Sherpa has a better agreement with data, in particular for WZ processes.

Samples for single top production, s-channel, t-channel and Wt, were generated using Powheg with CT10 PDF's interfaced with Pythia6.425+CTEQ6L1 with the Perugia2011C underlying event [76]. The different V+jets processes are generated with Alpgen 2.14 [77] at LO with CT10 PDF's. Parton showering is handled by Pythia 6.425. The resulting samples are normalized by comparing the b-jet spectrum with data. Table 4.1 summarizes MC samples used in the analysis.

Additional samples were generated also for cross-check, optimization studies and to evaluate the composition of non-prompt lepton backgrounds, in particular a $t\bar{t}$+jets sample was generated at NLO with Powheg with CT10 PDF's interfaced with Pythia 6.425 using the CTEQ6L1 PDF set. Small corrections to p_T spectrum were applied, based on the discrepancy between MC and the $7\,TeV$ data.

After showering and hadronization all events are passed through the ATLAS detector simulation, using the full GEANT4 [78] or parametrized calorimeter showers together with GEANT4 for tracking simulation. Minimum bias pile-up interactions are added to signal and background events using Pythia 8.1 with MSTW2008 PDF's, scaled to match the observed data. Contributions of pile-up coming from neighbouring bunch crossing are also added in the simulations.

Process	ME Generator	Parton Shower	PDF	Tune
$t\bar{t}H$	HELAC-Oneloop [41, 42] + POWHEG-BOX [48-50]	PYTHIA 8 [43]	CT10 [44]/CTEQ6L1 [45, 46]	AU2 [47]
$tHqb$	MADGRAPH [33]	PYTHIA 8	CT10	AU2
tHW	MG5_AMC@NLO [29]	HERWIG++ [51]	CT10/MRST LO** [52]	UE-EE-4 [53]
$t\bar{t}W$ + $\leq$ 2 partons	MADGRAPH	PYTHIA 6 [54]	CTEQ6L1	AUET2B [55]
$t\bar{t}(Z/\gamma^*)$ + $\leq$ 1 parton	MADGRAPH	PYTHIA 6	CTEQ6L1	AUET2B
$t(Z/\gamma^*)$	MADGRAPH	PYTHIA 6	CTEQ6L1	AUET2B
$q\bar{q}, qg \to WW, WZ$	SHERPA [56]	SHERPA	CT10	SHERPA default
$qq \to qqWW, qqWZ, qqZZ$	SHERPA	SHERPA	CT10	SHERPA default
$q\bar{q}, qg \to ZZ$	POWHEG-BOX [57]	PYTHIA 8	CT10	AU2
$gg \to ZZ$	GG2ZZ [58]	HERWIG [59]	CT10	AUET2 [60]
$t\bar{t}$	POWHEG-BOX [61]	PYTHIA 6	CT10/CTEQ6L1	Perugia2011C [62]
s-, t-channel, Wt single top	POWHEG-BOX [63, 64]	PYTHIA 6	CT10/CTEQ6L1	Perugia2011C
$Z \to \ell^+\ell^-$ + $\leq$ 5 partons	ALPGEN [65]	PYTHIA 6	CTEQ6L1	Perugia2011C
$W \to \ell\nu$ + $\leq$ 5 partons	ALPGEN	PYTHIA 6	CTEQ6L1	Perugia2011C

Table 4.1: Configurations used for event generation of signal and background processes. If only one parton distribution function is shown, the same one is used for both the matrix element and parton shower generators; if two are shown, the first is used for the matrix element calculation and the second for the parton shower. "Tune" refers to the underlying-event tune of the parton shower generator. "Pythia 6" refers to version 6.425; "Pythia 8" refers to version 8.1; "Herwig++" refers to version 2.6; "MadGraph" refers to version 5; "Alpgen" refers to version 2.14; "Sherpa" refers to version 1.4; "gg2ZZ" refers to version 2.0.

4.3 Object reconstruction and selection

The very first steps of the analysis chain are the object reconstructions that will be used to identify decayed particles and hence signal and background events. Since in ATLAS objects can be charged particles, leptons, clusters, jets, missing E_T (MET), τ, these are reconstructed, identified and selected using different techniques that can be tuned to our specific kinematics. We use the reconstruction algorithms provided by the detector for every object on the basis of the recommendations of the performance groups, then the object selections are optimized using MC simulations to get the best signal.
Object reconstruction consists in grouping the signals of the particle detectors in known patterns that can be associated to physical particles that might have produced the signals and extracting their kinematic properties. This is accomplished through different methods, depending on the objects and the aim of the reconstruction: a fast reconstruction for triggering purposes or a precise one aimed at physics analysis. The ATLAS experiment uses the information from the inner detector (charged particles), from the calorimeters and from the muon spectrometer (for muons) to identify and precisely reconstruct particles produced in the pp collisions.

4.3.1 Track reconstruction

Track reconstruction is composed of two parts: track finding, where a track is identified, and track fitting, where the track shape is improved and the kinematic parameters are extracted. There are several different methods that can be used to reconstruct tracks in ATLAS. The main track finding strategy is the "inside-out" strategy, where a short track, called a "seed", is first identified in the pixel layers closest to the interaction point and then it is expanded towards the outer layers. The first step is accomplished through a patter recognition algorithm: three silicon space-points, which can be a cluster of pixel-hits or an SCT strip crossing, must be compatible with a pre-determined pattern representing a possible track with $p_T > 500\,MeV$. The track is then prolonged towards the outer layers using a simple Kalman [79] filter and other hits can be associated to it. Only tracks having at least 7 silicon hits are processed in the next steps. An algorithm

designed to remove duplicated tracks and fake tracks is then applied, favouring the best tracks having more consecutive hits. The last step in track finding is to match the seeds with TRT measurements, assigning signals close to the silicon track and re-fitting the entire track.
After the first reconstruction made by the detector, off-line track fitting is implemented using an accurate Kalman filter or with a global least-squares fit method. The results obtained using the two methods were shown to be identical [80].

4.3.2 Electrons

An energy cluster in the EM calorimeter associated with a reconstructed track in the inner detector is defined as an electron candidate. These candidates must have $|\eta_{CL}| < 2.47$, with the calorimeter transition region, $1.37 < |\eta_{CL}| < 1.52$, excluded. To distinguish electrons and hadronic showers, a multivariate discriminant based on shower shape and track information is used [81], selecting electrons that pass a *very tight* working point (WP)[1] cut. Electrons with $E_T < 10\,GeV$ are excluded. In the signal region we want to have only prompt electrons, directly coming from W, Z and τ decays, and thus two isolation cuts are applied. The first one looks at the sum of the transverse energies (E_T^{cone}) in calorimeter cells within a cone of radius $\Delta R = 0.2$ around the particle trajectory. This energy does not include the energy released by the electron itself and is corrected for ambient energy contamination and leakage from the electromagnetic shower. The second cut is based on the p_T^{cone}, the sum of transverse momentum of tracks with $p_T > 1\,GeV$ found in a cone of the same radius $\Delta R = 0.2$ This cut is more robust against pile-up background. Both cuts require these quantities to be less than $0.05 \times p_T$. Two more cuts are applied to ensure that the electron comes from the interaction vertex: the longitudinal impact parameter of the track, multiplied by $\sin\theta$, where θ is the polar angle, must be $|z_0 \sin\theta| < 1\,mm$; the transverse impact parameter divided by its estimated uncertainty is required to be $\left|\frac{d_0}{\sigma(d_0)}\right| < 4$ to be compatible with being generated in the interaction

[1] A Working Points is a reference value used to represents an ensemble of other variable values that together define a non-linear cut. For example a combination of variables defines if a lepton was reconstructed properly: algorithms used, detector requirements. Working Points allow the user to choose between certain combinations of these variables.

vertex or coming from the decay of short lived particles [82].

4.3.3 Muons

Muon candidates can be reconstructed from inner detector tracks, muon spectrometer tracks or, as was used in this analysis, a combination of the two. Candidates must have pseudorapidity $|\eta| < 2.5$ and $p_T > 10\,GeV$. Moreover, the same isolation cuts defined for electrons are applied: $|E_T^{cone}/p_T| < 0.1/p_T^{muon}$ and $|p_T^{cone}/p_T| < 0.1/p_T^{muon}$. Similarly to electrons, we require $|z_0 \sin\theta| < 1\,mm$ and $\left|\frac{d_0}{\sigma(d_0)}\right| < 3$ [83].

4.3.4 Hadronic τ

The visible part (an invisible ν_τ is always produced) of the τ candidates decay into hadrons (τ_{had}) is identified through calorimeter clusters, both in the electromagnetic and hadronic calorimeters. Kinematic cuts on τs are $p_T > 25\,GeV$ and $|\eta| < 2.4$. Additionally, τ candidates must have exactly 1 or 3 associated charged tracks, with a total charge of ± 1. A boosted decision tree multivariate approach is used to combine calorimeter and tracking variables for τ reconstruction. Similarly, another BDT is used to reject electrons as a hadronically decaying τ lepton [84, 85].

4.3.5 Hadrons and jets

Jet reconstruction starts from calibrated topological clusters built from the association of the energy deposit in the hadronic calorimeter cells; noise is suppressed through a threshold on energy deposits in the cells, which in turn requires a correction for the lost energy. A matching with the EM calorimeter cells is used to separate the EM and hadronic components (they display a different behaviour) before jet reconstruction. The anti-k_t clustering algorithm is used, which associates tracks and calorimeter clusters within a conic area of radius parameter $R < 0.4$ (starting from the interaction point) [86–88]. A local cluster calibration scheme is applied. Figure 4.1 compares the most used clustering algorithms, showing the resulting hard-jet active areas.

MC simulations were used to derive energy and η-dependent calibration factors, while

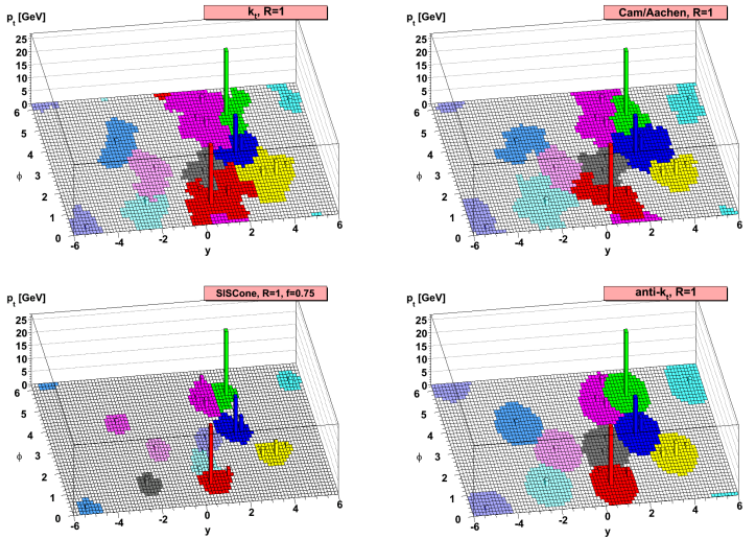

Figure 4.1: A sample parton-level event (generated with Herwig [73]), together with many random soft "ghosts", clustered with four different jet algorithms, illustrating the "active" catchment areas of the resulting hard jets

the $in-situ$ technique was used to calculate additional corrections. After these calibrations, the cuts $p_T > 25\,GeV$ and $|\eta| < 2.5$ are applied. Additionally, for jets with $p_T < 50\,GeV$ and $|\eta| < 2.4$, having a higher probability of coming from different interactions, another cut is applied to reduce contamination from pile-up jets: the scalar sum of the p_T of tracks matched to the jet and originating from the primary vertex must be at least 50% of the scalar sum of the p_T of all tracks matched to the jet.
In our analysis we distinguish between jets coming from light or charm quarks from jets having a top or bottom origin. Therefore it is very important the jet b-tagging, which is accomplished using a multivariate discriminant [89] that combines topological properties of secondary and tertiary decay vertices with the impact parameters of displaced jet tracks. Figure 4.2 shows a scheme of a b-jet structure (left) and the 2-dimensional density of the minimum $\Delta R_{b,q}$ in top decay events $t \to Wb \to qq'b$ as a function the top p_T.

An overall 70% b-tagging efficiency working point is used to identify b-jets, with the distribution as a function of ΔR_{b-q} shown in figure 4.3. At this working point there is a light jet mis-tag rate of 1% and a charm jet rejection factor of 5, as determined using $t\bar{t}$

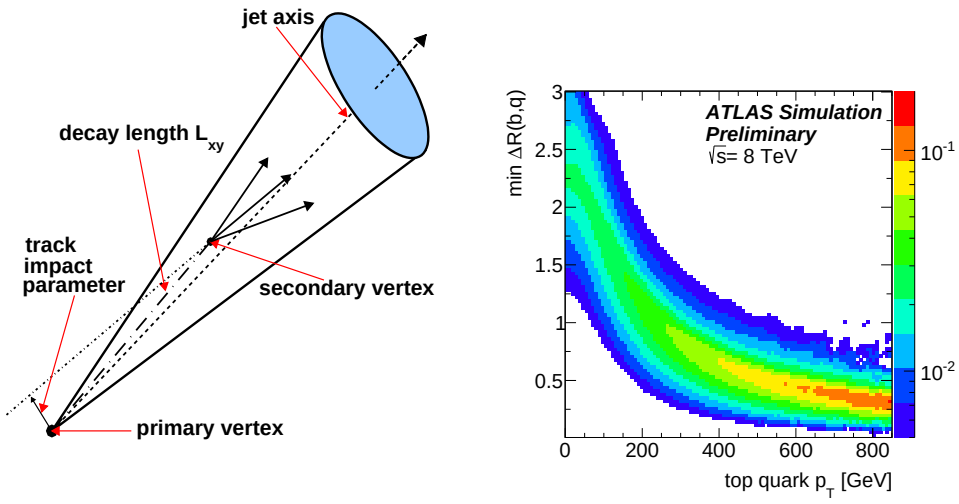

Figure 4.2: Schematic view of a b-hadron decay inside a jet (left) resulting in a secondary vertex with three charged particle tracks. The vertex is significantly displaced with respect to the primary vertex, thus the decay length is macroscopic and well measurable. The track impact parameter, which is the distance of closest approach between the extrapolation of the track and the primary vertex, is shown in addition for one of the secondary tracks. Smallest distance ΔR (right) in the $\eta\phi$-plane between the b-quark and the decay products of the W-boson in $t \to Wb \to qq'b$ decays as a function of the top quark p_T. The distributions are normalised column-wise in the p_T bins and the color coding corresponds to the fraction of considered top quarks. The distribution is obtained from $t\bar{t}$ decays simulated using POWHEG+PYTHIA.

MC simulations. Contrarily to light jet cuts, only b-jets with $|\eta| < 2.4$ are considered in this analysis. Efficiency and mis-tag rates are measured using data, as are the correction factors applied to the simulated efficiency.

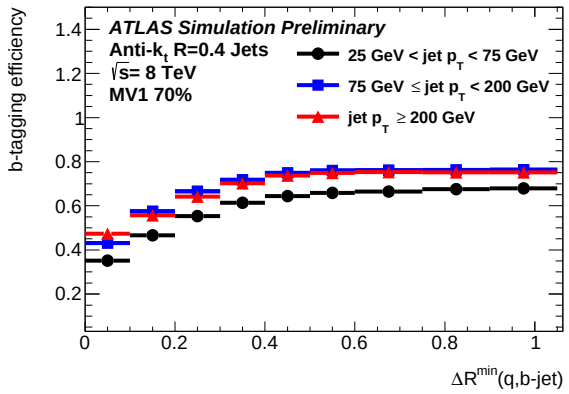

Figure 4.3: The b-tagging efficiencies' dependence on the ΔR_{min} between the b-quark jets and the hadronic decay products of the W-boson stemming from top quark decays for the MV1 algorithm. The chosen working point corresponds to an overall b-tagging efficiency of 70%. Jets are classified into three different p_T regions and studied separately.

4.4 Overlap removal

Sometimes different objects are reconstructed from the same clusters and tracks, identified using different algorithms that do not take each other into account. These objects need to be removed to avoid multiple object counting in the event in a procedure called Overlap Removal (OR), summarized in table 4.5. Due to this, if two electrons are within $\Delta R = 0.1$ of each other, the one with the lowest p_T is discarded. If an electron is within $\Delta R = 0.1$ of a muon, it is discarded, since it's likely identified from a track that actually belongs to a muon. If an electron and a jet are within $\Delta R = 0.3$, the jet is discarded, since it was reconstructed from a calorimeter cluster produced by the electron. Similarly, τs are discarded if within $\Delta R = 0.1$ of an electron or muon.
Overlap removal can also be used to remove decay products of prompt objects. This is

the case for muons and jets, where a muon within $\Delta R = 0.04 + \frac{10\,GeV}{p_T^\mu}$ of a jet is supposed to be produced during hadron decays and is discarded. Similarly, jets are discarded if within $\Delta R = 0.3$ of a hadronic τ.

Remove	**Overlap with**	**Cone size (Δ R)**
electron (low p_T)	electron	0.1
electron	muon	0.1
jet	electron	0.3
muon	jet	$0.04 + 10/p_T^\mu$
tau	electron or muon	0.1
jet	tau	0.3

Table 4.2: Summary of overlap removal between electrons, muons, taus and jets.

4.5 Event Selection and identification

In this section we select $t\bar{t}H$ events with leptonic final states. Because of this we use single-lepton triggers, choosing the ones with the lowest p_T to analyse the maximum possible parameter space. For each lepton type we use an isolated trigger with $p_T > 24\,GeV$ and a higher-p_T, non-isolated lepton trigger: EF_e24vhi_medium1, EF_e60_medium1, EF_mu24i_tight or EF_mu36_tight. Here the "i" stands for isolated. To reach the plateau of maximum efficiency even for the lowest triggers, the triggering lepton must have $p_T > 25\,GeV$. Since the main reducible background for our signal comes from $t\bar{t}$ events, selections are studied to reduce this contribution, using final states that cannot be produced by $t\bar{t}$ events, such as requiring a high number of leptons or two leptons of the same sign. The analysis channels are classified on the basis of the lepton and τ_{had} multiplicities to avoid any overlap. With this purpose leptons are selected as in the previous section, with an additional $p_T < 10\,GeV$ cut. Table 4.3 shows the analysis categories with the composition of the associated signal regions based on Higgs decays: two leptons of the same sign and no hadronic tau ($2lSS0\tau$), three leptons ($3l$), two same sign leptons produced together with a hadronic tau ($2lSS1\tau$), four light leptons ($4l$) and

	Higgs boson decay mode			
Category	WW^*	$\tau\tau$	ZZ^*	Other
$2\ell 0\tau_{\text{had}}$	80%	15%	3%	2%
3ℓ	74%	15%	7%	4%
$2\ell 1\tau_{\text{had}}$	35%	62%	2%	1%
4ℓ	69%	14%	14%	4%
$1\ell 2\tau_{\text{had}}$	4%	93%	0%	3%

Table 4.3: Fraction of expected $t\bar{t}H$ signal arising from different Higgs boson decay modes in each analysis category. The six $2l0\tau$ categories are combined together, as are the two $4l$ categories. The decays contributing to the "other" column are dominantly $H \to \mu\mu$ and $H \to bb$. Rows may not add to 100% due to rounding.

a single lepton with two hadronic taus ($1l2\tau$). The categories counting τ_{had} are mostly the result of $H \to \tau\tau$ decays, while the other channels mainly come from $H \to WW^*$ decays and secondarily from $H \to ZZ^*$ decays. Selections are completely orthogonal, to ensure no overlap between signal regions. The overlap with analysis studying gluon fusion, vector boson fusion and associated VH production mechanisms is negligible.

4.5.1 $2lSS0\tau$ category

The signal region for this channel is identified by two light leptons of the same charge sign. Events containing a hadronic τ that passes all the object selection cuts are vetoed. Subsequent lepton selection is tightened with respect to the common object selection: the leading lepton must have $p_T > 25\,GeV$ and the sub-leading lepton is required to have $p_T > 20\,GeV$, while the isolation on both leptons is tightened to $E_T^{cone}/p_T < 0.05$ and $p_T^{cone}/p_T < 0.05$. To reduce the contamination from opposite sign events where one of the electrons has its charge sign mis-reconstructed, electrons must have $|\eta| < 1.37$.
For this channel a minimum of 4 jets is requested, to suppress most of the $t\bar{t}$+jets and $t\bar{t}W$ background. At least one of these jets must be a b-jet, to remove diboson and single-boson background. This signal channel is further categorized on the basis of the lepton flavour (ee, $e\mu$ and $\mu\mu$) and the number of jets (exactly four or at least five), in order to increase the signal to background ratio and, thus, the channel sensitivity.
This is the analysis channel on which we focus the most in what follows.

4.5.2 $3l$ category

This signal region is defined by exactly three leptons selected with the cuts detailed in the previous section, with a total charge of ± 1, and is inclusive with respect to the number of τ_{had}, since no veto is applied. Candidate events in this region mostly come from opposite sign events with an additional non-prompt lepton, so an additional $p_T > 20GeV$ cut is imposed on the same sign leptons to suppress this background source. Similarly to the previous channel, a minimum of four jets and a b-tagged jet or, in alternative, exactly 3 jets and 2 b-jets, to suppress boson and diboson background. To reduce contamination from the $t\bar{t}Z$ a veto is imposed on events where a same-flavor, opposite sign couple of leptons has an invariant mass within $10\,GeV$ of the Z mass peak, as well as when the invariant mass is below $12\,GeV$, to avoid resonant background processes.

4.5.3 $2lSS1\tau$ category

Events selected in this channel must have exactly two same sign leptons with the additional requirement on the leading one of $p_T > 25\,GeV$ and on the sub-leading of $p_T > 15\,GeV$. The channel is defined by having exactly one single τ_{had}. As for the previous channel, 4 jets and a b-jet are required to suppress $t\bar{t}$+jets and $t\bar{t}V$ background. Again, events where the dilepton mass is within $10\,GeV$ of the Z mass peak are discarded.

4.5.4 $4l$ category

The category is identified by exactly 4 light leptons with null total charge, out of which the leading lepton $p_T > 25\,GeV$ and sub leading lepton $p_T > 15\,GeV$. The channel is inclusive in the number of τ_{had}. At least 2 jets of which one must be a b-jet must be selected in the event. Events that contain an opposite sign, same flavour, lepton couple with invariant mass within $10\,GeV$ of the Z mass peak are discarded, as well as those with invariant mass lower than $10\,GeV$, in order to suppress $t\bar{t}Z$ and resonant background. To reject $Z \to 4l$ and $t\bar{t}Z$ events, the four lepton invariant mass is required to be between 100 and $500\,GeV$. Selected candidate events are further categorized by the presence or absence of a same-flavour opposite-sign lepton pair. These are called Z-enriched and Z-depleted events, where the first can come from off-shell Z and $\gamma^* \to ll$

decays.

4.5.5 $1l2\tau$ category

The channel is defined by a single lepton with $p_T > 25\,GeV$ and 2 τ_{had} candidates with opposite sign charges. At least 3 reconstructed jets must be included in the event and one of them must be b-tagged. The signal region is mostly composed of $H \to \tau\tau$ events, allowing the partial reconstruction of the mass of the Higgs. The signal is identified with a cut $60 < m_{vis} < 120\,GeV$, since there is an energy loss due to the neutrinos produced in the τ decays. In this case, since there are multiple undetected objects, the missing E_T doesn't have enough information to reconstruct the whole event.

4.6 Background estimation

While object and event selections can identify the signal region accurately, this will never be pure, especially when the cross section is low compared to the background processes. Background estimation has, thus, a primary role in obtaining a more stringent limit measurement. We mainly focus on the $2lSS0\tau$ channel, providing just a quick overview of the other channels.
Most of the irreducible backgrounds, including $t\bar{t}V$ and diboson, are estimated using MC simulations and validated with data using dedicated control regions. Reducible backgrounds like W+jets and $t\bar{t}$, on the other hand, are mostly coming from processes that should replicate the signal only in case of non-prompt lepton production or electron charge mis-identification. In some categories these are treated using MC simulation, while in others data-driven techniques are used to better model the backgrounds.

4.6.1 $t\bar{t}V$ and tZ

The Feynman diagrams for the associated production of $t\bar{t}$ and massive vector bosons are shown in figure 4.4, displaying event topologies very similar to the $t\bar{t}H$ production.
The $t\bar{t}W$ process, of particular concern to the $2lSS$ categories, usually has lower jet multiplicity than the $t\bar{t}H$ signal and consequently most of its contribution is made of events

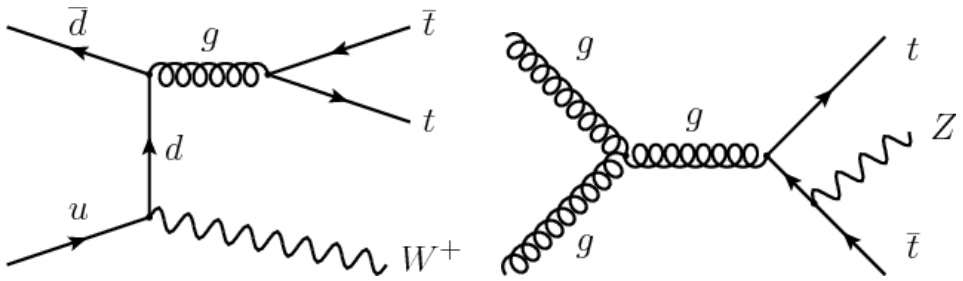

Figure 4.4: Feynman diagrams of the Leading Order $t\bar{t}W$ (left) and $t\bar{t}Z$ (right) production at LHC.

presenting additional high-energy jets. $t\bar{t}Z$, on the other hand, is the most significant contribution to the other channels. The Z boson has to decay leptonically to mimic the signal, resulting in events that can be greatly reduced by vetoing the Z invariant mass of the OS couples. The tZ is a small contribution to the background of every channel. For the $t\bar{t}Z$ background, a validation control region can be defined using the Z mass peak. This shows good agreement between MC and data within statistical uncertainties. For $t\bar{t}W$, a validation region, albeit with lower purity and statistic, is defined using the $2lSS0\tau$ selection, but requiring $N_{jet} = 2$ or 3 and $N_{bjet} > 1$. The comparison of the spectra as a function of the number of jets is shown in figure 4.5.

Systematic uncertainties for this background are a combination of cross-section and acceptance uncertainties, which are estimated comparing different MC simulations: Sherpa2.1.1 at LO, Sherpa+OpenLoops at NLO and Herwig++. These comparison are made to evaluate the impact of, respectively, parton shower matching effects, LO against NLO acceptance and p_T-ordered versus angular-ordered parton showers. Together these effects account for a 5 to 23% uncertainty, depending on the analysis channel and the background source into consideration. Systematic uncertainties due to PDF and the choice of QCD scale have an estimated impact of, respectively $0.8 - 4.8\%$ and $1.3 - 6.7\%$.

4.6.2 Prompt background with MC

Monte Carlo simulations are also used to evaluate backgrounds deriving from diboson processes associated with heavy flavour jets (or light jets with mis-identified flavour). In the $2lSS0\tau$ channel this has small impact, mainly coming from WZ+jet where the OS

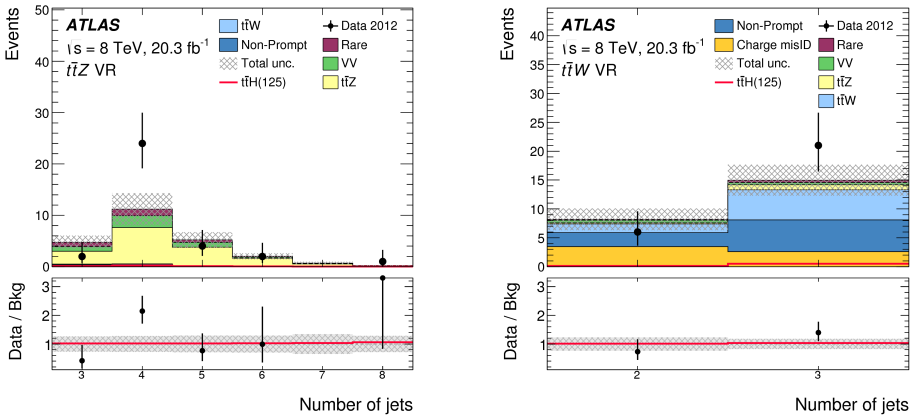

Figure 4.5: The spectrum of the number of jets expected and observed in the $t\bar{t}Z$ (left) and $t\bar{t}W$ (right) validation regions (VR). The hatched band represents the total uncertainty on the background prediction in each bin. The "non-prompt" backgrounds are those with a lepton arising from a hadron decay or from a photon conversion in detector material. Rare processes include tZ, $t\bar{t}WW$, triboson, $t\bar{t}t\bar{t}$, and tH production. The red line corresponds to the $t\bar{t}H$ signal predicted by the SM.

lepton is lost.
The most relevant process to the $3l$ channel is WZ+jets, that was compared to data in a dedicated validation region, requiring a Z boson and 0/1 b-jets. For the $0b$ region, the data is well modelled by MC, but the $WZ + b$ is constrained with a 100% uncertainty, giving an overall 50% uncertainty on the total WZ contribution to the $3l$ channel.

4.6.3 Charge mis-identification

The $2lSS$ channels can have contamination from opposite sign (OS) backgrounds if the sign of the lepton charge is mis-reconstructed, as shown in figure 4.6.
There are two main sources of electron charge mis-identification:

- Hard Bremsstrahlung producing trident electrons ($e^{\pm} \to e^{\pm}\gamma^{*} \to e^{\pm}e^{+}e^{-}$) whose EM cluster is identified with the wrong electron's track, leading to a mis-identification of the charge. This source represents the main contribution to the background. The fraction of trident electrons depends on the amount of material that the electrons

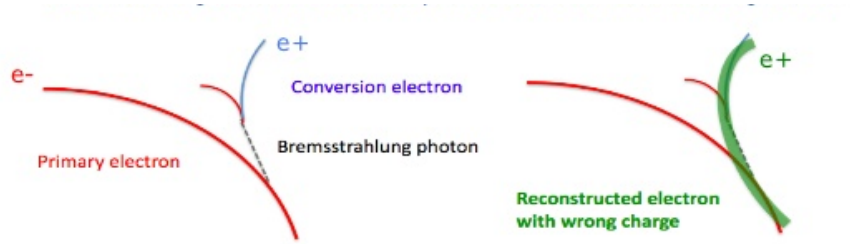

Figure 4.6: Electron charge mis-identified due to the production of a high-energy positron during matter interaction.

traverse. In the detector, the distribution of the material depends on $|\eta|$. Therefore, a strong dependence on $|\eta|$ is expected in the mis-identification rates. The probability of this happening for muons is negligible due to the lower energy loss into matter.

- A slightly curved track that induces a measurement error. This effect is important at high transverse momentum. Thus, a small dependence on electron p_T is also expected in the mis-identification rates. Thanks to the long arms of the muon trajectories in the Muon Chambers, muons are virtually unaffected.

The charge mis-ID rate is estimated using a maximum likelihood fit of $Z \to ee$ events of same and opposite charge and parametrized as a function of η and p_T, as shown in figure 4.7. High p_T regions are extrapolated from lower p_T ones using scaling functions extracted from MC simulations. This rate is applied to opposite sign control regions otherwise defined exactly as the signal and other CR's. The systematic uncertainty is dominated by the statistical uncertainty of the charge mis-ID, yielding a final uncertainty of $\sim 40\%$ in the signal region.

4.6.4 Non-prompt leptons

An important portion of the background for the several analysis categories comes from events where a light lepton is produced in hadron decays inside a jet, transforming a lepton event into a dileptonic one and a dileptonic event into a trileptonic one. This is relevant, respectively, for the $2lSS0\tau$ signal and the $3l$ and $2lSS1\tau$ categories. Since tight

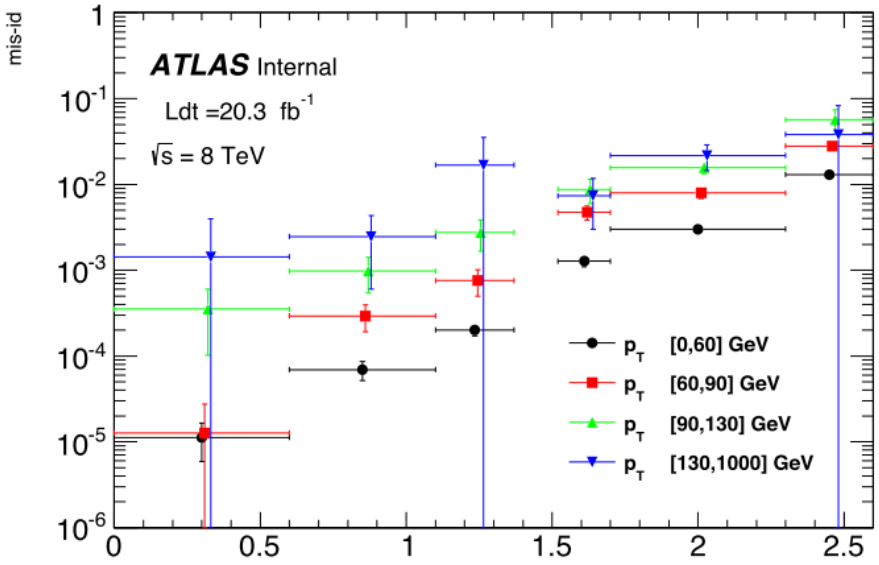

Figure 4.7: Electron charge mis-identification probability estimated using a likelihood fit through same sign and opposite sign lepton couples on the Z mass peak.

reconstruction and isolation requirements are applied to selected analysis objects, most of this kind of background is removed. In the signal region, these backgrounds are mostly composed by $t\bar{t}$ or single top events, but also W+jets contributes in a smaller portion. Estimates of these backgrounds are taken from data with slightly different methods used in each category, due to the particular event topologies and control region statistics. Other methods were studied and evaluated but ultimately discarded for the sake of simplicity. As a reference, leptons that pass the full object selection are denominated "tight", while "sideband" leptons have some of the selection cuts modified or inverted. "Sideband" control regions are defined by having one or more leptons that are sideband instead of tight or by different jet requirements.

2lSS0τ

Two side-band regions, enriched in $t\bar{t}$ non-prompt electrons, are used to produce yields that are afterwards extrapolated to the signal regions. Sideband electrons must have the standard identification and isolation requirements inverted, while sideband muons are identical to tight muons except for the transverse momentum, that is required to be

$6 < p_T < 10\,GeV$. Sideband regions have exactly one tight lepton and one sideband lepton, but are otherwise identical to the signal region. Transfer factors must be used to extrapolate sideband events into the signal region with two tight leptons. Two control regions are defined to extract the transfer factors shown in figure 4.8, identical to the sideband and signal region, but with the orthogonal requirement of having lower jet multiplicity: $1 \leq n_{jet} \leq 3$ for electrons and $2 \leq n_{jet} \leq 3$ for muons. Monte Carlo simulations are used to evaluate the prompt background in all sideband and control regions, subtracting these before calculating and applying the transfer factors, together with the electron charge mis-identification contribution. A veto on m_{ll} close to the Z mass peak is applied to the electrons in order to reduce the contribution from $Z \to ee$ events. A cross-check using a definition of sideband muon similar to the electron one yielded similar results, increasing the confidence in the method.

The systematic uncertainty on this method is estimated on $t\bar{t}$ MC events and by vary-

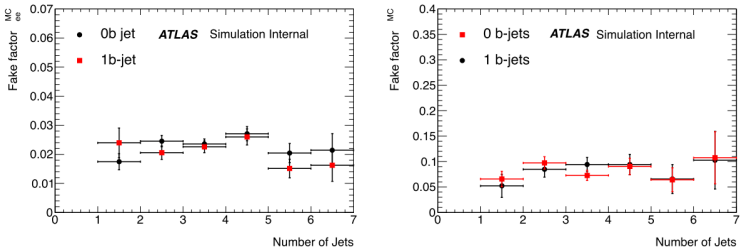

Figure 4.8: Transfer fake factors measured for ee (left) and $\mu\mu$ (right) events as a function of the number of jets in the event.

ing the definitions of sideband and control regions. Different parton shower and hadron decay models are used, as well as removing the requirement on a b-tag. Concerning electrons, also relaxing the η cut and increasing the p_T threshold were tested. Stability was evaluated in the range $25 - 30\%$, limited by simulation statistics. In data, the method is studied by altering the p_T cut of the b-jets, applying a requirement on missing transverse energy (E_T) and changing the N_{jet} definition of the transfer factor control region or using $10 - 15\,GeV$ to define the muon sideband region. Stability in this case was found to be 19% for electrons and 14% for muons. The total systematic uncertainty on this background source ranges between 32% and 52%.

This method cannot provide a fully data-driven estimation as a function of other kinematic variables (such as the lepton p_T), due to the low statistic in some of the regions used to extract the fake factors. In chapter 5 we use a different method, called *matrix method* to estimate the fake background, showing its potential in differential analyses.

$3l$

In this region the definition of sideband leptons consists in reversing the isolation cut for both flavours and, in addition, for electrons, reverting the tight electron identification requirement, passing the loose likelihood definition instead. The sideband region is defined by the same cuts used for the signal region, but with one of the leptons being sideband instead of tight. Transfer factors are taken from MC simulation. These sideband events are mainly composed of two opposite sign prompt leptons and a non-prompt lepton, that forms a same sign couple with one of the prompt leptons. Due to this the method is applied only to the two same sign leptons. Even though the transfer factors are from simulation, they are validated on data in the region $2 \leq n_{jet} \leq 3$, showing good agreement. Comparing data and simulation of the extrapolated variables, a systematic uncertainty of 20% is estimated both for electrons and muons. Additional uncertainties are given by the propagation of the statistical uncertainties on control regions and simulation.

$2lSS1\tau$

A similar technique to that of the previous categories is used in this channel. The presence of a τ_{had} is similar between control and signal region, so no impact on the sideband and control region definition. To define the sideband region, the E_T cut is inverted and the p_T requirement is relaxed. Additionally, in the electron case the identification criterion is relaxed. Transfer factors were extrapolated in the $2 \leq n_{jet} \leq 3$ control region, while the sideband region is defined in the same way as the signal, but with one of the leptons being sideband instead of tight. Validation is done using $t\bar{t}$ simulations and its statistical precision dominates (27%) the systematic uncertainty. Overall uncertainty is, anyway, mostly due to the low statistic on the high jet multiplicity control region.

4l

The contribution of the non-prompt background to the $4l$ signal is estimated at $\leq 10^{-3}$ total events in the Z-enriched region and $\leq 10^{-4}$ in the Z-depleted region. These represent $\sim 2\%$ of the total background.

4.6.5 τ misidentification

The evaluation of the τ_{had} fake yield is necessary only for the $1l2\tau$ category, where it reaches a sizeable contribution. The estimation is performed on $t\bar{t}$ simulation, but this is cross-checked with data-driven techniques. Since the τ_{had} of the events are opposite sign, one of them will be of the same sign as the light lepton and the other of opposite sign. The SS candidate is usually a fake while the light lepton is prompt and the OS candidate is often real. Sideband τs are defined as a candidate passing a loose identification BDT selection but not the tight one. Three control regions are defined, depending on which (or if both) τ candidate is sideband. The two regions with sideband OS candidates are used to obtain the transfer factor for the SS candidate. This is then applied to the region with tight OS and sideband SS to obtain the estimation in the signal region. Transfer factors are parametrized as a function of several kinematic and topological properties of the event. Due to the statistical limitations of the method, it is used only as a cross-check for the $t\bar{t}$ simulation and the comparison gives a 36% systematic uncertainty on the prediction in the signal region.

4.7 Other uncertainties

There are other sources of systematic uncertainties that do not derive directly from the analysis procedure. One of them is the uncertainty on the integrated luminosity, estimated at 2.8%, derived from a calibration in the luminosity scale during data-taking [90].
Clean resonances, such as J/ψ and Z, are used to determine the lepton reconstruction and identification uncertainties. The main systematic uncertainties on jets come from the jet energy scale: the in-situ calibration, the different response between quark and gluon

Category	q mis-id	Non-prompt	$t\bar{t}W$	$t\bar{t}Z$	Diboson	Expected bkg.	$t\bar{t}H$ ($\mu = 1$)	Observed
$ee + \geq 5j$	1.1 ± 0.5	2.3 ± 1.2	1.4 ± 0.4	0.98 ± 0.26	0.47 ± 0.29	6.5 ± 1.8	0.73 ± 0.14	10
$e\mu + \geq 5j$	0.85 ± 0.35	6.7 ± 2.4	4.8 ± 1.2	2.1 ± 0.5	0.38 ± 0.30	15 ± 3	2.13 ± 0.41	22
$\mu\mu + \geq 5j$	–	2.9 ± 1.4	3.8 ± 0.9	0.95 ± 0.25	0.69 ± 0.39	8.6 ± 2.2	1.41 ± 0.28	11
$ee + 4j$	1.8 ± 0.7	3.4 ± 1.7	2.0 ± 0.4	0.75 ± 0.20	0.74 ± 0.42	9.1 ± 2.1	0.44 ± 0.06	9
$e\mu + 4j$	1.4 ± 0.6	12 ± 4	6.2 ± 1.0	1.5 ± 0.3	1.9 ± 1.0	24 ± 5	1.16 ± 0.14	26
$\mu\mu + 4j$	–	6.3 ± 2.6	4.7 ± 0.9	0.80 ± 0.22	0.53 ± 0.30	12.7 ± 2.9	0.74 ± 0.10	20
3ℓ	–	3.2 ± 0.7	2.3 ± 0.7	3.9 ± 0.8	0.86 ± 0.55	11.4 ± 2.3	2.34 ± 0.35	18
$2\ell 1\tau_{\mathrm{had}}$	–	$0.4^{+0.6}_{-0.4}$	0.38 ± 0.12	0.37 ± 0.08	0.12 ± 0.11	1.4 ± 0.6	0.47 ± 0.08	1
$1\ell 2\tau_{\mathrm{had}}$	–	15 ± 5	0.17 ± 0.06	0.37 ± 0.09	0.41 ± 0.42	16 ± 5	0.68 ± 0.13	10
4ℓ Z-enr.	–	$\lesssim 10^{-3}$	$\lesssim 3 \times 10^{-3}$	0.43 ± 0.12	0.05 ± 0.02	0.55 ± 0.15	0.17 ± 0.02	1
4ℓ Z-dep.	–	$\lesssim 10^{-4}$	$\lesssim 10^{-3}$	0.002 ± 0.002	$\lesssim 2 \times 10^{-5}$	0.007 ± 0.005	0.025 ± 0.003	0

Table 4.4: Expected and observed yields in each channel. Uncertainties shown are the sum in quadrature of systematic uncertainties and Monte Carlo simulation statistical uncertainties. "Non-prompt" includes the misidentified τ_{had} background to the $1l2\tau$ category. Rare processes (tZ, $t\bar{t}WW$, triboson production, $t\bar{t}t\bar{t}$, tH) are not shown as a separate column but are included in the total expected background estimate.

jets and the pile-up subtraction. Since the requirement on N_{bjet} is usually 1, the impact of b-tagging efficiency is reduced for signal and the main backgrounds. The impact of b-tagging on signal strength $\mu = \sigma_{obs}/\sigma_{SM}$ produces an uncertainty $\Delta\mu = ^{+0.08}_{-0.06}$.
The uncertainties on $t\bar{t}H$ cross section, as well as PDF uncertainty, QCD scale choice and parton shower algorithm effect on acceptance in each analysis category are considered. These latter result in variations of $0.3 - 1.4\%$ for PDF, $0.1 - 2.7\%$ for scale choice and $1.5 - 13\%$ for parton shower algorithm. Uncertainties from MC simulation statistics are mostly negligible, except for the diboson case where they can reach 50% of the total uncertainties.
The total uncertainties are shown in table 4.4.

4.8 Results

In this section we compare the observed data yields and background estimations already introduced in table 4.4 to get a measurement of the deviation of the data from the Standard Model, using the variable $\mu = \sigma/\sigma_{SM}$. Figure 4.9 shows the distribution of the yields and the expected backgrounds as a function of the number of jets in the event.

The signal strength μ is calculated for every signal channel using a maximum likelihood

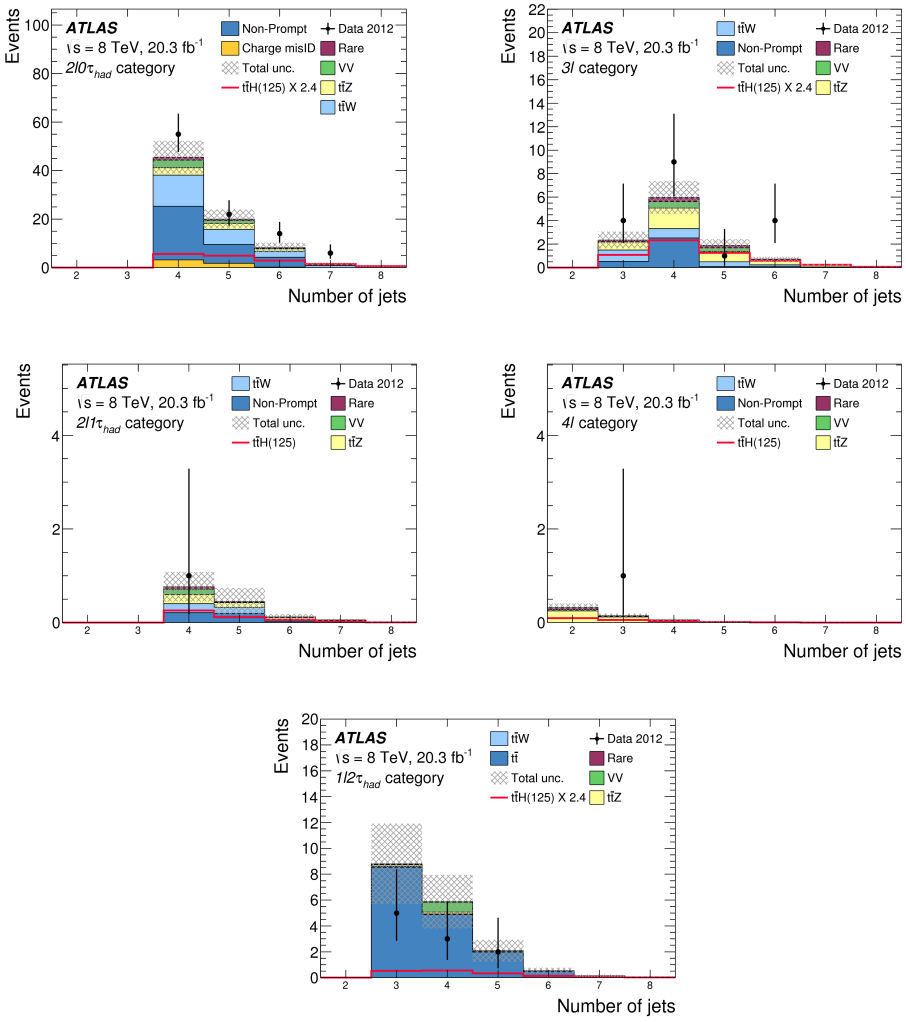

Figure 4.9: The spectrum of the number of jets expected and observed in each signal region. For display purposes the six $2l0\tau$ categories ($ee/e\mu/\mu\mu$ and $N_{jets} = 4/ \geq 5$) are combined into one plot, as are the two $4l$ categories (Z-enriched and Z-depleted). The hatched bands show the total uncertainty on the background prediction in each bin. The non-prompt and charge mis-id background spectra are taken from simulation of $t\bar{t}$, single top, $Z \rightarrow ll$+jets and other small backgrounds, with normalization as described in the text (in particular the $N_{jets} = 4/ \geq 5$ regions of the $2l0\tau$ plot have the ratio given by the data-driven prediction). The red line shows the $t\bar{t}H$ signal from the Standard Model. For visibility, the $t\bar{t}H$ signal is multiplied by a factor of 2.4 in the $2l0\tau$, $3l$, and $1l2\tau$ plots.

fit, where these are considered as independent poissonian terms. The profile likelihood approach is used, where the systematic uncertainties are treated as nuisance parameters with their own uncertainties that can be constrained by the fit [91]. As a reference, we consider the hypothesis $\mu = 1$ the case of the Standard Model Higgs production ($m_H = 125\,GeV$). Systematic uncertainties are allowed to float as nuisance parameters of the fit, assuming their best fit values. The only constraints are imposed on the lepton transfer factors and normalization region yields for $2l0\tau$ category and the fake τ background for the $1l2\tau$ channel. The first ones are affected by large statistical uncertainties and so the results from the signal region are expected to constrain them. The latter is affected by a large initial uncertainty that the fit can constrain.
The fit produces the results shown in figure 4.10, whereas table 4.5 displays them together with the most significant uncertainties; these are mostly statistical, with the exception of the combined $2l1\tau$ channel. All results are compatible with the Standard Model and with the other experimental results obtained in the past [92]. Combining all results, we obtain a value $\mu = 2.1^{+1.4}_{-1.2}$, while the expected SM result, considering systematic and statistical uncertainties, would have been $1.0^{+1.2}_{-1.1}$.

The p-value observed for the $\mu = 0$ hypothesis is 0.0037, against an expected 0.18, corresponding respectively to deviations of 1.8σ and 0.9σ from the SM. The observed p-value of the SM hypothesis is 0.18, corresponding to a 0.9σ deviation. Using the likelihood function [91] we obtained a 95% confidence level upper limit on μ, shown in table 4.5, for every channel, leading to a combined value of $\mu < 4.7$, where the expected value was $\mu < 2.4$.

In this analysis the $tHqb$ and tHW processes have been considered together with the $t\bar{t}H$ signal, since no explicit subtraction of their contribution from the signal region has been performed. If we can consider the $tHqb$ and tHW processes as background, the μ value is shifted by $\Delta\mu = -0.04$. $t\bar{t}V$ production in the analysis is considered a background and as such its cross-section is set to the theoretical prediction, but the experimental cross-sections have still high uncertainties. In the case of a variation from the SM values, $\mu(t\bar{t}H)$ varies as a function of the $t\bar{t}V$ cross sections: $\mu(t\bar{t}H) = 2.1 - 1.4(\sigma(t\bar{t}W)/232 - 1) - 1.3(\sigma(t\bar{t}Z)/206 - 1)$, values in fb.

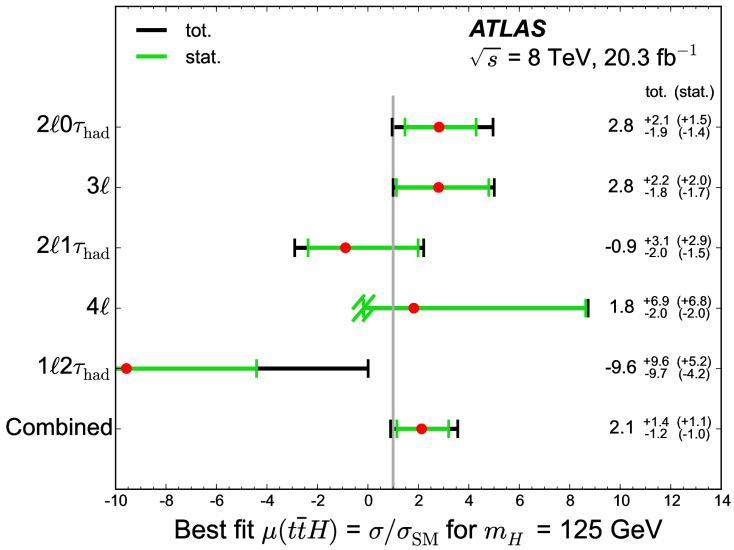

Figure 4.10: Best fit values of the signal strength parameter $\mu = \sigma_{t\bar{t}H,obs}/\sigma_{t\bar{t}H,SM}$. For the 4l Z-depleted category, $\mu < -0.17$ results in a negative expected total yield and so the lower uncertainty is truncated at this point.

Source	$\Delta\mu$	
$2\ell 0\tau_{\rm had}$ non-prompt muon transfer factor	$+0.38$	-0.35
$t\bar{t}W$ acceptance	$+0.26$	-0.21
$t\bar{t}H$ inclusive cross section	$+0.28$	-0.15
Jet energy scale	$+0.24$	-0.18
$2\ell 0\tau_{\rm had}$ non-prompt electron transfer factor	$+0.26$	-0.16
$t\bar{t}H$ acceptance	$+0.22$	-0.15
$t\bar{t}Z$ inclusive cross section	$+0.19$	-0.17
$t\bar{t}W$ inclusive cross section	$+0.18$	-0.15
Muon isolation efficiency	$+0.19$	-0.14
Luminosity	$+0.18$	-0.14

Table 4.5: Leading sources of systematic uncertainty and their impact on the measured value of μ

Conclusions

The analysis was performed on 20.3 fb^{-1} of data gathered by the ATLAS experiment at the LHC energy of $8\,TeV$. The resulting $\mu(t\bar{t}H) = 2.1^{+1.4}_{-1.2}$ is compatible with the Standard Model, imposing the 95% CL limit $\mu < 4.7$. Due to the high uncertainty, this result cannot be considered as the discovery of a discrepancy in the $t\bar{t}H$ standard model production, since a 5-σ level of certainty is required for this.
In the coming chapters, a different method for the fake background estimation is shown and applied to Run I and to the first data gathered by ATLAS in 2015. This *matrix method* provides differential background estimation, which is an important addition to the Run I results and will become essential for the high expected statistics of 2016.

Chapter 5

The Matrix Method background estimation

The *matrix method* is a data driven background estimation. It is used to measure the contamination in a selected region of mis-identified reconstructed objects or the rate of events produced by background. In the analysis described here we apply it to the case of light leptons (electrons and muons) produced by jets (in particular jets produced by heavy quarks). The method uses two selections on the physics reconstructed object: the tight one which is the one used for the selection of the Signal Region (SR) and a looser one that includes the tight selection. The method is used to estimate background coming from fake leptons as a function of any variable [93] [94], making it ideal for differential analyses and multi-variate analysis.

5.1 The theoretical framework

The matrix method exploits differences in identification between real and fake leptons (see chapter 4):

- Real leptons are the ones coming from W, Z and τ leptonic decays, where these are coming directly from t or H decay; they are usually isolated, well reconstructed and come from the primary vertex;

- Fake leptons are produced in meson decays in jets, so they are mostly non-isolated and may come from a secondary vertex; for this reason they are sometimes referred to as "non-prompt".

The method is based on selecting two categories of events using loose and tight lepton selection requirements. The tight lepton selection is by definition the standard lepton selection used in the analysis (well identified leptons coming from the primary vertex), while the loose one is obtained reducing some of the lepton identification and isolation requirements. This way all the leptons passing the tight selection ("tight leptons") are also passing the loose lepton selection (they are "loose leptons" as well). Based on these loose and tight lepton selections, two data samples are defined, differing only in the lepton identification criteria (loose or tight), while keeping the same kinematic selections. The tight sample contains mostly events with real leptons, while the loose one is enriched in events with fake leptons. The number of events contained in each sample is, thus, a sum of events containing real and fake leptons.
In the single-lepton case this means:

$$N^{loose} = N^{loose}_{real} + N^{loose}_{fake} \tag{5.1}$$

$$N^{tight} = N^{tight}_{real} + N^{tight}_{fake} \tag{5.2}$$

where $N^{loose}_{real(fake)}$ is the number of real (fake) events with a lepton passing the loose criteria and $N^{tight}_{real(fake)}$ is the number of real (fake) events passing the tight selection. The quantity that we want to measure is N^{tight}_{fake}, which is the fake background that still passes the tight selection. We can now define the fake and real efficiencies as $\epsilon_{real} = N^{tight}_{real}/N^{loose}_{real}$ and $\epsilon_{fake} = N^{tight}_{fake}/N^{loose}_{fake}$. This way we can express the number of tight leptons as $N^{tight}_{real} = \epsilon_{real} \times N^{loose}_{real}$ and $N^{tight}_{fake} = \epsilon_{fake} \times N^{loose}_{fake}$. If the efficiencies are known, this equation system can be solved. In the case of a single lepton selection, the solution is straightforward:

$$N^{tight}_{fake} = \frac{\epsilon_{fake}}{\epsilon_{real} - \epsilon_{fake}}(\epsilon_{real} N^{loose} - N^{tight}) \tag{5.3}$$

Note that for the method to work properly, a clear separation between ϵ_{real} and ϵ_{fake} is required, with the former that needs to be close to 1; otherwise, we incur in very large or extremely small weights, resulting in an inaccurate estimation. ϵ_{real} and ϵ_{fake} are usually

dependent on the particle kinematic properties or some global event topology property var, such as p_T, η, N_{jet} or $\Delta R_{l-jet} = \sqrt{\Delta\eta^2 + \Delta\phi^2}$; since their values are calculated in different regions with respect to the signal one (like the Z mass peak for ϵ_real), to use them properly we need to parametrize them as a function of these variables. This is the reason why, instead of a global counting method, each event is weighted with a weight that depends on its kinematic properties:

$$w_i = \frac{\epsilon(var)_{fake}}{\epsilon(var)_{real} - \epsilon(var)_{fake}}(\epsilon(var)_{real} isLoose(i) - isTight(i)), \tag{5.4}$$

where *isLoose(i)* and *isTight(i)* are 1 if the lepton passes respectively the loose and tight selections, 0 otherwise. This way the number of fake leptons passing the tight selection can be estimated as $N_{fake}^{tight} = \sum_{data} w_i$.

The principles of the method can be applied to cases with two or more leptons, too. We use it to estimate the non-prompt background of the 2lSS0tau channel, so we have to apply it to the two-leptons case. To generalize this case we define l as a lepton that passes the loose selection requirements, t a lepton that passes the tight selection, $\bar{t}$ a lepton that passes the loose but not the tight selection, r a real lepton and f a fake lepton. The real and fake efficiencies are redefined as $r_i = \epsilon(i)_{real}$ and $f_i = \epsilon(i)_{fake}$. This way we get a vector of events based on the four resulting event categories that can be derived using a matrix M from the combination of real and fake leptons that pass the loose selection (ll pairs):

$$\begin{pmatrix} N_{tt} \\ N_{t\bar{t}} \\ N_{\bar{t}t} \\ N_{\bar{t}\bar{t}} \end{pmatrix} = M \begin{pmatrix} N_{rr}^{ll} \\ N_{rf}^{ll} \\ N_{fr}^{ll} \\ N_{ff}^{ll} \end{pmatrix}, \tag{5.5}$$

where N indicates the number of pairs made with leptons passing the loose selection and passing (t) and/or failing ($\bar{t}$) the tight selection; their number is connected with the real (r) and fake (f) pairs passing the loose selection (ll) through the matrix M, defined as:

$$M = \begin{pmatrix} r_1 r_2 & r_1 f_2 & f_1 r_2 & f_1 f_2 \\ r_1(1-r_2) & r_1(1-f_2) & f_1(1-r_2) & f_1(1-f_2) \\ (1-r_1)r_2 & (1-r_1)f_2 & (1-f_1)r_2 & (1-f_1)f_2 \\ (1-r_1)(1-r_2) & (1-r_1)(1-f_2) & (1-f_1)(1-r_2) & (1-f_1)(1-f_2) \end{pmatrix} \tag{5.6}$$

The matrix is then inverted to solve the linear system and find the real and fake contributions to the ll pairs.

$$M^{-1} = \frac{1}{(r_1 - f_1)(r_2 - f_2)} \begin{pmatrix} (1-f_1)(1-f_2) & (f_1-1)f_2 & f_1(f_2-1) & f_1 f_2 \\ (f_1-1)(1-r_2) & (1-f_1)r_2 & f_1(1-r_2) & -f_1 r_2 \\ (r_1-1)(1-f_2) & (1-r_1)f_2 & r_1(1-f_2) & -r_1 f_2 \\ (1-r_1)(1-r_2) & (r_1-1)r_2 & r_1(r_2-1) & r_1 r_2 \end{pmatrix} \quad (5.7)$$

Now we can use the efficiencies again to obtain the number of fake dilepton events that enter the tight-tight (N_f^{tt}) signal selection:

$$\begin{aligned} N_f^{tt} = N_{rf}^{tt} + N_{fr}^{tt} + N_{ff}^{tt} = r_1 f_2 N_{rf}^{ll} + r_2 f_1 N_{fr}^{ll} + f_1 f_2 N_{ff}^{ll} = \\ \alpha r_1 f_2 [(f_1-1)(1-r_2)N_{tt} + (1-f_1)r_2 N_{t\bar{t}} + f_1(1-r_2)N_{\bar{t}t} - f_1 r_2 N_{\bar{t}\bar{t}}] \\ + \alpha f_1 r_2 [(r_1-1)(1-f_2)N_{tt} + (1-r_1)f_2 N t\bar{t} + r_1(1-f_2)N_{\bar{t}t} - r_1 f_2 N_{\bar{t}\bar{t}}] \\ + \alpha f_1 f_2 [(1-r_1)(1-r_2)N_{tt} + (r_1-1)r_2 N t\bar{t} + r_1(r_2-1)N_{\bar{t}t} + r_1 r_2 N_{\bar{t}\bar{t}}] \end{aligned} \quad (5.8)$$

where we have defined $\alpha = 1/(r_1 - f_1)(r_2 - f_2)$. The above equation can be used on an event-by-event basis to determine the weight w_f^{tt} that indicates the contribution of that event to the fake dilepton signal. Since f_i and r_i are measured in regions with a different topology from the signal one, if there is a significant dependence from topological or kinematic variables, it is necessary to parametrize the efficiencies as a function of these variables, using $f_i \to f(var_i)$ and $r_i \to r(var_i)$.

5.1.1 Analysis-specific considerations

In this analysis the tight lepton definition is exactly the one presented in chapter 4, as required by the matrix method. Loose leptons are defined by removing or loosening some selection cuts, while maintaining all the others identical, remaining consistent with the tight selection. For both lepton flavours this is accomplished by removing the isolation cut, although tests were made that also removed the $tight/tight_{LH}$ identification requirement from the loose definition. Overlap removal is treated differently in the case of loose objects: not to alter the tight event topology with the introduction of loose

leptons, any object is removed only if within the ΔR ($= \sqrt{\Delta\eta^2 + \Delta\phi^2}$) cone of a tight object. For example, a jet within $\Delta R = 0.3$ of a tight lepton would be removed, while it is kept if the lepton is not tight.
What was presented so far is the canonical framework of the matrix method for inclusive single lepton and dilepton events. In our case the signal region is defined by exactly two tight leptons, but there is no restriction on the number of loose (non-tight) leptons. This creates a difficulty in events where there are three loose leptons out of which at most 2 pass the tight selection. The exact solution to this issue would be summing to perform at the same time the background estimation for all the cathegories of the analysis (2lepton, 3-letpon etc) spoiling the different SR definitions. On the contrary we have adopted two alternative approaches, one that underestimates and the other that overestimates the background measurement:

- the matrix method weight is calculated only using the two leading leptons passing the loose cuts; any other lepton is ignored for weight calculation;
- summing all dilepton contributions; this is a slight overestimation, since it counts a part of the background that should contribute to the 3l channel, instead.

Very small differences were produced between the use of these two methods, under 10% in the regions with the largest differences (see section 5.3), and both were compatible with data in the Control Region, so the best match with the control region result (summing all contributions) is used in the final estimation.

5.2 Efficiency measurement

In this thesis the main efficiency parametrizations used are p_T, trigger matching and, for fakes, $\Delta R(\mu - b\text{-jet})$. Other parametrizations were also tested, standalone or in 2D with the p_T of the lepton. Other quantities tested or taken into consideration are $|\eta|$ of the lepton and N_{jet}. Combined with p_T these parametrizations show a negligible difference while introducing additional systematic uncertainties, as is displayed in detail in this section.

The *real* and *fake regions* where we evaluate the real efficiencies and fake rejections must have high real/fake purities to ensure a correct data-driven estimation. To further improve the accuracy in the ϵ_f determination, that has a lower purity, the prompt background estimated using MC simulations is subtracted.
With the exception of some tests, all efficiencies are differentiated on the basis of the lepton trigger matching: leptons that do not match with any trigger ("back"), leptons that match isolated triggers with low p_T thresholds ("medium") and leptons that pass high-p_T, non-isolated triggers ("high"). This is necessary because the main analysis triggers are either isolated or have a high-p_T threshold. The former reducing the difference between loose and tight leptons and the latter reducing the kinematic range of the MM.

5.2.1 Real efficiencies

The *real region* has to be as pure as possible. For this region, the Z boson signal is chosen due to its clear signal and high cross-section; it is defined by having two opposite sign (OS) leptons of the same flavour, with the baseline $p_T > 10\,GeV$ and the standard cuts($\eta < 2.4$ and excluding $1.37 < \eta < 1.52(e)$, $\left|\frac{d_0}{\sigma(d_0)}\right| < 3(\mu)/4(e)$ and $z0\sin\theta < 1\,mm$). The invariant mass of the dilepton couple must be within $83.7 < M_{ll} < 98.7\,GeV$, to exploit the purity of the Z boson mass peak. A tag-and-probe method is used to measure the efficiency: a high-p_T, isolated lepton is tagged and the second lepton is used as probe. If the lepton passes the loose cuts, it goes into a denominator histogram, while probes that pass both loose and tight cuts go into the numerator histograms. Figure 5.1 shows the real efficiencies as a function of p_T, η and N_{jet} for muons and electrons, differentiated on the basis of the lepton trigger matching, obtained by dividing the numerator histogram by the denominator histogram; this means that the value of every numerator bin is divided by the value of the corresponding bin in the denominator histogram.

The dependence on the number of jets is weak and within statistical uncertainties (except for backup muons), thus allowing the extrapolation to the higher N_{jet} signal regions without parametrizing for it. The dependence on η is rather weak, as well, so it is used in combination with p_T only to test the impact it has on the signal.

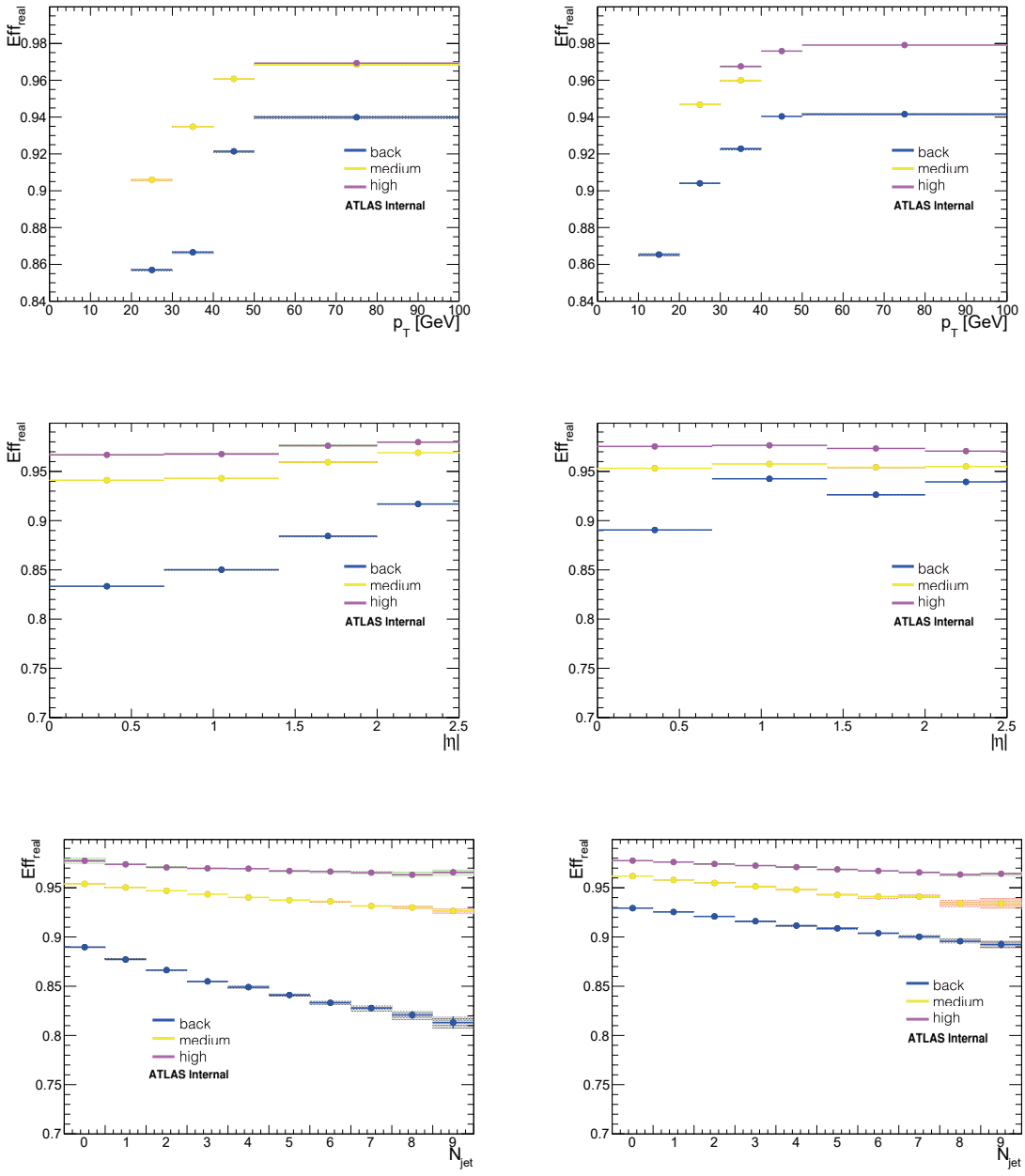

Figure 5.1: Real efficiency distributions as a function of p_T, η and N_{jet} for electrons (left) and muons(right), differentiated on the basis of the lepton trigger matching, measured using a tag-and-probe method on the Z mass peak.

5.2.2 Fake efficiencies

Fake efficiencies of non-prompt leptons are estimated in dedicated control regions orthogonal to the signal region, called $fake\,regions$. Regions enriched with fake leptons must be identified, reverting one or more signal cuts. During the analysis procedure, several different variations of the fake region definitions were tested, with the three main strategies being:

- a region with $N_{jet} \geq 2$, $N_{bjet} \geq 1$ and requiring exactly one lepton (loose or tight) passing the same selection as in the 2lSS channel except isolation and $\left|\frac{d_0}{\sigma(d_0)}\right| \leq 4$; orthogonality is ensured by asking for a single lepton and inverting this last cut, requiring $\left|\frac{d_0}{\sigma(d_0)}\right| \geq 5$, generically enriching the region with fakes coming from semileptonic b decays;

- the same $N_{jet} \geq 2$ and $N_{bjet} \geq 1$, with exactly one lepton, region is defined, but in this case the event must have the missing transverse energy $MET < 20\,GeV$, the transverse mass $M_T < 20\,GeV$ and their sum $MET + M_T < 20\,GeV$ in order to suppress the prompt W, $t\bar{t}$ and W+jets events;

- for both leptons the control region with $1 \leq N_{jet} \leq 3$ can also be used for ϵ_f measurement and is used in this thesis as a cross-check; it consists in selecting events with an isolated lepton and evaluating the efficiencies on the second one, provided it is of the same sign; in this way we select $t\bar{t}$ events and, while OS events are mostly from dileptonic decays, SS events mostly come from semileptonic events with a second fake lepton.

Since the first two regions require exactly one lepton, this has to be the one that triggered the event. Due to the fact that we need to know the fake efficiencies of both leptons for the matrix method to work, it is necessary to include events acquired using low momentum and non-isolated triggers [1]. Every event must pass a certain trigger to be accepted, depending on the lepton p_T threshold, as shown in table 5.1.

The leptons selected in these regions, after the subtraction of the prompt lepton contri-

[1] To lower the acquisition rate, these triggers are *prescaled*, which means that only a fraction of the triggering events are actually acquired; the data is then corrected for this fraction.

p_T range (GeV)	e	μ
$20-25$	EF_e15vh_medium1	EF_mu15
$25-30$	EF_e22vh_loose1	EF_mu15
>30	EF_e24vh_medium1	EF_mu24_tight

Table 5.1: Triggers used for fake efficiency estimation. EF refers to them being compute at the Event Filter level, the number represents the p_T threshold and the rest indicates reconstruction and identification parameters.

butions, are all considered fake. The subtraction of this contribution is done using Monte Carlo simulations of the samples described in the previous chapter and summarized in table 4.1. In these control regions, the rest of the selection is identical to the Signal Region one, to keep the measurements as consistent as possible. To subtract the prompt contribution through the simulations, we require that the leptons we subtract come only from Z, W and $\tau \to l\nu\nu$ decays, matching them with the generator truth. Matching is accomplished using a ΔR reconstructed-truth discrimination; the lepton parent list of the truth particle is studied to identify vector bosons and τ decays. Leptons coming from jets produced by boson and tau hadronic decays are excluded from this selection, since they contribute to the non-prompt lepton pool.
The fake efficiency is then computed as:

$$\epsilon_f = \frac{N_t - B_{t(WZ\tau)}}{N_l - B_{l(WZ\tau)}} \tag{5.9}$$

where $N_{t(l)}$ is the number of tight(loose) leptons and $B_{t(l)(WZ\tau)}$ is the number of tight (loose) background leptons truth-matched with a W, Z or τ decay and weighted for the sample luminosity and appropriate MC weights. The subtraction is mostly relevant in the electron channel, where the contamination is higher, as shown in figure 5.2.

The $t\bar{t}$ MC all-hadronic sample is used for the first estimation through the Monte Carlo truth matching [2]. The ϵ_f distributions obtained in this way are displayed in figure 5.3 and are used in the next section to cross check the MM method on a MC sample.

In data the events were categorized not only on the basis of the trigger matched by the lepton but also on the distance in ΔR between the lepton and the closest b-jet,

[2]the information on the generation and development of each particle before the reconstruction phase

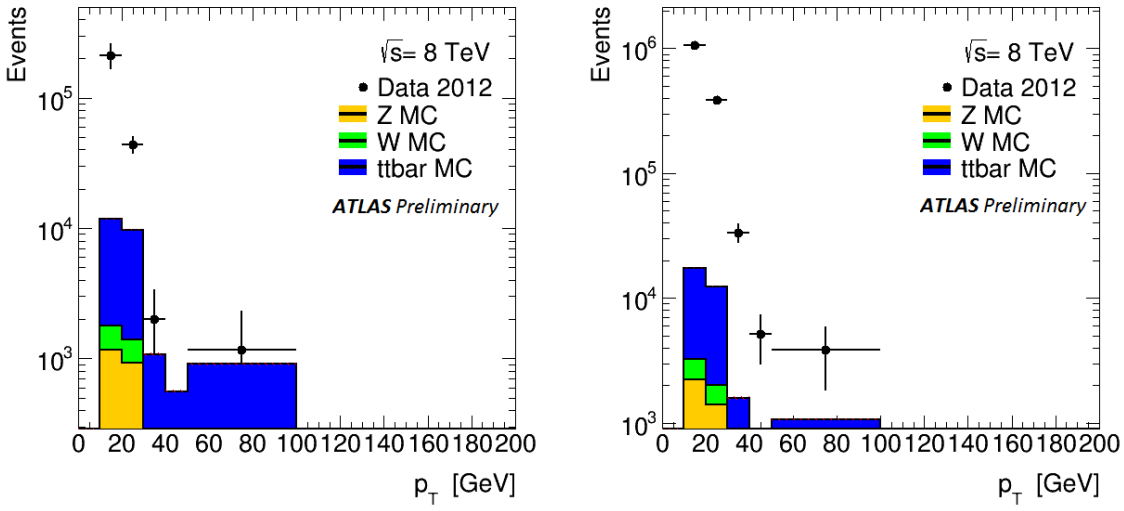

Figure 5.2: The fake efficiency estimation histograms in the electron channel, with the main single-lepton prompt backgrounds: $t\bar{t}$, W+jets and Z. The numerator histogram is on the left, the denominator is on the right.

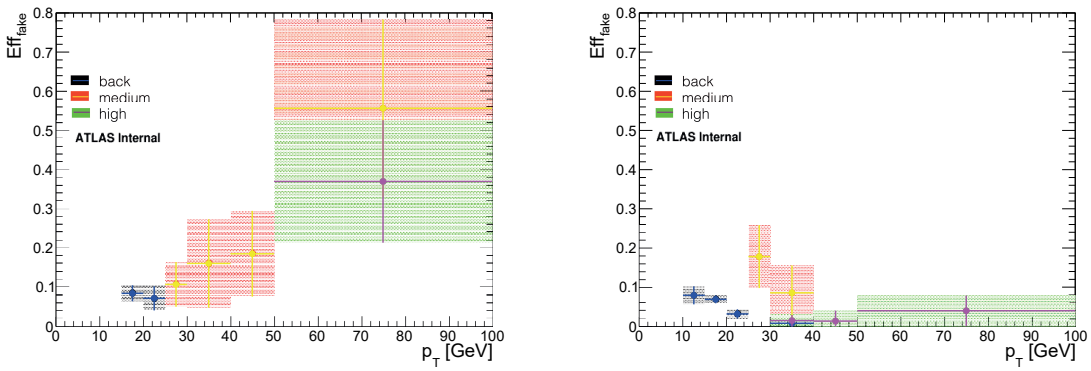

Figure 5.3: The fake efficiencies obtained on the $t\bar{t}$ all-hadronic sample, which are used later to estimate the non-prompt contribution in the non-all-hadronic sample. Electrons are displayed on the left and muons on the right.

because ϵ_f shows a dependence from these variables. Figure 5.4 shows the *standard* fake efficiencies for both muons and electrons as a function of p_T for the six categories. It is important to notice that the three trigger regions, are mostly relevant within the three respective p_T ranges (5.1).

The dependence from other kinematic and topological variables is studied in figure 5.5,

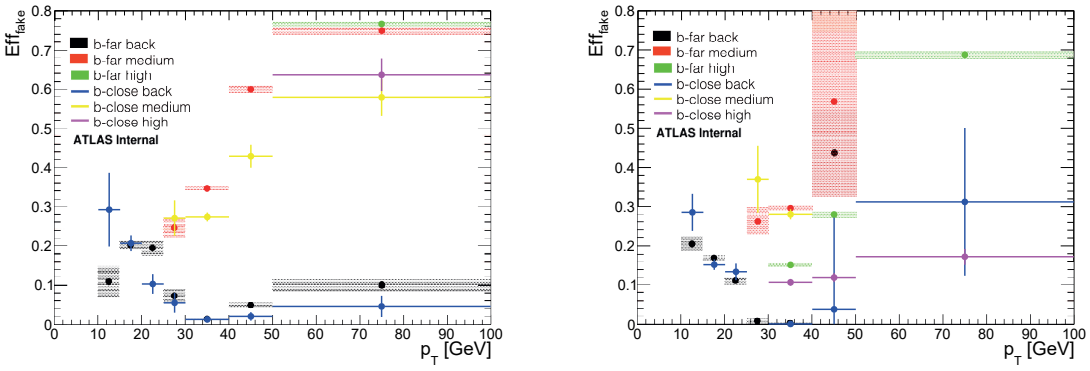

Figure 5.4: Lepton fake efficiencies determined in data using the prescaled triggers to include low-p_T, non isolated leptons. The distributions are displayed as a function of p_T for different categories of trigger matching and ΔR between b-jet and lepton. Electrons are displayed on the left and muons on the right.

revealing that the dependencies from these other variables is negligible within uncertainties. This allows us to use only the p_T, trigger and $\Delta R(l - b_{jet})$ parametrization.

At this point a comparison between the fake estimation methods is necessary to evaluate their compatibility and select one. Figure 5.6 shows the ϵ_f distributions for electrons and muons as a function of p_T calculated with the $\left|\frac{d_0}{\sigma(d_0)}\right| \geq 5$ method and the $2lSS$, low-N_{jet} control region. Due to low statistics, this last method has no discrimination on the basis of the ΔR between lepton and b-jet. The calculation using the $2lSS$, low-N_{jet} fake region produces results compatible with the *standard* FR definition, especially in the $\Delta R < 1.2$ region, which has the highest statistic. As a consequence of the lower overall statistic, this region is kept as a cross-check for the *standard* one. The distributions measured in the $\left|\frac{d_0}{\sigma(d_0)}\right| \geq 5$ fake region, instead, displays significantly lower result,

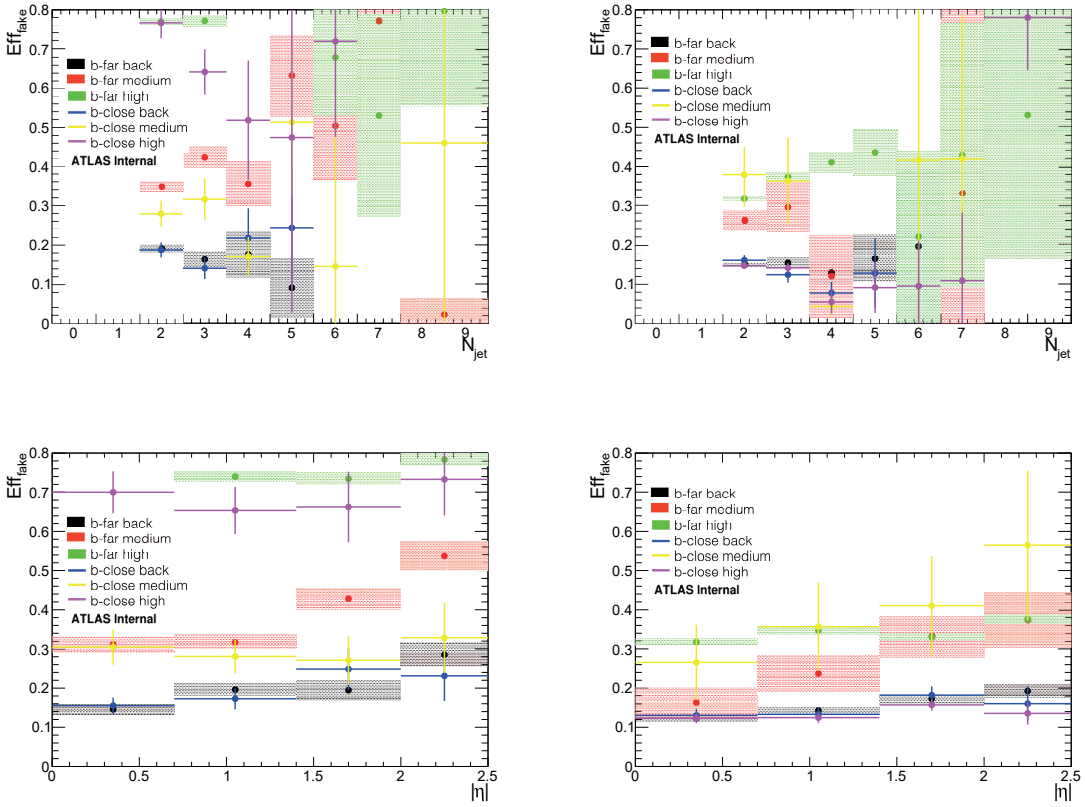

Figure 5.5: Lepton fake efficiencies as a function of the number of jets and the lepton pseudorapidity. Again, we differentiate on the basis of trigger matching and ΔR between b-jet and lepton. The dependency from the number of jets is compatible within uncertainties with a flat dependence, while the η dependence is negligible for almost all of the twelve distributions. Electrons are displayed on the left and muons on the right.

especially in the electron channel in the case of the *medium*, isolated, trigger; this might be due to a correlation between isolation and the transverse impact parameter $\left|\frac{d_0}{\sigma(d_0)}\right|$. Since d_0 is an indication of decays far from the interaction point and these are in large part due to heavy jet decay that also imply loose isolation, the correlation is likely.

Another possibility instead of using events selected by the different triggers displayed

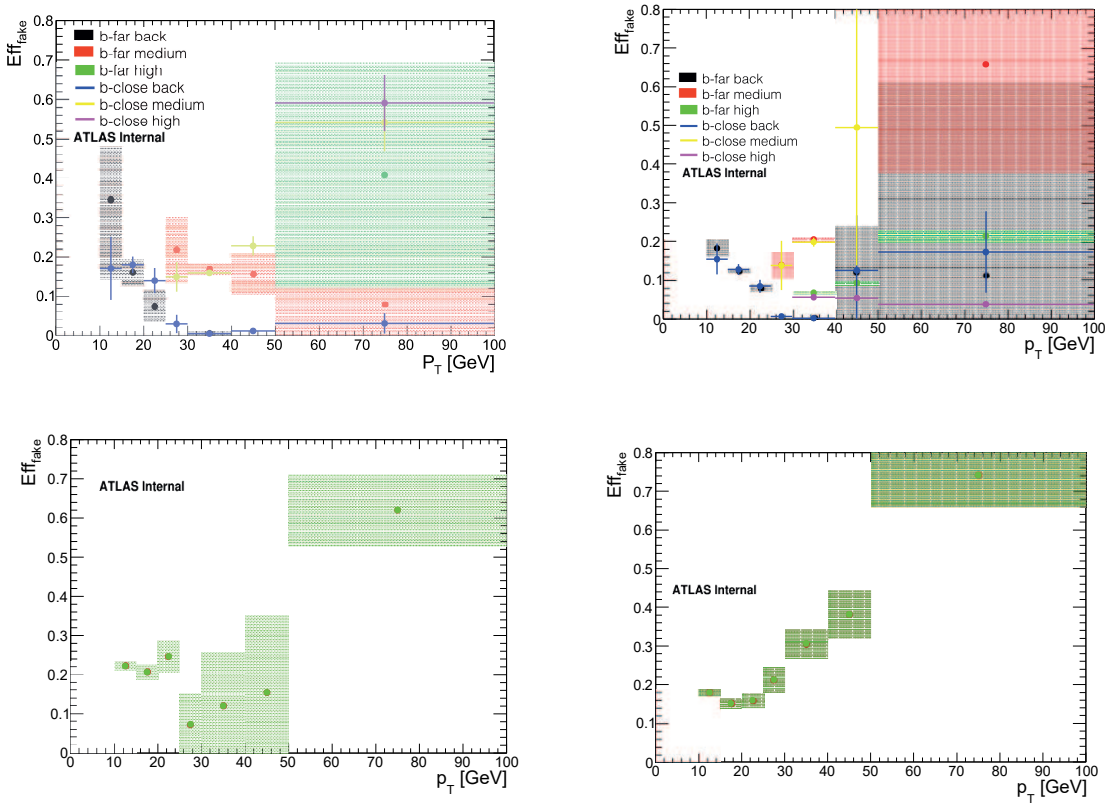

Figure 5.6: Lepton fake efficiencies determined in data using alternative definitions of fake region. The two at the top are produced using the $\left|\frac{d_0}{\sigma(d_0)}\right| \geq 5$ cut, the two at the bottom in the $2lSS$, low-N_{jet} control region. The distributions are displayed as a function of p_T and, in the first case, trigger matching and ΔR between b-jet and lepton. Electrons are displayed on the left and muons on the right.

in table 5.1 is to use events collected by just the lowest threshold trigger. In this case the statistics of the sample at larger lepton p_T would be reduced but all trigger bias would be removed. Fake rejections obtained in this way are shown in figure 5.7 and the

resulting background estimate will be shown in the next section.

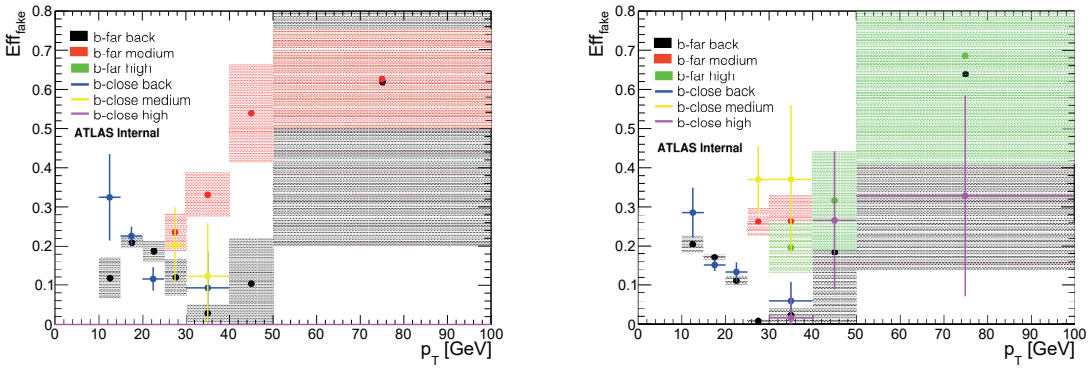

Figure 5.7: Lepton fake efficiencies determined in data using only the lowest-threshold prescaled triggers to study the differerences in using a more homogeneous dataset. The distributions are displayed as a function of p_T, trigger matching and ΔR between b-jet and lepton. Electrons are displayed on the left and muons on the right.

Another test consisted in studying the dependence from the overlap removal of loose leptons, in particular loose muons. Results of this comparison show small differences with the reference Overlap Removal and a worse correspondence with data in the control region.
Leptons were also tested without the cut $\left|\frac{d_0}{\sigma(d_0)}\right|$, to extend the statistics, with results shown in figure 5.8: the uncertainty is slightly reduced, but the shapes are compatible with the *standard* one, only leaving the selection less consistent with the tight selection.

5.3 Matrix Method estimation

The first step to verifying that the method is working correctly is to use the efficiencies produced with the MC simulations (figure 5.3) and compare the background estimations obtained using the full $t\bar{t}$ all-hadronic sample. In figure 5.9 we report the leading p_T distributions for the three different channels (ee, $e\mu$ and $\mu\mu$). The estimations obtained

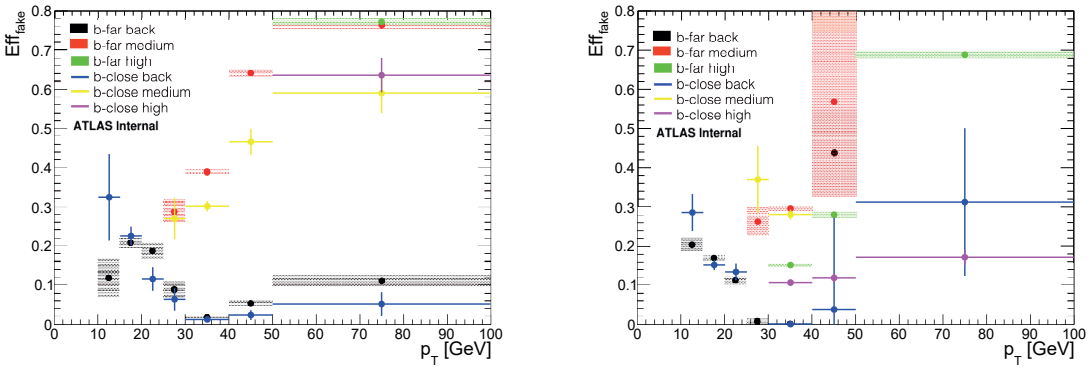

Figure 5.8: Lepton fake efficiencies determined in data without the cut $\left|\frac{d_0}{\sigma(d_0)}\right|$ on leptons. The distributions are displayed as a function of p_T, trigger matching and ΔR between b-jet and lepton. Electrons are displayed on the left and muons on the right.

using the MM[3] summed with the contributions from prompt leptons are in agreement with the overall MC distributions.

After the successful check on MC, the second step is to apply the MM to the data CR defined in the same way as the signal region, but with $1 < N_{jet} < 4$ and no additional cut on electron η, to increase statistics, necessary for a check of this kind. The contribution from charge mis-identification is estimated in a specular opposite sign control region using the charge flip rate shown in chapter 4, while all other prompt contributions to background are derived from simulation.

We follow the scheme used in section 5.2 to evaluate the impact of different efficiency estimations and parametrizations. The results that we call *standard* are obtained using $\epsilon_f(p_T)$ measured in the low-MET, low-M_T fake region and shown in 5.4. Figures 5.10 and 5.11 respectively show the standard results and the ones obtained through the $\epsilon_f(p_T, \eta)$ parametrization. The two results display little difference, as could be expected by the weak η dependence on ϵ_f. We prefer to use $\epsilon(P_T)$ instead of $\epsilon(p_T, \eta)$ singe the latter suffers for larger statistics uncertainties.

Throughout the chapter, the variation of the method used (see section 5.1.1) in the

[3] without looking at the origin of the lepton.

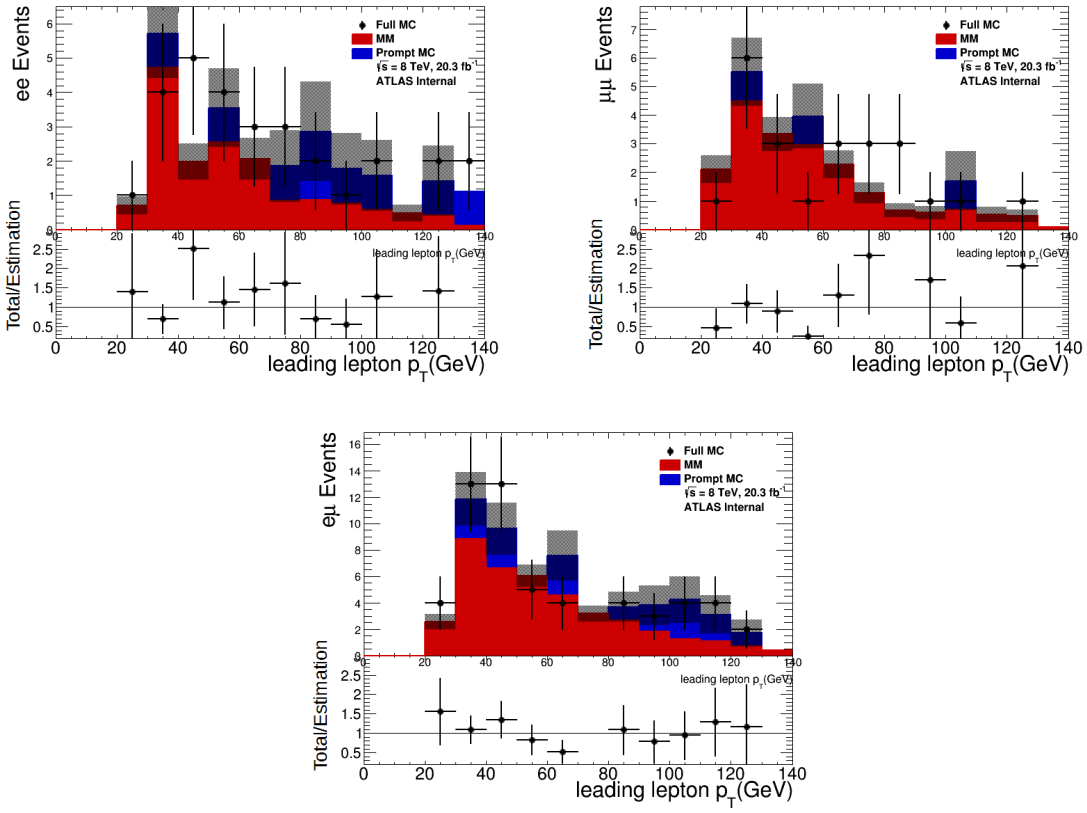

Figure 5.9: Closure test of the matrix method background estimation as a function of the p_T of the leading lepton. This is applied to the signal region of the MC non-all-hadronic sample. The uncertainty corresponds to the statistical uncertainty only. In red, the contribution of the non prompt component estimated with MM. In blue the contribution of the prompt component estimated using the truth origin of the lepton. Dots show the overall distribution obtained by the MC.

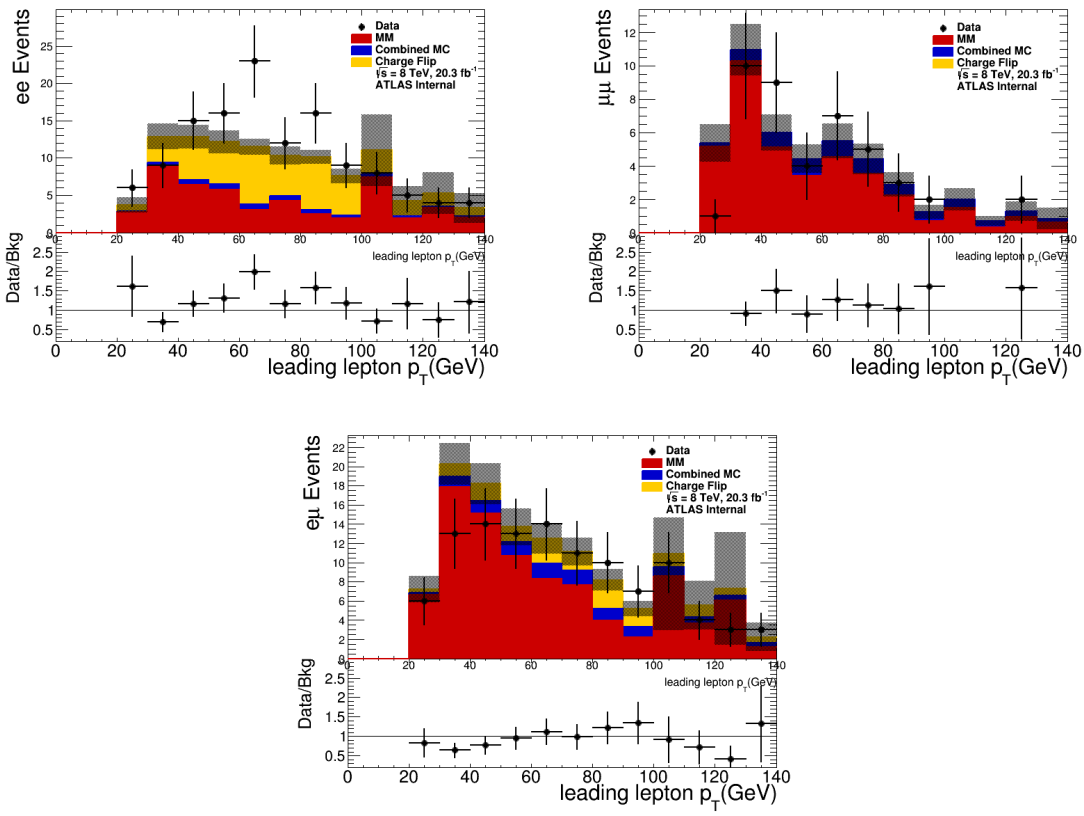

Figure 5.10: The matrix method background estimation as a function of the p_T of the leading lepton using the standard $\epsilon_f(p_T)$. The uncertainty corresponds to the systematic uncertainty, discussed in the next section (5.4), square-summed to the statistical: $\sigma = \sqrt{\sigma^2_{sysMM} + \sigma^2_{stat}}$.

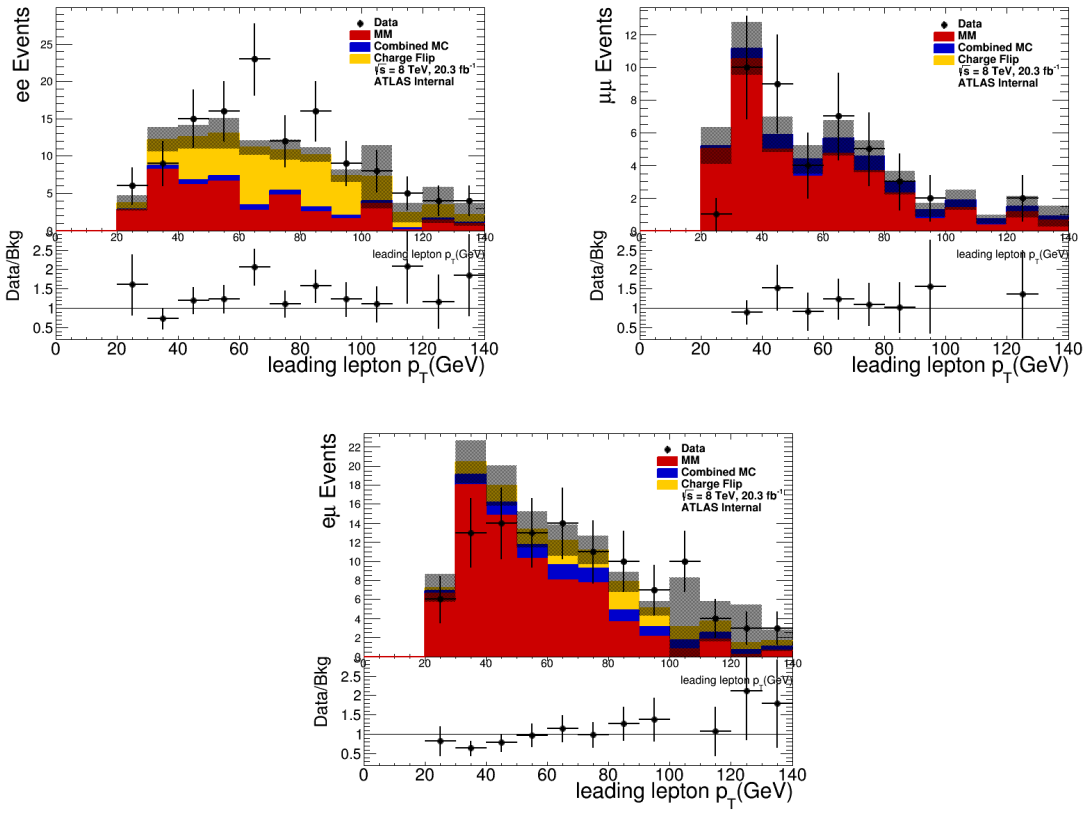

Figure 5.11: The matrix method background estimation as a function of the p_T of the leading lepton using the 2-dimensional $\epsilon(p_T, \eta)$ efficiency parametrization. The uncertainty corresponds to the MM systematic uncertainty, discussed in the next section (5.4), square-summed to the statistical: $\sigma = \sqrt{\sigma^2_{sysMM} + \sigma^2_{stat}}$.

presence of > 2 loose leptons consists in applying the MM weight to all of the lepton pairs of an event and summing up the contributions. For example, in an event with $N_l = 3$ and $N_t = 1$, the event is kept and its MM weight $w_{MM} = \sum_{i \neq j} w^{ij}_{MM}$. Figure 5.12 is produced, instead, by applying the MM only to the two leading leptons: in the same example it would be $w_{MM} = w^{kl}_{MM}$, where k and l indicate the two highest-p_T leptons. The difference between these results and the ones obtained by summing on all contributions is very small and well within uncertainties.

The test on the impact of trigger composition on efficiency derivation is obtained using

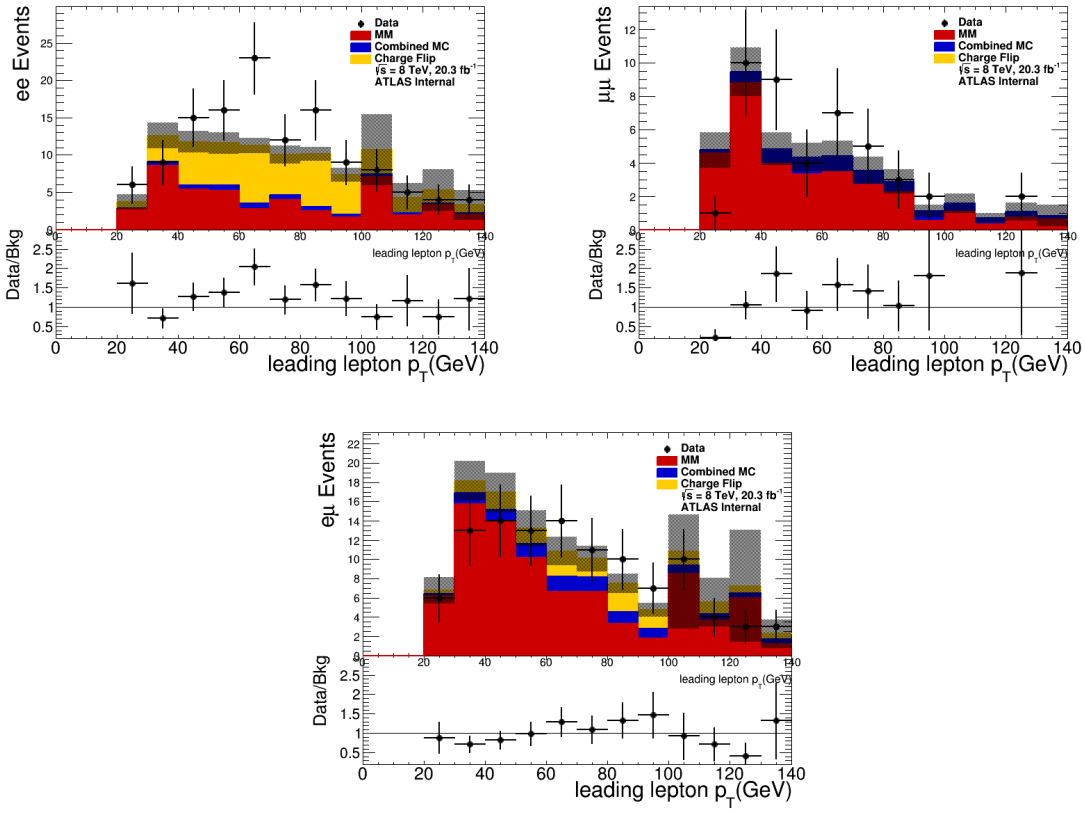

Figure 5.12: Matrix method background estimation as a function of the p_T of the leading lepton summing only the contribution coming from the couple composed by the two leading leptons. The uncertainty corresponds to $\sqrt{\sigma^2_{stat} + \sigma^2_{sysMM}}$.

the efficiencies measured using only the sub-sample acquired with the lowest-p_T prescaled trigger (figure 5.7). The results are compatible with the standard ones, but do not show

the same level of fitting to data in the control region, as can be seen in figure 5.13.

Extending the standard fake region by removing the $\left|\frac{d_0}{\sigma(d_0)}\right|$ cut from the loose definition

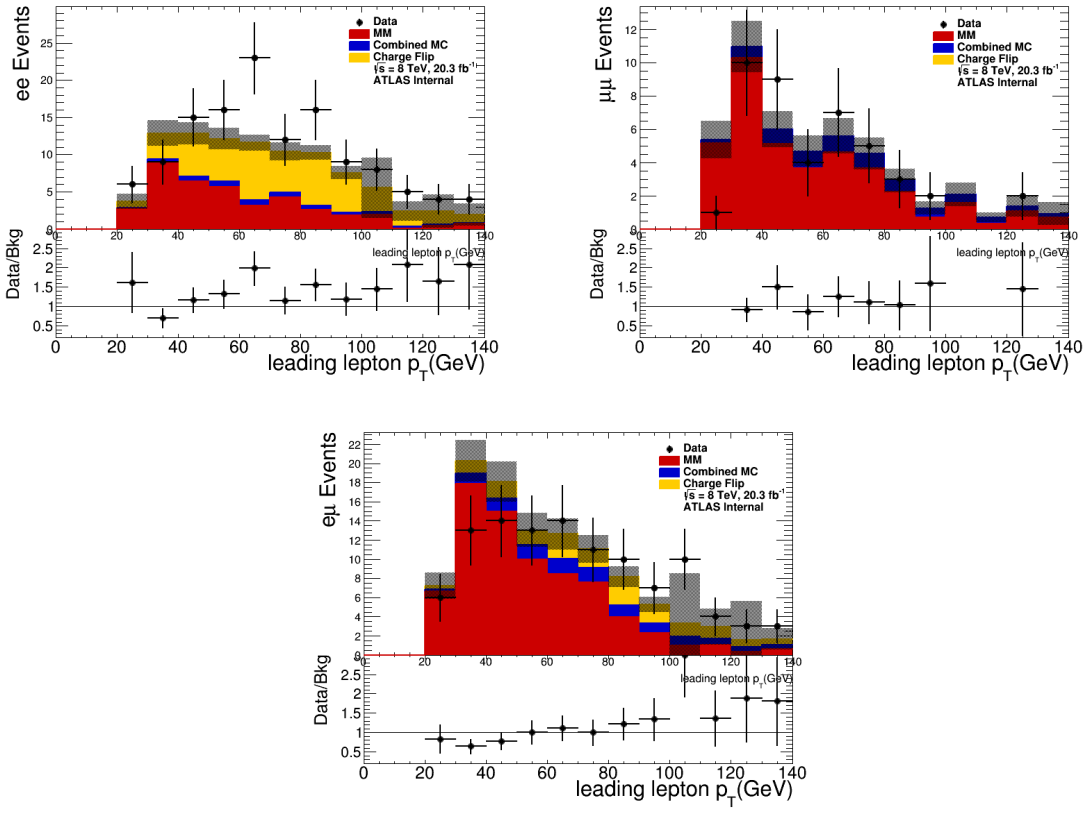

Figure 5.13: Matrix method background estimation as a function of the p_T of the leading lepton in control region, using fake efficiencies from the lowest prescaled trigger only. The uncertainty corresponds to $\sqrt{\sigma^2_{stat} + \sigma^2_{sysMM}}$.

to improve statistics yields reasonable efficiencies, as displayed in figure 5.8, but could potentially introduce a bias given by the different event topology. The resulting CR estimation is shown in figure 5.14, nearly identical to the *standard* estimation, confirming our original result.

The alternative fake regions used to calculate the efficiencies of figure 5.6 were also tested using the low-N_{jet} CR. Figure 5.15 shows the behaviour of the matrix method

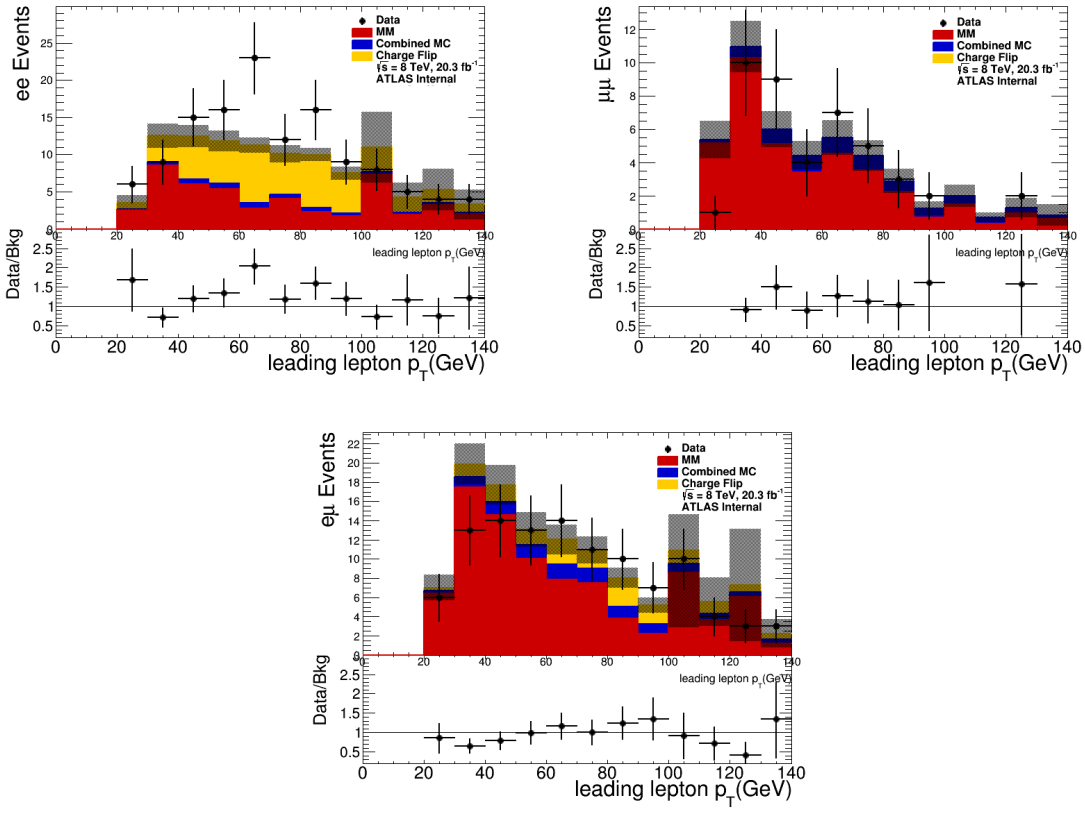

Figure 5.14: Matrix method background estimation as a function of the p_T of the leading lepton in control region, using fake efficiencies from an extended $\left|\frac{d_0}{\sigma(d_0)}\right|$ range. The uncertainty corresponds to $\sqrt{\sigma^2_{stat} + \sigma^2_{sysMM}}$.

obtained using efficiencies calculated in the $\left|\frac{d_0}{\sigma(d_0)}\right| > 5$ fake region. This displays significantly low estimations when compared to data in the CR, albeit within uncertainties, and for this reason it is not used.

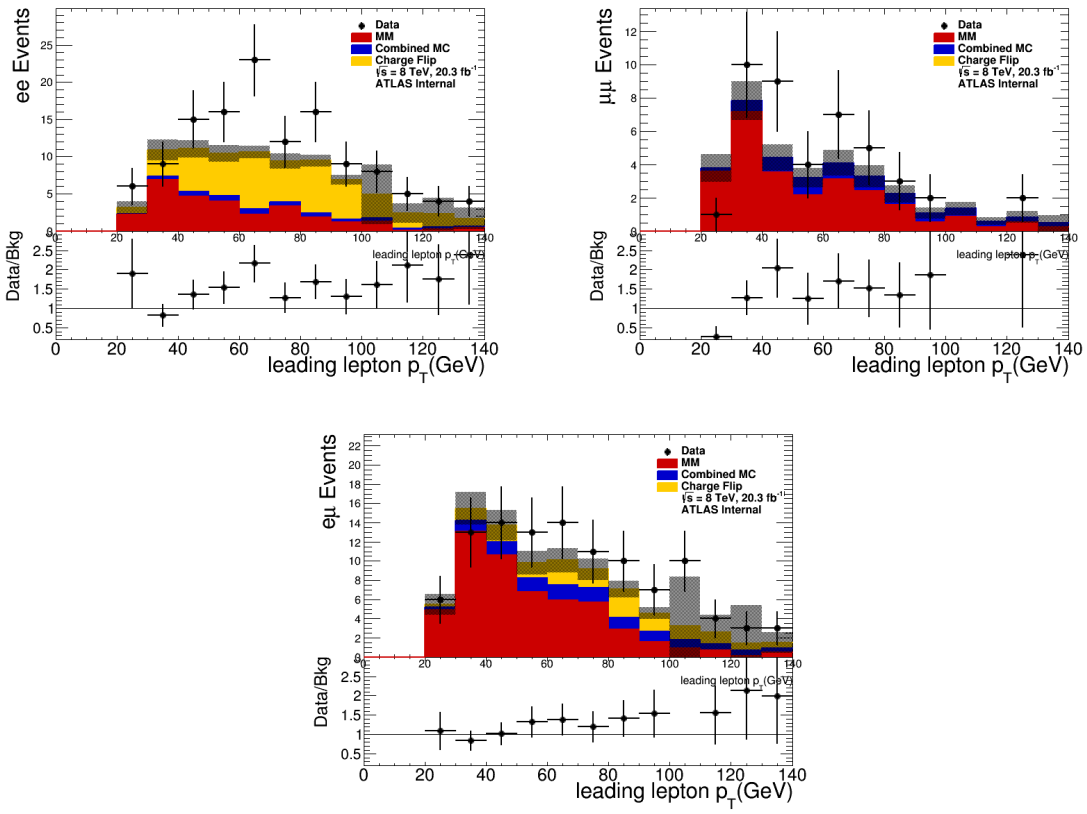

Figure 5.15: Matrix method background estimation as a function of the p_T of the leading lepton in control region, using a fake efficiencies alternative method that requires $\left|\frac{d_0}{\sigma(d_0)}\right| > 5$ to increase the purity of the non-prompt lepton sample. The uncertainty corresponds to $\sqrt{\sigma^2_{stat} + \sigma^2_{sysMM}}$.

The low-N_{jet} SS control region is not optimal when it comes to testing an efficiency produced with it, because the leptons used for ϵ_f and for the test would be exactly the same, possibly introducing correlation between the statistical uncertainties and the systematic ones produced by ϵ_f statistics. The comparison still gives a good indication

that the method works properly and produces a result in agreement with the standard efficiencies, as shown in figure 5.16.

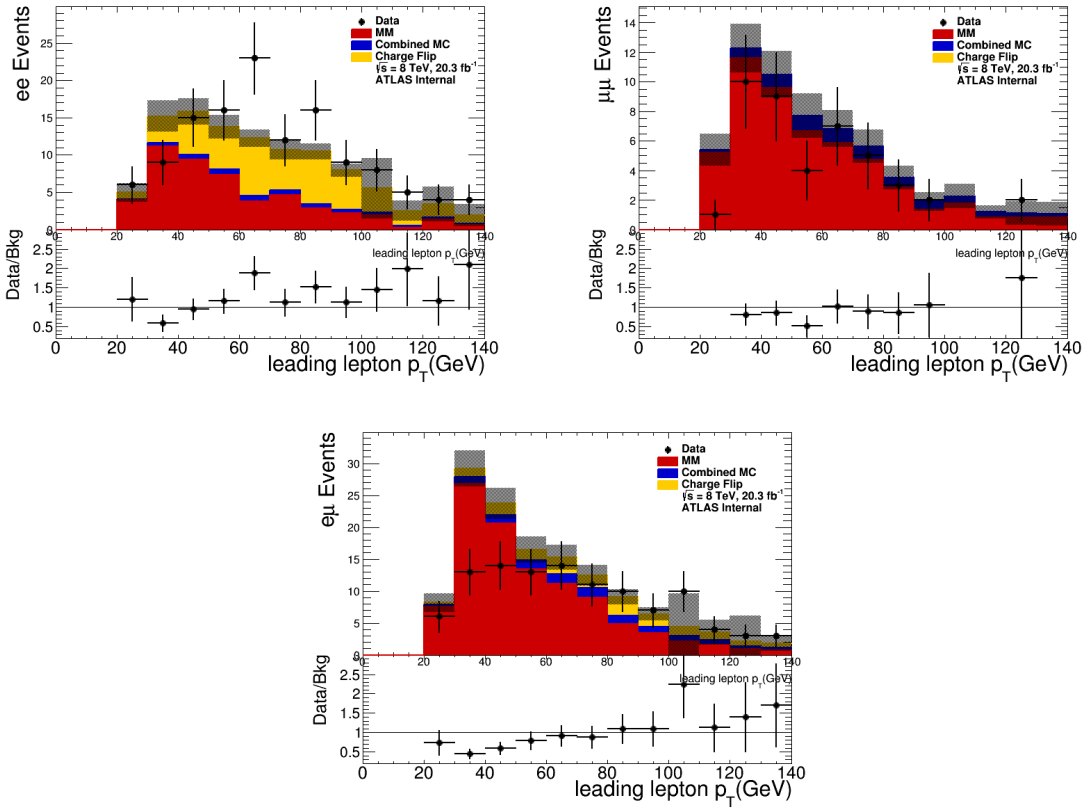

Figure 5.16: Matrix method background estimation as a function of the p_T of the leading lepton in the control region, using fake efficiencies determined in the same low-N_{jet} region. The uncertainty corresponds to $\sqrt{\sigma^2_{stat} + \sigma^2_{sysMM}}$.

The series of tests performed on the fake efficiency estimation and on the application of the matrix method reported here, together with other less-relevant checks, lead to the conclusion that the fake efficiencies displayed in figure 5.4 can be used in the signal region background estimation. The fact that all of these variations fall within a maximum of 2σ in the most extreme cases, confirms the validity of the method.

5.4 Systematic uncertainties

The matrix method weights are calculated using the measured fake and real efficiencies. The uncertainty on the MM estimation is mainly statistical from the limited size of the sample where the fake efficiencies are evaluated, but a systematic uncertainty in also considered. There are two main sources of systematic uncertainty for the background estimation: the statistical uncertainty of ϵ_f and ϵ_r and the uncertainty in the MC subtraction. The first contribution is evaluated by applying a 10% shift in the number of MC events subtracted from the fake region and testing the results on the CR; this showed a negligible difference from the *standard* efficiencies. The systematic uncertainty on the MM prediction due to the statistical uncertainty on ϵ can be evaluated in different ways:

- two shifts up and down one$-\sigma$ of the efficiency distributions are applied and the difference in MM background estimation is considered as a systematic source; this is an overestimation, since it assumes that the uncertainties are correlated across bins, while statistical uncertainties are not;

- a total of N different toy fake efficiency distributions are generating by varying the central value on each bin by a random quantity. This quantity is generated using a gaussian distribution with a deviation $\sigma = \sigma_{bin}$. The systematic uncertainty on the matrix method background is calculated by producing backgrounds with all of these distributions and calculating the deviation from the reference value μ, bin per bin: $\sigma_i = \sqrt{\frac{1}{n}\sum_{i\to n}(\mu - y_i)^2}$; this method is used in the final results;

- as a variation from the previous approach, a gaussian fit minimized using a poissonian likelihood is considered, producing smaller uncertainties except when the minimization fails to converge properly.

The two stochastic methods are theoretically a better estimation, but are susceptible to the randomization process. The three estimations methods are shown in figure 5.17 for the signal region. The second method is used in the analysis.

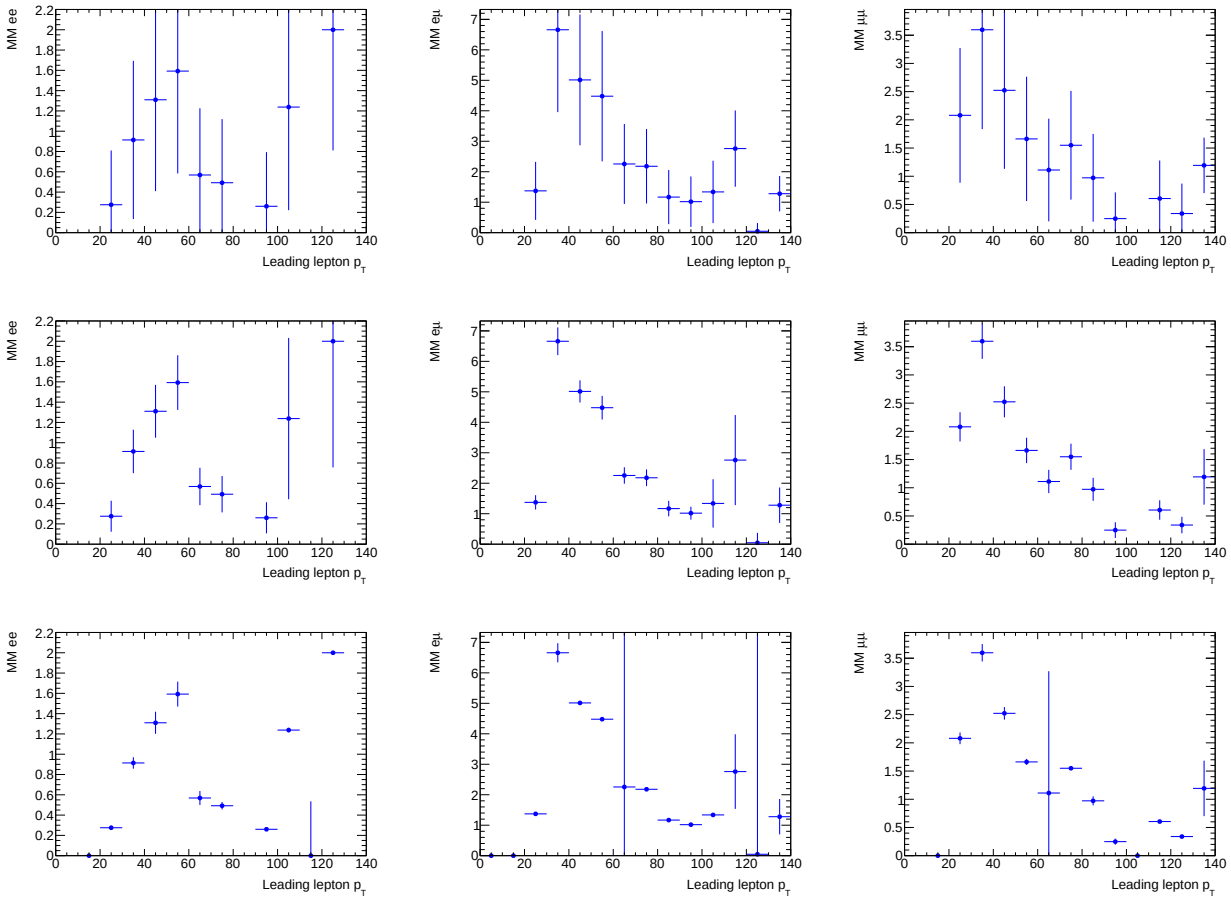

Figure 5.17: Matrix method background estimation (MM) as a function of the p_T of the leading lepton for the three event categories (ee, $e\mu$ and $\mu\mu$). The uncertainty displayed corresponds to the systematic uncertainty calculated with the two methods. The first line corresponds to the method of shifting efficiencies by 1σ up and down. The last two lines show the variations in the second method: using the deviation from the reference value and using a gaussian fit to combine the random samples.

5.5 Analysis results with the MM

The matrix method background estimation is applied to the signal region, as displayed in figure 5.18 as a function of p_T and, for comparison with the results of chapter 4, as a function of the number of jets (figure 5.19).

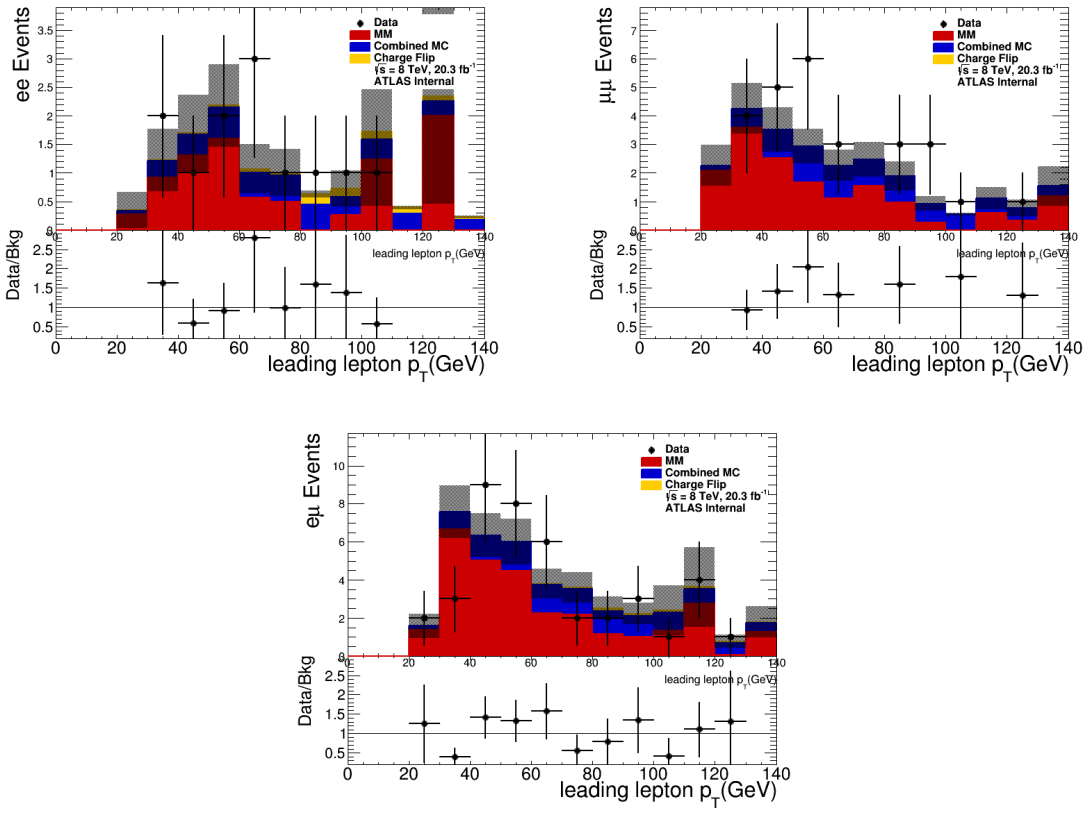

Figure 5.18: Matrix method background estimation as a function of the p_T of the leading lepton, using the standard $\epsilon_f(p_T)$ in the Signal Region. The uncertainty corresponds to the systematic uncertainty discussed in the previous section square-summed to the statistical: $\sigma = \sqrt{\sigma^2_{sysMM} + \sigma^2_{stat}}$.

The results in the three flavour channels are combined with the appropriate systematic uncertainties and the results shown in chapter 4 to produce table 5.2, leading to a combined $\mu = \sigma/\sigma_{SM}$ value in line with the Standard Model hypothesis. The central

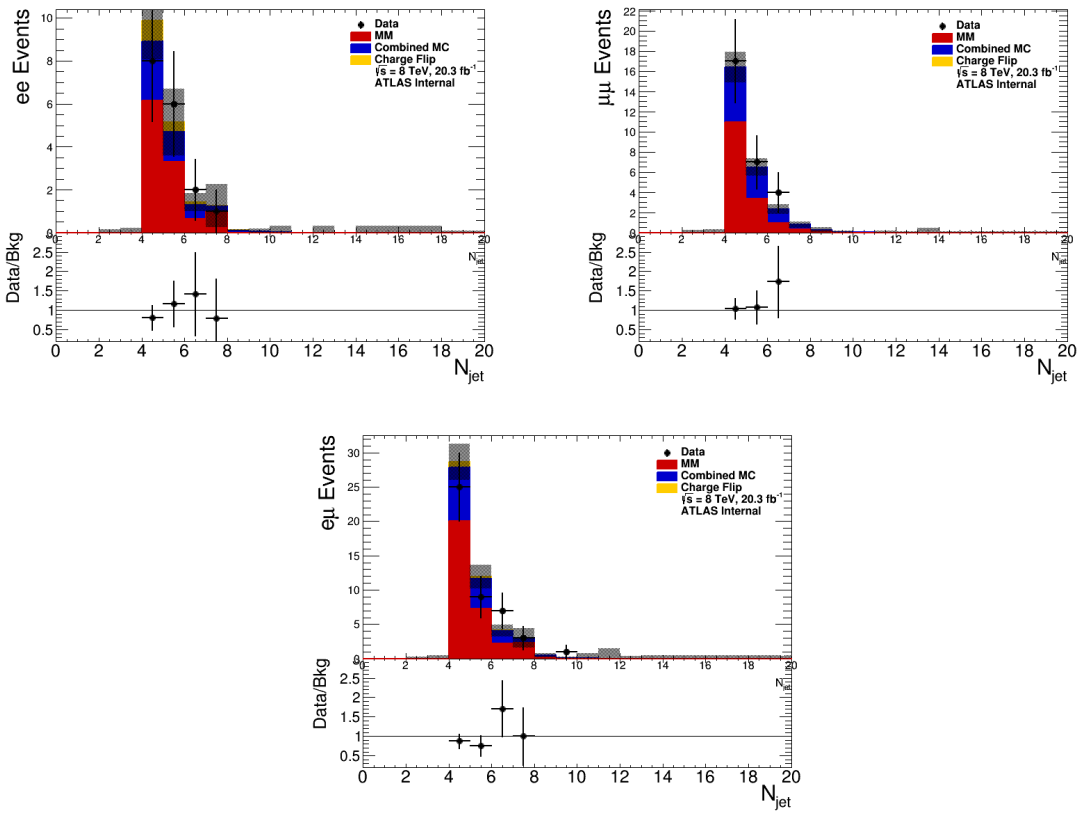

Figure 5.19: Matrix method background estimation as a function of the number of jets in the event, using the standard $\epsilon_f(p_T)$ in the Signal Region. The uncertainty corresponds to the systematic uncertainty discussed in the previous section square-summed to the statistical: $\sigma = \sqrt{\sigma^2_{sysMM} + \sigma^2_{stat}}$.

value of the measured μ is sensibly smaller than the one measured with the side-band method reported in Chap. 4 although still in agreement within the uncertainties. It is also more in agreement with the expectations from the Standard Model: $\mu = 0.8 \pm 2.1$. This results in the 95% CL limit $\mu < 4.6$.

This great deal of study on the matrix method background estimation on the well-

Category	q mis-id	Non-prompt		Total. bkg.		Exp. $t\bar{t}H$	Observed
		sideband	MM	sideband	MM		
$ee+ \geq 5j$	1.1 ± 0.5	2.3 ± 1.2	5 ± 2.5	6.5 ± 1.8	9.2 ± 2.8	0.73 ± 0.14	10
$e\mu+ \geq 5j$	0.85 ± 0.35	6.7 ± 2.4	12 ± 3	15 ± 3	20.3 ± 3.6	2.13 ± 0.41	22
$\mu\mu+ \geq 5j$	–	2.9 ± 1.4	4.8 ± 1.1	8.6 ± 2.2	10.5 ± 2.0	1.41 ± 0.28	11
$ee + 4j$	1.8 ± 0.7	3.4 ± 1.7	6 ± 3	9.1 ± 2.1	11.7 ± 3.2	0.44 ± 0.06	9
$e\mu + 4j$	1.4 ± 0.6	12 ± 4	20 ± 6.7	24 ± 5	32 ± 7	1.16 ± 0.14	26
$\mu\mu + 4j$	–	6.3 ± 2.6	11 ± 1.6	12.7 ± 2.9	17.4 ± 2.4	0.74 ± 0.10	20

Table 5.2: Table of the 6 sub-channels in the $2lSS0\tau$ channel, with listed the MM estimation, which should be compared with the Sideband one. The expected background is consistently higher, reducing the expected yield observed in the chapter 4 conclusions.

known Run I data is essential to understand its application to the first data collected by ATLAS during Run II, enabling the study of differential shapes and the use of multi-variate analyses once the luminosity collected will allow better statistics.

Chapter 6

Analysis of 2015 ATLAS data

In 2015 LHC started a new series of collisions at the new center-of-mass energy $\sqrt{s} = 13\,TeV$, ramping up the luminosity to $L_{peak} = 5 \times 10^{33} cm^{-2} s^{-1}$ and, after the first weeks of collisions, moving from $50\,ns$ to $25\,ns$ bunch spacing. Due to the increase of the production cross section, $t\bar{t}H$ rates grow by approximately a factor of 4, more than most background processes. Both the detector and the electronics and software systems have changed from Run I, being upgraded to sustain and exploit the new running conditions. This included introducing a new pixel layer (IBL) dedicated to b-tagging and the upgrade of several detectors.

In this chapter we illustrate the analysis of the data collected by ATLAS at LHC in 2015, for a total of $L = 3.25 fb^{-1}$. We focus on the three channels with the highest statistics: $2lSS0\tau$, $3l$ and $2lSS1\tau$, since even with increased cross-section, the expected number of signal events is not greater than what was measured in Run I. Due to the new running conditions and detector capabilities, the selections are re-optimized and the background estimations are reproduced.

The structure of the chapter is similar to the previous two chapters, first treating the general aspects of the analysis that have been changed with respect to Run I: simulations used, object and event selection, control region validation and background estimation. After that, a detailed description of the matrix method results follows, used for the estimation of non-prompt lepton background.

At the time of writing, the data contained in the signal regions are still in a "blinded"

state, which means that they cannot be unveiled until the analysis procedure is complete and all of the details are frozen. This is necessary not to introduce a bias into the procedure that could, for example, artificially enhance a signal.

6.1 Dataset and Simulations

The dataset used in this analysis has been recorded by the ATLAS experiment from June to November 2015. The LHC, in that period, reached a peak instantaneous luminosity of $5.22 \times 10^{23}\, cm^{-2}s^{-1}$. The total luminosity delivered by the LHC in 2015 is $4.34\, fb^{-1}$. The good quality data acquired by the experiment corresponds to a total integrated luminosity of 3.25 fb^{-1}. The triggers for Run II have similar thresholds to the ones used in Run I, but different techniques are implemented to reduce the acquisition rate: isolation requirement, identification working point (WP)[1] tightening and association with Level 1 trigger regions of interest:

- HLT_e24_lhmedium_L1EM20VH for data set, HLT_e24_lhmedium_L1EM18VH for Monte Carlo samples; these low-threshold ($24\, GeV$) electron triggers are associated with the Level 1 trigger and require a tighter identification WP;
- HLT_e60_lhmedium has high threshold ($60\, GeV$), but still requires the medium likelihood WP;
- HLT_e120_lhloose has a very high threshold ($120\, GeV$) allowing a lower identification WP;
- HLT_mu20_iloose_L1MU15 has low threshold ($20\, GeV$) thanks to the isolation and Level 1 matching required;
- HLT_mu50, with a $p_T > 50\, GeV$ threshold;

[1] A Working Points is a reference value used to represents an ensemble of other variable values that together define a non-linear cut. For example a combination of variables defines if a lepton was reconstructed properly: algorithms used, detector requirements. Working Points allow the user to choose between certain combinations of these variables.

The main backgrounds are the same as in Run I, albeit with different contributions. To simulate both signal and background at $\sqrt{s} = 13\,TeV$, several generators have been updated and used in the MC productions. The generator chosen for signal modelling is aMC@NLO+Herwig++, while for the irreducible ttV backgrounds MadGraph+Pythia8 is used. The $t\bar{t}$ background is modelled using Powheg, although it is not used for the final fit but only for MC closure in data-driven fake estimates purposes. Powheg is also used to model other top backgrounds such as single top t-channel and s-channel and Wt. Diboson backgrounds are generated with Sherpa. For Z+jets backgrounds, the nominal sample has been produced with Sherpa due to a better data modelling in validation regions, but Madgraph and Powheg modellings have also been tested.
All Monte Carlo samples are processed using Geant4 to completely simulate the interactions with the ATLAS detector. Additional pp collisions are generated with Pythia8 and overlaid to the main events to reproduce the effects of pileup from additional pp collisions in the same and nearby bunch crossings. The pileup distribution is reweighed to reflect the mean number of additional interactions observed in data.

6.2 Object Selection

Object and event selections had to be optimized again with respect to Run I due to the new running conditions and detector modifications. In particular, the new energy and cross-section produce different kinematic distributions of signal and background and the new bunch-spacing of $25\,ns$ reduces pile-up while maintaining the same or larger peak luminosity, although requiring tighter timings for every detector. The detector has changed, as well, in particular with the addition of the Inner B-Layer (IBL), an additional silicon pixel layer located very close to the beam pipe, whose main purpose is the improvement of b-tagging performance.
In the same way as in Run I, all channels share a common object pre-selection. To improve the accuracy of the matrix method background estimation, pre-selection identification and isolation requirements are chosen to be much "looser" than in the signal region. The objects used in the analysis are the same used in Run I: electrons, muons, tau hadrons, jets and b-jets. Only the differences with respect to the Run I selections

are explained in detail here.

6.2.1 Electrons

Electron candidates are reconstructed from matching an electromagnetic energy cluster to the tracks formed in the inner detector. A likelihood-based discriminant is built on shower shapes in the electromagnetic calorimeter and track qualities from the inner detector. It is used to separate prompt electrons from fakes mainly coming from hadron decays and photon conversion. The *loose* working point of the likelihood-based identification discriminant is used in this phase of pre-selection, giving approximately $\sim 95\%$ electron efficiency. A different isolation approach is used to suppress the hadronic background: a differential cut using E_T^{cone20}/p_T and p_T^{cone20}/p_T keeping a constant 99% efficiency. Impact parameter cuts are: $|z_0 sin\theta| < 2\,mm$ and $|d_0/\sigma(d_0)| < 10$. All of these selections produce a lower purity than the one obtained in Run I, to enable keeping the same selection for the matrix method *loose* definition, that requires a clear separation between *loose* and *tight* definitions.

6.2.2 Muons

Muon candidates are reconstructed through a combination of the inner detector and muon spectrometer tracks like in Run I. Muon identification is defined by using the *loose* identification working point and by passing the track quality requirements. The same isolation variables computed for electrons are used: E_T^{cone20}/p_T and p_T^{cone20}/p_T. Flat efficiency of 99% in $\eta - p_T$ plane is chosen for muons, too, with the same cuts on the longitudinal impact parameter $|z_0 sin\theta| < 2\,mm$ and transverse impact parameter $|d_0/\sigma(d_0)| < 10$. In the this case the *matrix method* is tested with and without isolation for the *loose* definition.

6.2.3 Tau

Hadronically decaying taus are reconstructed using clusters both in the electromagnetic and the hadronic calorimeters [95]. Hadronic taus are identified using the *medium*

working point of a Boosted Decision Tree. Checks on the hadronic charge $q = \pm 1$ and on the number of associated tracks $N_{track} = 1$ or 3 are applied.

6.2.4 Jets and b-jets

Jets are reconstructed using the "anti$-k_t$" algorithm with distance parameter $R = 0.4$, starting from topological clusters in the calorimeters [96]. Jets are accepted within the fiducial region $p_T > 25\,GeV$ and $|\eta| < 2.5$. To discriminate between hard scatter jets and pileup, jets with $p_T < 50\,GeV$ and $|\eta| < 2.4$ must satisfy a 0.64 cut on a multivariate variable called the jet-vertex-tagger (JVT) [97], which gives about 92% efficiency and approximately 2.0% fake rate.
Jets containing b-quarks are identified using the MV2c20 algorithm, using a working point that gives a $\sim 77\%$ efficiency to tag b-hadron jets.

6.2.5 Overlap Removal

An overlap removal (OR) is performed among objects to decrease the probability of having multiple objects reconstructed from the same true particle. In this early analysis, the OR is identical to the one performed in Run I and explained in Chapter 4, as summarized in table 4.2.

6.3 Signal and Control Regions

The channel definition described in this section is exclusive in light leptons and hadronic tau multiplicity, ensuring no overlap between them. Each channel had a second optimization stage that tightens the object requirements with respect to the common object pre-selection.
The signal region definition is the same used in Run-I, but only the three most significant channels are included in this first Run II analysis: $2lSS0\tau$, $2lSS1\tau$ and $3l$. The control regions are used to develop and test background estimations, both simulated and data-driven.
The lepton counting for the channel is performed using the lepton selection detailed in

sections 6.2 and 6.2.5. For the sake of the matrix method implementation explained in chapter 5 and used later in this chapter, the leptons passing the object pre-selection are considered "loose", while the additional object cuts implemented in the three signal regions define a "tight" lepton.

6.3.1 $2lSS0\tau$

In this channel only electrons or muons with transverse momentum greater than $25\,GeV$ are used. Other selection requirements are tightened to increase the S/B and $S/\sqrt{B}$ ratios in the same way as described in chapter 4. The two remaining leptons must be of the same sign.
For electrons, the likelihood based discriminant working point is tightened to *TightLH*, while for isolation both $E_T^{cone20}/p_T < 0.06$ and $p_T^{cone20}/p_T < 0.06$ are required, corresponding to the *FixedCutTight* working point. For muon candidates, track based isolation p_T^{cone20}/p_T has to be less than 0.06, corresponding to the *FixedCutTightTrackOnly* isolation working point.

6.3.2 $2lSS1\tau$

In this channel, exactly one hadronic tau is required of opposite sign with respect to the light lepton pair. Similarly to the 0τ channel, electrons are required to satisfy E_T^{cone20}/p_T, $p_T^{cone20}/p_T < 0.06$ and the *tight* likelihood identification, while muons have to pass $p^{cone30}/p_T < 0.06$ and the *loose* identification.
The leading lepton must be trigger matched and have a $p_T > 25\,GeV$, while the subleading lepton p_T cut is $15\,GeV$.

6.3.3 $3l$

This channel requires exactly 3 light leptons and is inclusive in the number of τ leptons. The sum of light lepton charges has to be equal to 1 due to the topology of the event. The two same charge leptons are required to pass the same object selection of the $2lSS0\tau$ channel, with the exception of a $p_T > 20\,GeV$ for both. To reduce the dilepton resonant background and the Z-boson background, the invariant mass of any

two opposite sign and same flavour leptons has to be greater than $12\,GeV$ and outside the $[81,\ 101]\,GeV$ Z mass peak.

6.3.4 Control Regions

The description of data by various Monte Carlo samples (MC) is tested over various validation regions defined in Table 6.1 together with what is used to verify the data-driven background estimation. Additional MC verification regions are used with respect to Run I.

6.4 Background Estimations

Signal region optimization reduces the background significantly, but a solid background estimation is still necessary to evaluate the remaining contamination in the signal regions. While irreducible backgrounds are modelled using Monte Carlo simulations, reducible backgrounds can be estimated using data-driven techniques. In this section we focus on reducible background estimation, since the MC simulations used for irreducible backgrounds were introduced in the first section of this chapter.

6.4.1 $2lSS0\tau$

The dominant backgrounds of this channel, just as for Run I, are irreducible backgrounds containing two prompt same charge leptons from $t\bar{t}V$ processes and reducible background events from $t\bar{t}$. The former one is verified using a dedicated control region (table 6.1). The latter contributes to the signal through opposite sign dileptonic events where one of the two lepton charges is mis-identified or through single lepton events where a second lepton is produced from a heavy quark decay. Opposite-sign leptons can also come from SM processes such as Drell-Yan and W^+W^-.

The contribution of the charge mis-identification background to the same-sign dilepton signature is estimated by measuring the probability that lepton charge is mis-

CR	Selection and purpose
Inclusive OS dilepton (ee, $e\mu$, $\mu\mu$)	2 OS leptons, leading lepton $p_T > 25$ GeV, sub-leading lepton $p_T > 10$ GeV, $M(\ell^+\ell^-) > 40$ GeV, with 2ℓ lepton selections for muons and electrons Demonstrate normalization of Z, lepton scale factors
OS $t\bar{t}$ (top dilepton) (ee, $e\mu$, $\mu\mu$)	As for inclusive OS, but ≥ 2 jets and ≥ 1 MV2c20 77% btagged jets, ± 10 GeV veto around Z mass Demonstrate normalization of top, check btag scale factors
$t\bar{t}$	2ℓ lepton selection require exactly 1 b-tagged jet and ≤ 3 reconstructed jets Verify non-prompt lepton background
$t\bar{t}W$	2ℓ lepton selection require ≥ 2 b-tagged jets and ≤ 3 reconstructed jets Verify $t\bar{t}W$ normalization, modelling
WZ on-shell	3ℓ lepton selection, require ≥ 1 OS SF pair within 10 GeV of Z and b-veto Verify WZ normalization, N_{jet} spectra
$W\ell\ell$ off-shell	As above but Z cut reversed Verify off-shell modelling
WZ+HF on-shell	As for WZ on-shell but require ≥ 1 77% b tagged jets Verify heavy flavour modeluing for WZ
$t\bar{t}Z$	3ℓ lepton and jet selection require at least one OS SF pair within 10 GeV of $m_Z = 91.2$ GeV requiring 4j2b Verify $t\bar{t}Z$ normalization, modeluing
ZZ	4ℓ lepton selection, require 2 OS SF pair within 10 GeV of Z Verify ZZ normalization, N_{jet} spectra
4ℓ inclusive	4ℓ lepton selection, exclude ZZ candidates Verify off-shell 4ℓ modeluing

Table 6.1: Description of the validation and control regions being designed for each background used in Run II.

reconstructed using same likelihood fit used in Run I and explained in Chapter 4. The main sources of systematic uncertainties come from statistical uncertainty of the electron sample, statistical uncertainty of the factor used for high p_T extrapolation, closure test of Likelihood method and truth-matching method and the background subtraction in selecting Z events. The measured charge flip rates from data are shown in figure 6.1, where both statistical and systematic uncertainty are included. The rate of charge mis-identification is higher than in Run I, mainly due to the different identification WP used in the Run II selection.

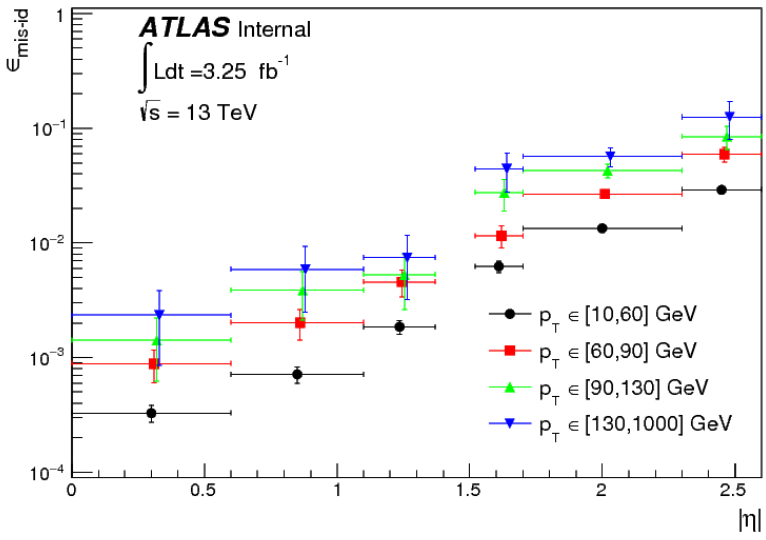

Figure 6.1: Electron charge mis-identification rates measured in data with the likelihood method on Z events (black points, red squares and green triangles) as a function of $|\eta|$ and parametrized in p_T. The 2015 dataset has been used to estimate the rates below 130 GeV. Above this value, the charge flip rates have been estimated by extrapolating the rates in the region where the $p_T \in [90, 130]$ GeV with a p_T dependent factor extracted from simulated $t\bar{t}$ events (blue triangles). Statistical and systematic uncertainties have been included in this plot.

The main fake background estimation techniques used in the analysis at this early stage are the matrix method (MM) and the side-band method (also called fake factor

method). The former provides background shapes and constitutes a fundamental step for the analysis of the future Run II data, while the latter constitutes a solid cross-check of the estimation. The matrix method is described in detail in the next section. The side-band method is the same used in Run I: a fake transfer factor θ is used to extrapolate the number of fake leptons from a control region similar to the signal one but with an inverted tight cut. Anti-tight electrons and muons are defined as leptons that pass the baseline selection but do not satisfy the tight selection. The transfer factors are calculated in regions with $N_{jet} \leq 3$. To avoid contaminations from other background sources, the irreducible ones are subtracted using MC simulations, while charge mis-id is subtracted using the same method shown for signal.

6.4.2 $2lSS1\tau$

The main background contributions in this analysis channel derive from $t\bar{t}$ and single-top events (reducible, generically defined as *top*) as well as $t\bar{t}V$ events (irreducible). Smaller but non-negligible contributions are from diboson events. Negligible backgrounds are due to Z+jets, W+jets and QCD multi-jet events.
Contamination from top production is dominated by fakes and objects with mis-identified electric charge. Data-driven estimates using side-band regions are used for fake background determination in order to avoid the MC-based uncertainties, while charge mis-identification is treated in the same way as the 0τ channel. The fake estimation uses a variation of the method used in the 0τ channel, called "ABCD". The CR regions for the sideband method are defined as follows:

- A: SS, $N_{B-jets} \geq 1$, $N_{\tau} = 1$, $N_{jets} \geq 4$, $N_{lep}(tight) = 2, N_{lep}(loose) = 0$
- B: SS, $N_{B-jets} \geq 1$, $N_{\tau} = 1$, $1 < N_{jets} < 4$, $N_{lep}(tight) = 2, N_{lep}(loose) = 0$
- C: SS, $N_{\tau} = 1$, $N_{jets} \geq 4$, $N_{lep}(tight) = 1, N_{lep}(loose) = 1$
- D: SS, $N_{\tau} = 1$, $1 < N_{jets} < 4$, $N_{lep}(tight) = 1, N_{lep}(loose) = 1$

In the regions that don't have high $t\bar{t}$ purity, the other backgrounds are subtracted using MC simulations. The result of the estimate yields to:

$$N^{A}_{fake} = \frac{N^{C}_{Data}}{N^{D}_{Data}} N^{B}_{Data} = 0.38^{+0.28}_{-0.17}. \tag{6.1}$$

The uncertainty given here is statistical only and includes the statistical uncertainty of the data yields in the three CR's as well as those of the subtracted MC yields. The low data event yield of the CR C of only 4 events is dominating the statistical uncertainty and leads to the asymmetric error treatment.

6.4.3 $3l$

The main background contributions for this channel come from the production of $t\bar{t}V$, diboson processes and $t\bar{t}$ dileptonic events with additional fake leptons from hadron decays (mainly from Bottom meson decays). The $t\bar{t}$ background is estimated using data-driven methods. The irreducible background from $t\bar{t}V$, tZ and di-boson production is estimated from simulated events.
The non-prompt lepton background is estimated through the same technique used for the $2lSS0\tau$ channel and, in general, for the Run I analysis. A transfer factor θ is used to convert the number of events counted in a dedicated CR into the number of fake events contained in the SR. This θ is evaluated as the ratio of the number of events with 3 leptons all tight, over the number of 2 tight + 1 anti-tight of the CR:

$$\theta = \frac{N_{\ell\ell\ell}}{N_{\ell\ell\bar{\ell}}} \tag{6.2}$$

where the anti-tight leptons are defined in the same way as the tight ones, but inverting the isolation cut. The resulting background estimation, depending on the flavour of the fake lepton, is:

$$N_{data,e,SR} = 1.49 \pm 0.67 \tag{6.3}$$

$$N_{data,\mu,SR} = 0.44 \pm 0.13(stat) \pm 0.13(sys) \tag{6.4}$$

6.5 Background estimation with the Matrix Method

The matrix method (MM) was introduced in chapter 5 as a mean to calculate the non-prompt lepton contribution to the background of the $t\bar{t}H$ multileptonic signal. The main advantage of this method with respect to other data-driven techniques is the possibility to produce the background shape as a function of any kinematic or topological variable. This aspect is essential when the statistic is large enough to perform analyses based on the shapes of the kinematic variables. The situation in Run II is not different from Run I, due to the lower luminosity. We apply this method to the $2lSS0\tau$ channel.

6.5.1 Real and Fake Efficiencies

Due to the different object pre-selection and the limited availability of datasets in this early analysis stage, the regions defined in chapter 5 for the measurement of real and fake efficiencies have undergone some variations.
Real efficiencies were produced in two different *real regions*

- a real region based on the Z mass peak, like the one described in chapter 5, defined by having 2 OS leptons of the same flavour with an invariant mass $M_Z - 7.5\,GeV < M_{ll} < M_Z + 7.5\,GeV$; the region is inclusive in the number of jets; results in this region are compared to those obtained using a Z inclusive MC simulation;
- a real region based on the $t\bar{t}$ background is used, with $N_{b-jet} \geq 1$, $1 < N_{jet} < 4$ and two OS leptons that pass the signal preselection; results in this region are compared to those obtained using an inclusive $t\bar{t}$ semileptonic and dileptonic MC sample;

In both cases a tag-and-probe method is used to extract the real efficiencies, where the highest-p_T tight lepton is used as tag to select the event and the second lepton is used as probe. With the addition of the $t\bar{t}$ real region in Run II analysis we are able to measure efficiencies for events more similar in terms of jet multiplicity to the ones expected for the $t\bar{t}H$ signal region.

The real efficiencies are produced as a function of p_T, since it is the variable to which they are most sensitive. To test the stability of the resulting ϵ_r in the transition

between the control regions and the signal region, the parametrizations in N_{jet} and $|\eta|$ are also used. As for the Run I MM, an additional distinction on the base of the trigger matching of the probe lepton is also used, since the difference in some kinematic regions is significant. All of these results are shown in figure 6.2 together with a test of the dependence from the lepton pseudorapidity η, all compared with the corresponding MC simulation.

Figure 6.3 shows the distribution of the real efficiencies for electrons and muons as a function of the p_T of the probe using the $t\bar{t}$ control region. Results are compatible within uncertainties.

The fake regions defined in this analysis are similar to what is used in Run I. Multiple regions are used to ensure a small dependence from the method used:

- single lepton trigger, fake-enriched by requiring at least one b-jet, low missing transverse energy (MET) and low transverse mass (M_T), thus removing most of the prompt W+jets $\rightarrow l\nu + jets$ leptons; this region is mostly used for electrons;
- single lepton triggers, enriched in fakes by requiring at least one b-jet and $d0/sigd0 > 5$, removing most prompt leptons coming from the primary vertex; this region is mostly used for muons;
- the low-N_{jet} CR, defined by $1 < N_{jet} < 4$, $N_{b-jet} \geq 1$ and exactly 2 SS leptons, one of which must be matched with the event triggers; this region is used for both leptons and is the only one used in MC simulations for comparison with data and for the "closure test".

The initial idea for the lepton selection was to keep the requirements used in the pre-selection phase, in order to remove from the $2lSS0\tau$ matrix method application the contamination from events belonging to other signal channels, in particular $3l$. The limiting factors to this strategy are the restricted number of events in the fake control regions and the fact that the matrix method requires a substantial difference between real and fake efficiencies in order to work properly, otherwise the fake estimation for some events might diverge. For electrons this strategy works out fine, but for muons this is not the case. In figure 6.4 we compare muon fake efficiencies obtained by applying

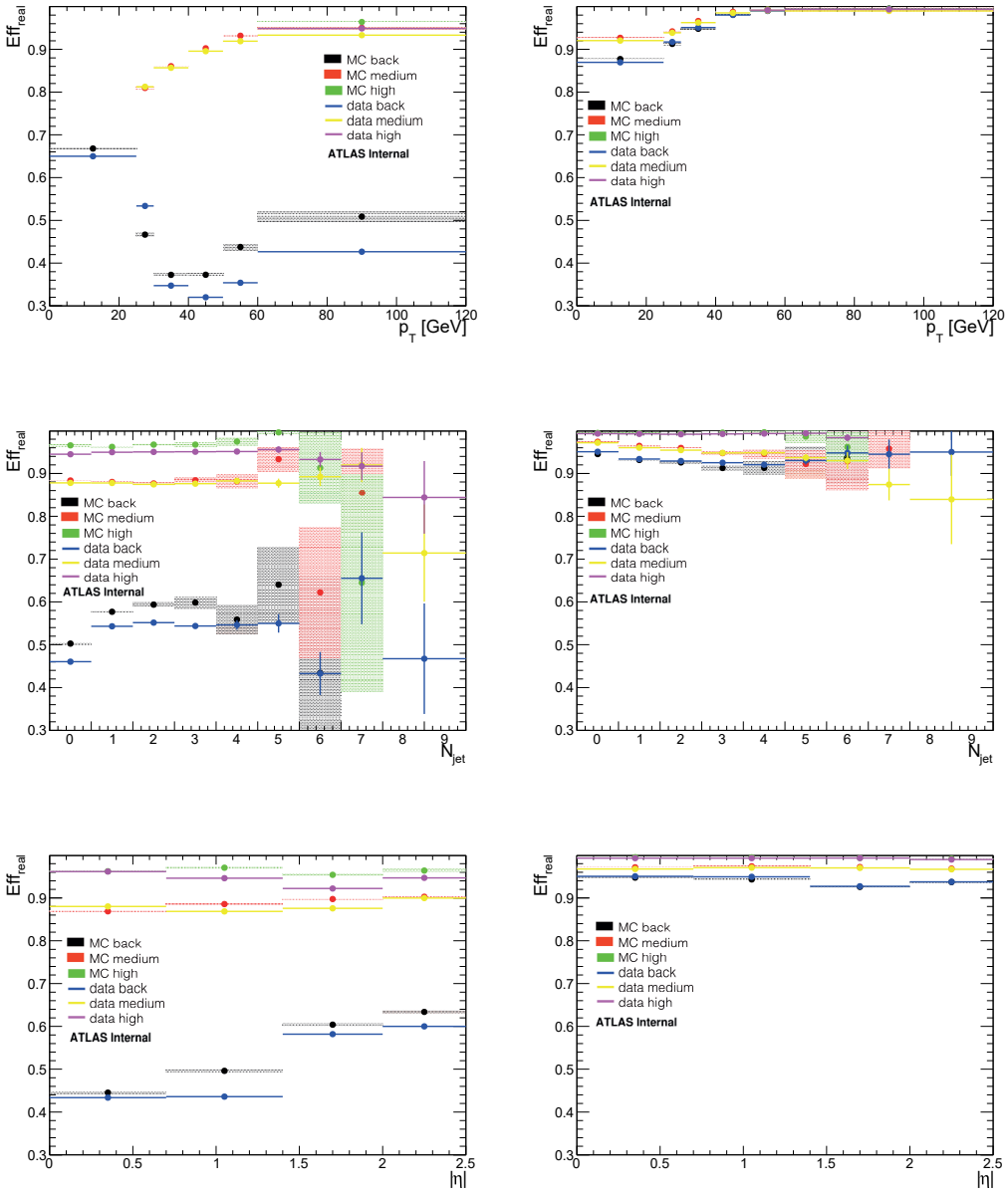

Figure 6.2: Real efficiency distributions as a function of p_T, N_{jet} and η for electrons (left) and muons (right), differentiated on the base of the lepton trigger matching, measured using a tag-and-probe method on the Z mass peak.

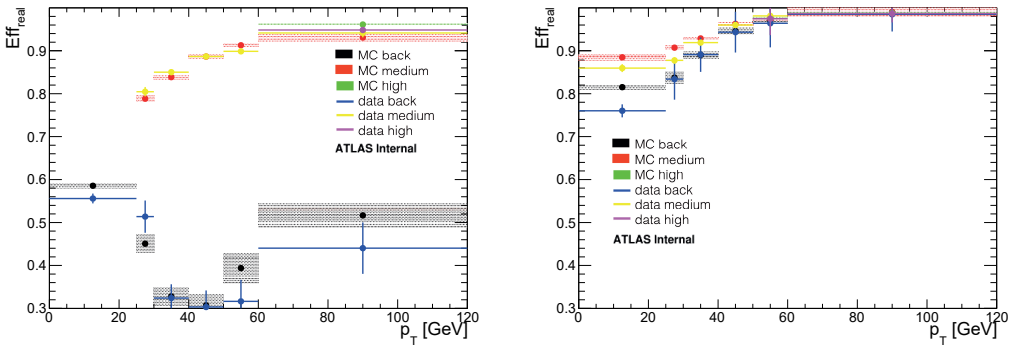

Figure 6.3: Real efficiency distributions as a function of p_T for electrons (left) and muons (right), differentiated on the base of the lepton trigger matching, measured using a tag-and-probe method on the $t\bar{t}$ control region.

the proper isolation cut in pre-selection and by removing it. The sharp rise at high-p_T is observed using all methods and control regions, indicating that this isolation working point effectively reduces fakes in the high-p_T region for muons.

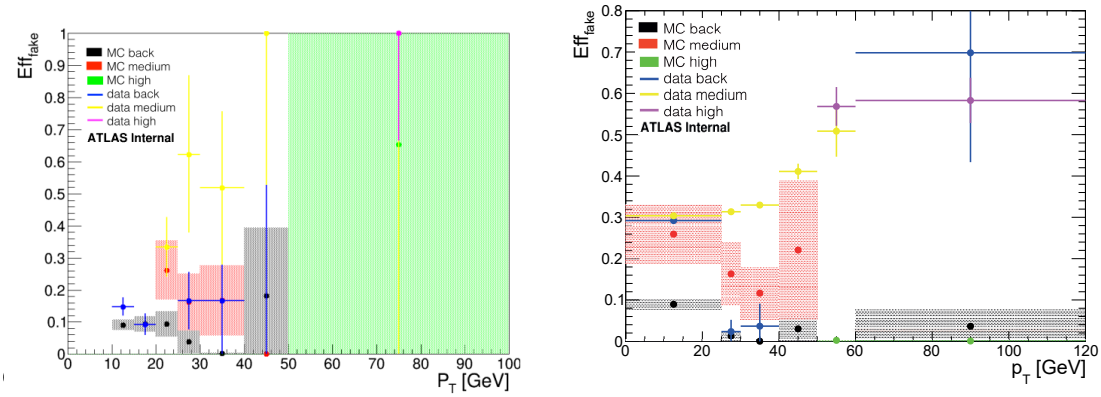

Figure 6.4: Muon fake efficiency measured in the low-N_{jet} control region with isolation applied (left) and without isolation applied (right) in the pre-selection phase.

Figure 6.5 shows the comparison of the fake estimates using the different CR's. The single lepton ones use the triggering lepton to measure the efficiencies, while the low$-N_{jet}$

regions is exploited through a tag-and-probe technique where the highest-p_T tight lepton is used as tag and the other is the probe. The results obtained have differences mostly within uncertainties.

The stability of the results with respect to N_{jet} is also tested, as is shown in figure 6.6.

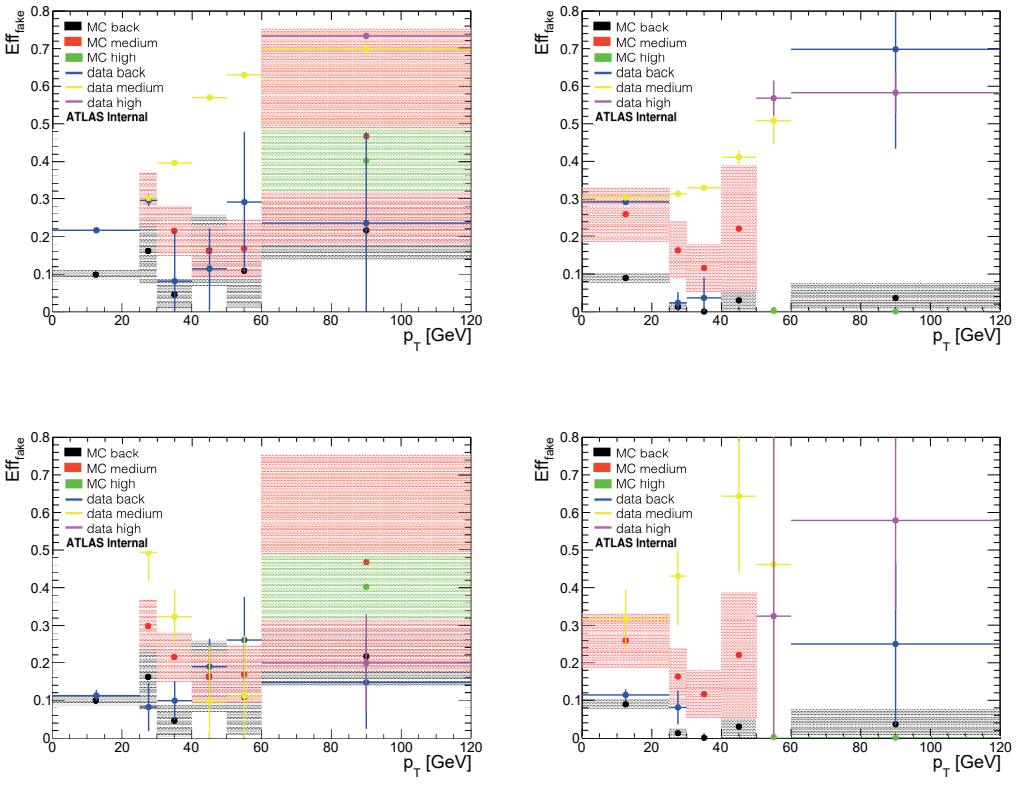

Figure 6.5: Electron (left) and muon (right) fake efficiencies measured as a function of the lepton p_T in the single lepton control regions (top) and low-N_{jet} control region (bottom) without isolation applied in preselection. The simulation used as a comparison in both estimations is produced only in the low-N_{jet} control region.

The small dependence ensures that the use of these efficiencies in the signal region is accurate within uncertainties for large N_{jet}.

The first test of the method is performed using MC simulations, where a sample containing dileptonic and single-lepton $t\bar{t}$ events is used both to produce the efficiencies

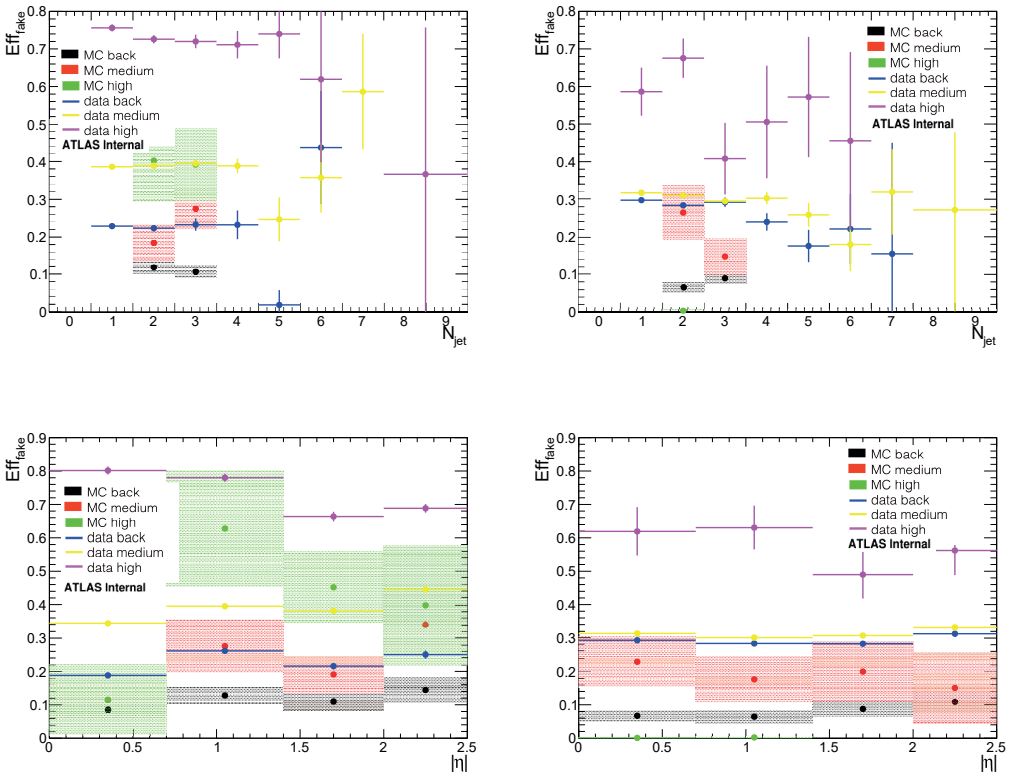

Figure 6.6: Electron (left) and muon (right) fake efficiencies measured as a function of the number of jets and the lepton pseudorapidity $|\eta|$ in the single lepton fake regions. The MC used in the comparison is obtained using the low-N_{jet} control region selection.

already shown and to test the signal region results against the full MC simulation. Figure 6.7 and 6.8 shows the comparison of the total MC sample with the estimation made with the matrix method summed with the prompt contribution in the signal region, as a function of, respectively N_{jet} and p_T.

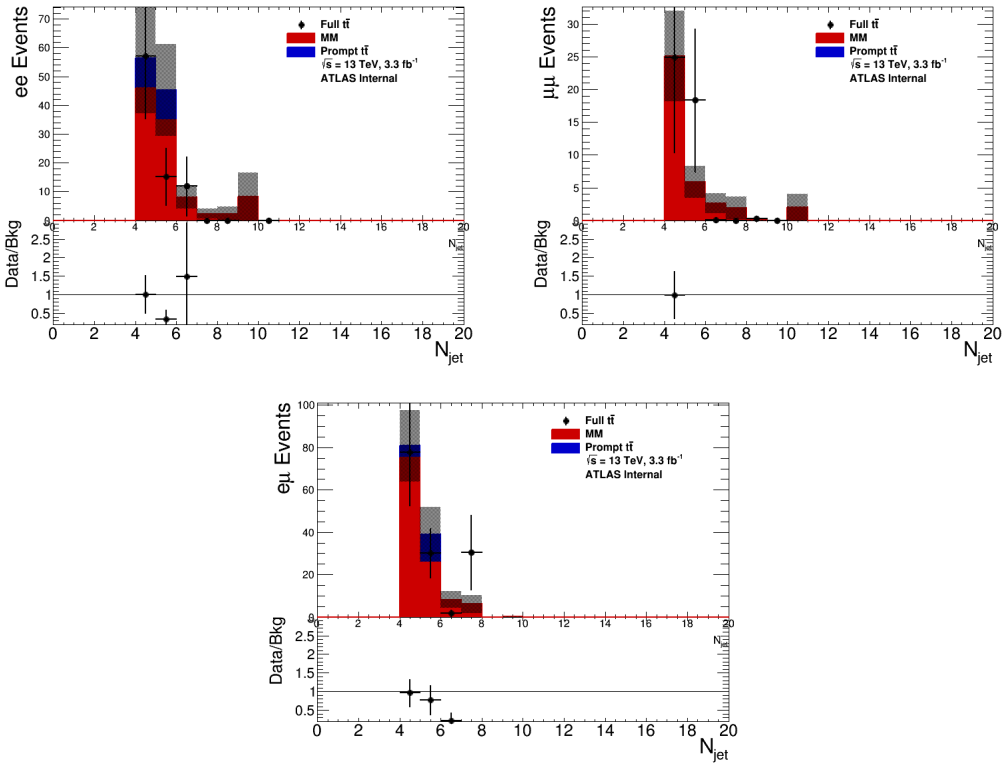

Figure 6.7: "Closure test" of the matrix method application as a function of the number of jets, made using ϵ_r and ϵ_f calculated in the low-N_{jet} control region. Efficiency calculation and test are performed on the $t\bar{t}$ MC sample composed of dileptonic and semileptonic events. Prompt $t\bar{t}$ refers to dileptonic prompt events selected using the MC generator truth. The selection used in this test is the one used for the signal region.

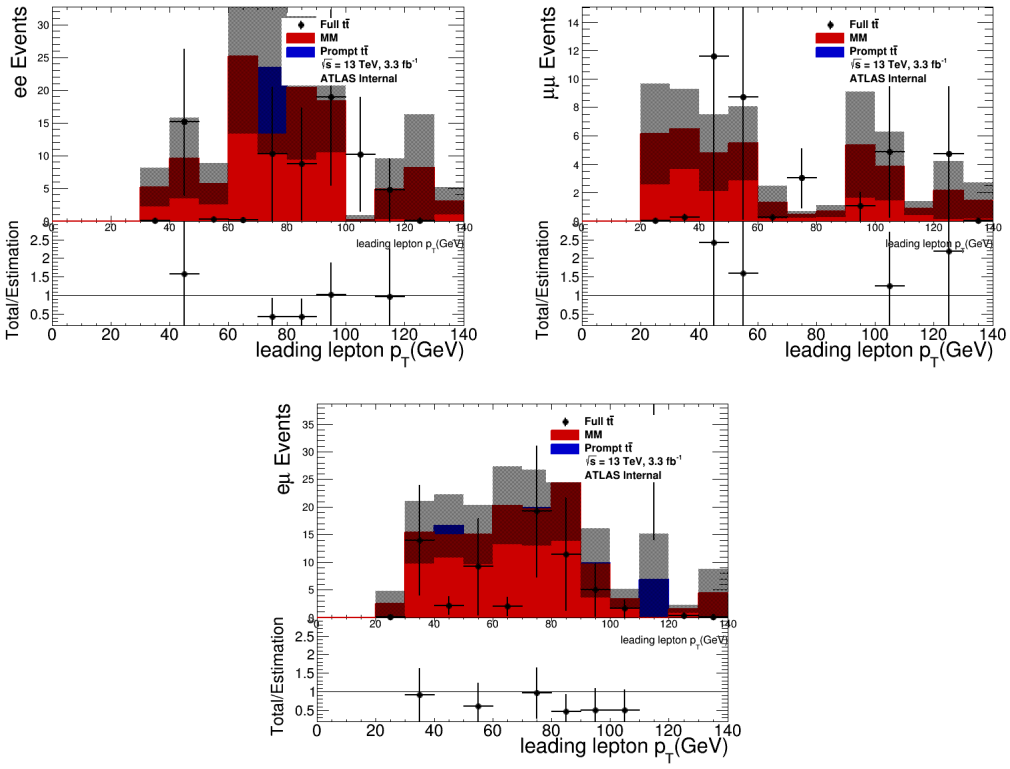

Figure 6.8: "Closure test" of the matrix method application as a function of the leading lepton p_T, made using ϵ_r and ϵ_f calculated in the low-N_{jet} control region. Efficiency calculation and test are performed on the $t\bar{t}$ MC sample composed of dileptonic and semileptonic events. Prompt $t\bar{t}$ refers to dileptonic prompt events selected using the MC generator truth. The selection used in this test is the one used for the signal region.

6.5.2 Matrix Method test

The data-driven fake and real efficiencies have been applied to the $\sim 3.25\, fb^{-1}$ low-N_{jet} control region to test the method. Loose lepton counting is performed using muons selected without the isolation requirement. Efficiencies produced with all methods are tested: figure 6.9 contains the matrix method background estimation made with efficiencies calculated in the low-N_{jet} CR, while figure 6.10 contains the same estimation made using the single lepton CR's. The first ϵ estimations provide a better match with data in the low-p_T region, while the behaviour looks worse in the high-p_T region, although here statistical uncertainties play a bigger role.

Similarly to the solution used in Run I, the matrix method is applied also by selecting events that have any number of muons that do not pass the *isolation* working point but exactly 2 muons that pass this cut. This should ensure that we have the same event multiplicity as the standard selection, but we can still apply the MM to all the muons in the event. The results of this test are shown in figure 6.11. This simple implementation improves the results in most p_T bins, but not by a significant margin, considering the large statistical uncertainty.

Although the matrix method still shows large fluctuations due to the available statistics on a bin-per-bin basis, it shows results compatible with the tests performed. Once, thanks to the increased luminosity acquired in 2016, the significance becomes higher and shape histograms become more significant, it is going to be used as the main estimation technique for non-prompt leptons.

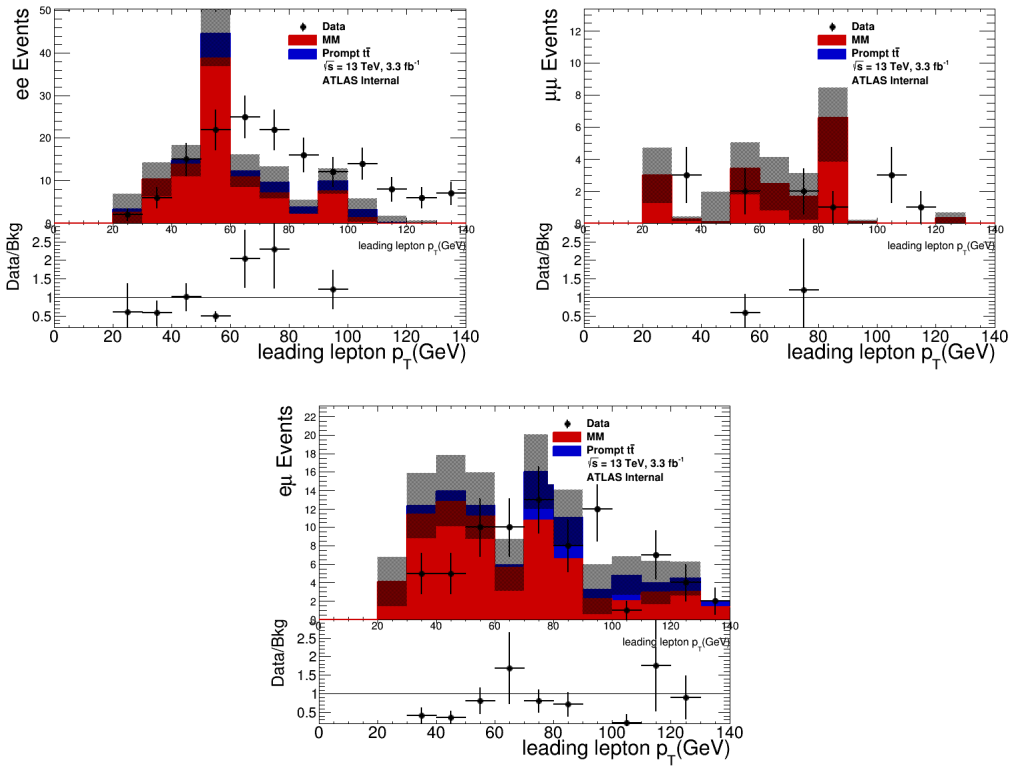

Figure 6.9: Test of the matrix method application as a function of the leading lepton p_T, made using ϵ_r and ϵ_f calculated in the low-N_{jet} control region. Efficiency calculation and test are performed on the full data sample gathered by ATLAS in 2015. Prompt $t\bar{t}$ refers to dileptonic prompt events selected using the MC generator truth and rescaled to the appropriate luminosity.

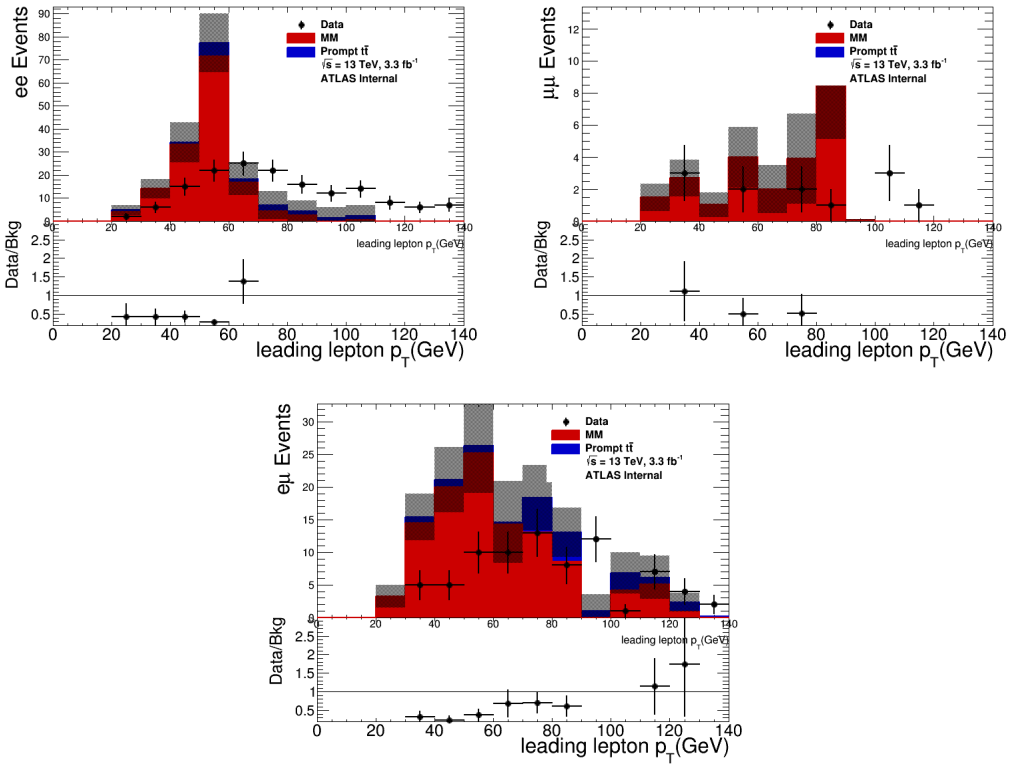

Figure 6.10: Test of the matrix method application as a function of the leading lepton p_T, made using ϵ_r calculated in the Z-peak CR and ϵ_f calculated in the single-lepton CR's. The test is performed on the full data sample gathered by ATLAS in 2015. Prompt $t\bar{t}$ refers to dileptonic prompt events selected using the MC generator truth and rescaled to the appropriate luminosity.

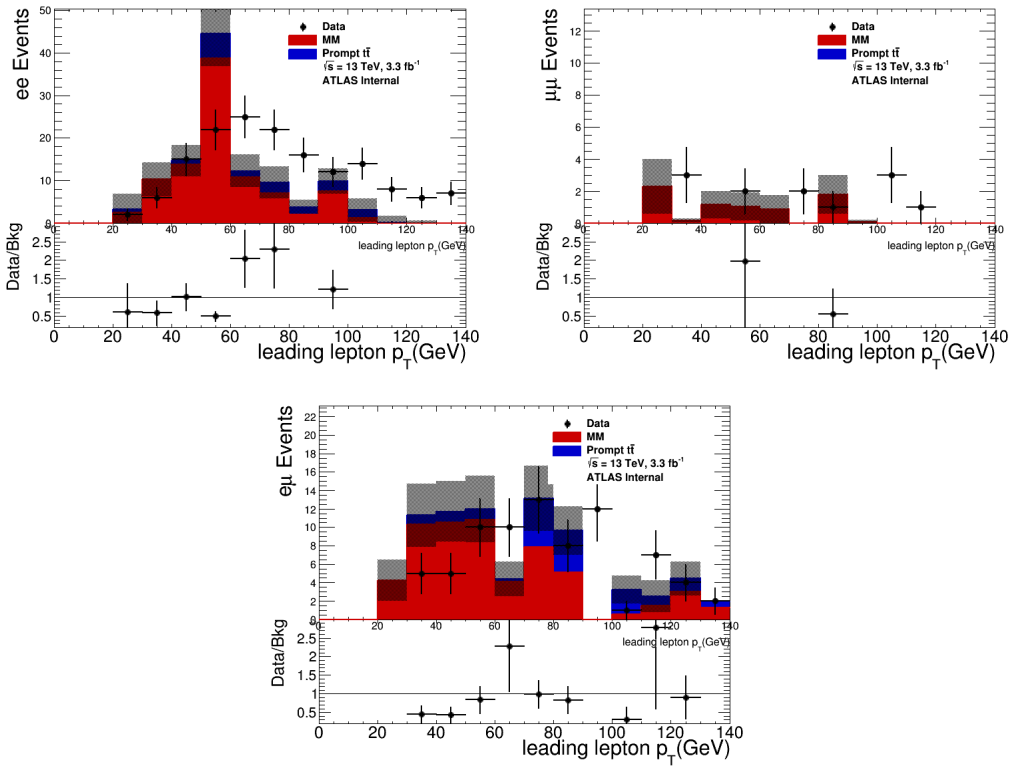

Figure 6.11: Test of the matrix method application as a function of the leading lepton p_T, made using ϵ_r and ϵ_f calculated in the low-N_{jet} CR. The test is performed on the full data sample gathered by ATLAS in 2015. The Matrix method is performed on all the lepton couples of events with exactly two leptons passing the standard preselection. The difference is that extra muons passing all the cuts except isolation are also considered.

Conclusions

This thesis presents the work I carried on within the ATLAS collaboration during the period of my Ph.D. at the Bologna University in collaboration with the Bologna INFN group and the CERN research center.
The main topic of the thesis is the study of the most recent addition to the Standard Model, the Higgs boson. The importance of the Higgs boson from a theoretical and experimental point of view was explained in detail, with particular attention to the study of the top Yukawa coupling in the $t\bar{t}H$ production channel.
The Large Hadron Collider and the ATLAS experiment are the unique tools that allow these studies. The main principles of particle acceleration and detection and the experimental set-up were described to introduce the system capabilities and limitations. The main Higgs-related phenomenology at particle physics experiments and ATLAS in particular was described.
An important addition to this study is the analysis of the decay into multi-leptonic final states, which was described in detail with a particular focus on the channel with two leptons of the same sign and no hadronic taus in the final state. A signal strength $\mu = \sigma_{2lSS0\tau,data}/\sigma_{2lSS0\tau,SM} = 2.8^{+2.1}_{-1.9}$ is measured from this channel alone, showing an excess from the Standard Model expected value, albeit of small significance due to the low statistics available. The combination of all the multi-leptonic analysis channels improves this result, yielding a signal strength $\mu = \sigma_{data}/\sigma_{SM} = 2.1^{+1.4}_{-1.2}$. This value is still compatible with the Standard Model hypothesis and poses an upper limit at 95% confidence level on the signal strength of $\mu < 4.7$, indicating that with a 95% probability the cross-section is lower than 4.7 times the SM expectation.
The analysis was extended using a different method to estimate the background produced

in the $2lSS0\tau$ channel by the leptonic decay of hadrons inside jets. This *matrix method* is important because it allows for the production of background shapes as a function of any kinematic or topological variable. This characteristic is essential for shape and multivariate analyses. The method implementation is explained in detail and the results in the signal regions are shown as a function of the particle transverse momentum and the number of jets. Using these results for background estimation, I obtain a new value for the signal strength: $\mu = 0.8 \pm 2.1$. This result is closer to the SM expectations than the signal strength previously shown. The 95% CL limit $\mu < 4.6$ is posed for this channel.
The preliminary analysis of the 2015 Run II data was also described, focusing again on the $2lSS0\tau$ channel and the background estimation using the matrix method. The tests performed show a good behaviour in the test regions and on MC simulations, ensuring that the method is ready for the signal region un-blinding and, even more important, for the 2016 data taking, that should see a significant increased in acquired luminosity.

Appendices

Appendix A

Luminosity with Z boson counting

The Z boson was introduced in chapter 1 as part of the EW theory and was shown to acquire a mass thanks to the SM EW symmetry breaking mechanism. The particle was discovered [32] at the SPS accelerator at CERN by the UA1 collaboration and provided the Nobel Prize to C. Rubbia and S. van der Meer. With a neutral charge and a mass of $91.2\,GeV$, it decays in l^+l^- and $q\bar{q}$; using its leptonic decay channels, the mass can be precisely reconstructed, providing a very clean signature that can be used as a standard reference process in performance studies.

This appendix describes the measurement of the Z boson production cross section $\times$ $BR_{\mu\mu}$ separately in each of 29 selected runs of the 2012 data taking of the ATLAS experiment, searching for the process $pp \to Z \to \mu\mu$; aim of the analysis is the study of some of the systematics of the official ATLAS luminometers (see chapter 2). The runs were selected to be representative of the full data-taking, covering a period of 7 months, for an integrated luminosity of $L_{int} = 3679.7pb^{-1}$.

The first part of the appendix describes the selection procedure used in these measurements and the results obtained with this selection. The second part describes the luminosity measurement procedure using boson counting and some of the systematic uncertainties studied this way: time drift of the luminometers and dependence on the number of interactions per bunch-crossing (μ-dependence).

A.1 Luminosity

Luminosity (see chapter 2) is a running parameter of any collider accelerator that depends on beam current, transverse size of the proton beams and the overlap between the two beams. The beam current is determined by the number of bunches in the beam, the number of protons in each beam and the frequency of LHC. This is resumed in the formula of instantaneous luminosity:

$$L = \frac{f_{LHC} \sum_{i=1}^{k_B} N_{1i} N_{2i}}{2\pi\sigma_x\sigma_y}, \tag{A.1}$$

where f_{LHC} is the revolution frequency of an LHC bunch, k_B is the number of packages, $N_{1/2i}$ is the number of protons in the i bunch and $\sigma_{x/y}$ are the beam spreads along the transversal axes.

To the experimental physicist, instantaneous Luminosity is correlated to the production rate (R) observed for a particular process together with its cross section (σ): $L = R/\sigma$. If we are interested in the number of processes that happen over a particular time-span, we integrate the instantaneous Luminosity as $L_{int} = \int L dt$. This quantity is used in the cross-section measurements: $L_{int} = N/\sigma$.

We define the average number of interactions per bunch-crossing $< \mu >=< N_{int}/BC >_{LB}$ (over a luminosity block). This quantity is directly proportional to the instantaneous luminosity averaged over a lumi-block $< L >_{LB} = < \mu > N_{collBCID} f/\sigma_{pp}$, where σ_{pp} is the total inelastic cross section, f is the bunch crossing frequency of $40\,MHz$ and $N_{collBCID}$ is the number of filled colliding BCID's.

Luminosity in ATLAS is measured with a redundant approach [28], so that if one of the measurements fails the others can provide Luminosity or at least identify the magnitude and reason of the problem. Thanks to this we compare the luminosity measured using the nominal detectors with several other methods and detectors. In Figure A.1 the variations with respect to a reference run are computed. A good agreement is obtained between the off-line measurements and Calorimeter measurements, while we observe a drift in luminosity measured with respect to BCM and LUCID. This study confirms the need of the luminosity correction as a function of time applied in the luminosity analysis [28].

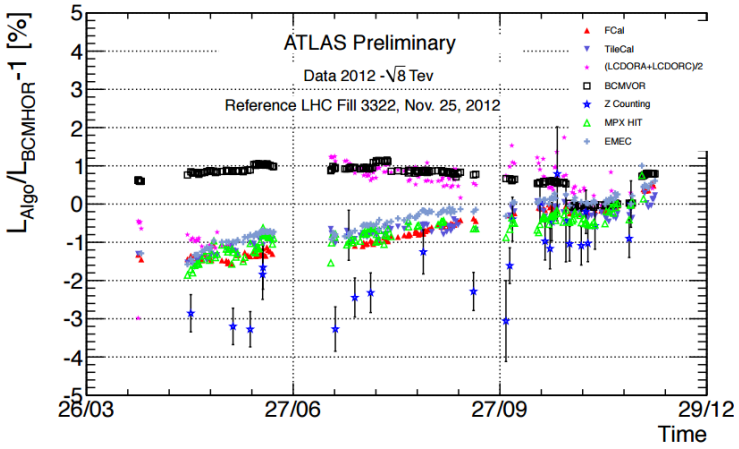

Figure A.1: Comparison of the luminosity measured with several methods to the ATLAS reference luminosity measurement. The comparison is displayed as a function of the day when the run was acquired.

A.1.1 Measurement through physics channels

Luminosity can be measured using standard physics processes and the $Z \to \mu\mu$ counting is optimal for this role, thanks to the clean signature and the high statistics at LHC. The advantage of using a physical process is that these are intrinsically more robust to μ-dependence and free from time-effects, since they are reconstructed using a greater number of sub-detectors, and don't incur in algorithm saturation, since the probability of multiple simultaneous processes is very low. Luminosity can, moreover, be measured lumi-block per lumi-block to verify the linearity of the detectors' measurements with μ. To measure the full integrated luminosity (over a LB) it is necessary to measure:

$$L^{Z}_{int,LB} = \frac{N - N_{bkg}}{A_Z C_Z \sigma^{th}_Z}, \tag{A.2}$$

where A_Z and C_Z are the acceptance and selection efficiency of the Z bosons and the σ^{th}_Z is the Z production theoretical cross-section.

A.2 Analysis procedure

The Z boson is produced at LHC at leading order in $q\bar{q}$ annihilation, where the $\bar{q}$ comes is from the virtual sea. The $Z \to \mu\mu$ decay has a branching ratio of $(3.366 \pm 0.007)\%$, but in the di-muon signal it has the lowest background contamination of all the decay channels. The first step of the analysis procedure is to remove a good part of the background without reducing the signal in a significant way. Afterwards it is necessary to evaluate the efficiency of the acceptance of the selection and the remaining background. At this point it is possible to measure the cross-section as a function of the run number and compare this measurement with the theoretical calculation. The analysis can, then, be used for luminosity studies.

A.2.1 Event and object selection

Events are selected using single muon triggers with a p_T threshold of $24\,GeV$ in case of isolated muons and $36\,GeV$ for non-isolated ones. A primary vertex cut is applied selecting events with at least two tracks reconstructed in the inner detector at a distance from the primary vertex along the beam line lower than $10\,mm$. The muons are required to be reconstructed with the *staco combined* algorithm [98], that uses both the muon spectrometer and the inner detector tracks, to be isolated and to have a transverse momentum $p_T > 25\,GeV$ for the leading lepton and $p_T > 20\,GeV$ for the secondary one. A cut on pseudo-rapidity $\eta < 2.4$ is applied to remove the detector regions where muon reconstruction gets worse.
Events with exactly two opposite sign muons are selected and a final invariant mass (M_{cand}) is reconstructed. If $66\,GeV < M_{cand} < 116\,GeV$, the event is considered to contain a Z boson and is used for luminosity studies.

A.2.2 Acceptance and efficiency

As from equation A.1.1, the theoretical cross section and the official ATLAS luminosity. Since these are absolute values, the determination of efficiency and acceptance is essential to measure the luminosity with Z-counting. In this section we also study the dependence of the selection efficiency on the average number of interactions per bunch

crossing ($< \mu >$), which can improve our understanding of the relative, LB per LB, measurements.

The calculation of A_Z and C_Z is made using the signal Monte Carlo Pythia Poweg [70] at 8 TeV using a theoretical cross-section of 1120 pb and the MRST [99] LO PDF set. Table A.1 shows this and the other generators used for signal and background. All of them are interfaced with Photos [100] to simulate the effect of final state QED radiation. The interaction of the particles produced in the final state of the process with the ATLAS detector is simulated using GEANT4 [78]. The fiducial acceptance is considered to be

Physics process	Generator	$\sigma\cdot$ BR [nb]	
$W^+ \to \mu^+\nu$	PowHegPythia8	6.89±0.34	NNLO
$W^- \to \mu^-\bar{\nu}$	PowHegPythia8	4.79±0.24	NNLO
$Z/\gamma^* \to \mu\mu$ $(m_{\ell\ell} > 60$ GeV)	PowHegPythia8	1.11±0.06	NNLO
$W^+ \to \tau^+\nu$	PowHegPythia8	6.89±0.34	NNLO
$W^- \to \tau^-\bar{\nu}$	PowHegPythia8	4.79± 0.24	NNLO
$Z/\gamma^* \to \tau\tau$ $(m_{\tau\tau} > 60$ GeV)	PowHegPythia8	1.11±0.06	NNLO
$t\bar{t}$	Mc@Nlo	$0.152^{+0.011}_{-0.015}$	≈NNLO
WW	Herwig	0.0124± 0.0006	NLO
WZ	Herwig	0.00367±0.00026	NLO
ZZ	Herwig	0.00099±0.00005	NLO
$b\bar{b}$ (μ channel, $\hat{p}_T > 18$ GeV, $p_T(\mu) > 15$GeV)	Pythia8	198.98	LO
$c\bar{c}$ (μ channel, $\hat{p}_T > 18$ GeV, $p_T(\mu) > 15$ GeV)	Pythia8	80.088	LO

Table A.1: Monte Carlo generators and PDF's used in the analysis.

$|\eta| < 2.4$ and $p_T > 10\,GeV$ for both muons. These cuts are applied on the Monte Carlo truth, producing an acceptance $A_Z = 0.4164 \pm 0.0001$ (stat).

The efficiency (trigger, reconstruction and cuts) of the Z selection C_Z is calculated run per run using trigger and isolation Scale Factor (SF) corrections specific to each run (the MC simulation is always the same). These are used to take into account the mis-modelling of MC and the small variations in the detector behaviour specific to each run and data-taking period. SF's are measured using a tag and probe technique [101] on data specifically for each run because this is necessary when studying a run-by-run dependence of the cross-section. As a consequence, different C_Z values are used in each run.

C_Z is also calculated as a function of $< \mu >$ in order to study the dependence on μ of the luminosity measured with equation A.1.1. Figure A.2 shows the variation of the

selection efficiency with $< \mu >$ for a specific run (left) and of the average efficiency for the 29 analysed runs (right). The dependence on μ is taken from a representative run, but all the other runs show a similar dependence. Since the MC simulation is always the same, the difference among the C_Z values among runs solely depends on the scale factors and reflects the different μ-ranges and trigger and detector effects.

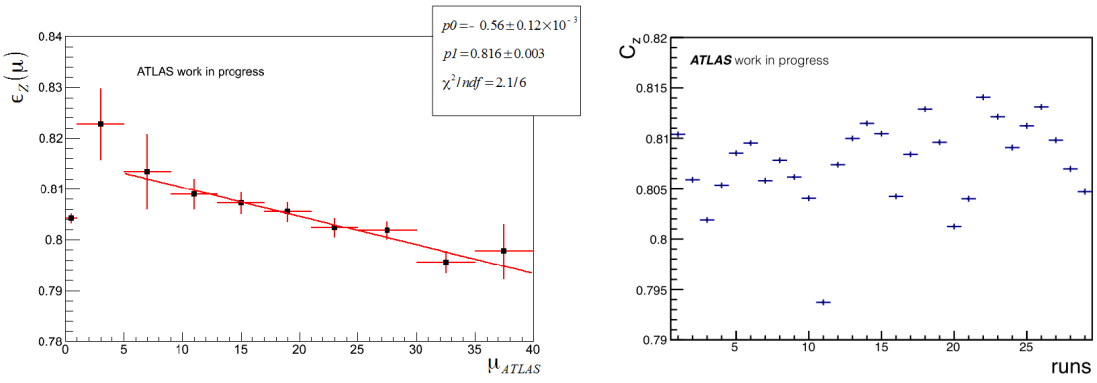

Figure A.2: Selection efficiency measured as a function of $< \mu >$ in a sample run (left). The first bin represents the average value for the run. C_Z is also measured as a function of the run observed (right).

A.2.3 Background

The background of the $Z/\gamma* \rightarrow \mu\mu$ channel is mainly due to dibosonic, $t\bar{t}$ and QCD multi-jet, each producing a dilepton signal, as shown for two sample runs in figure A.3. The shapes are produced using MC simulations for all backgrounds except QCD, for which a template fit is used, where the background shape is taken from MC and the normalization is taken from the fit of the real data. N_{bkg} is calculated by integrating the background shapes in the mass range $66\,GeV < M_{cand} < 116\,GeV$, producing an average 0.51% value. The variation between runs is found to be negligible.

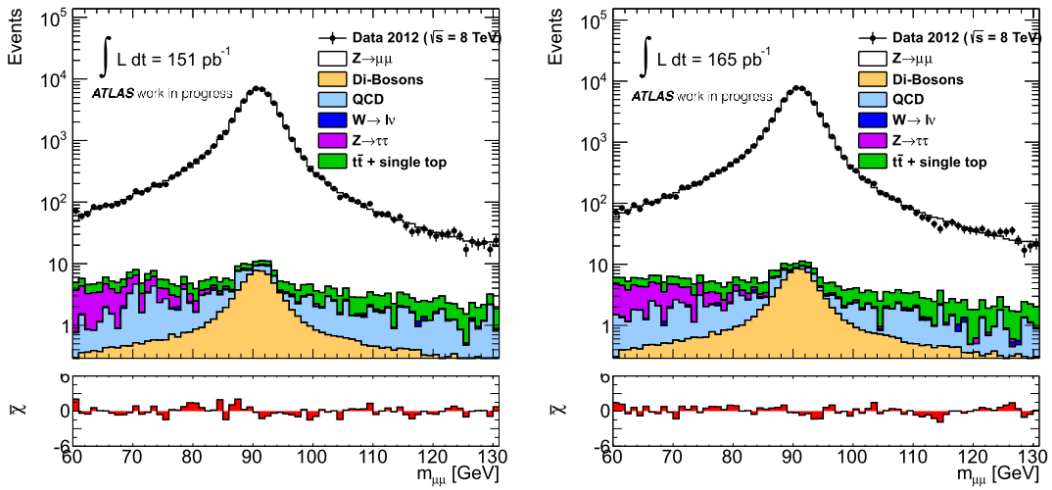

Figure A.3: Two sample runs where the main background distributions are displayed as a function of the invariant dileptonic mass M_{ll}.

A.2.4 Systematic uncertainties

Systematic uncertainties don't play a crucial role in this analysis, as they are used only to test the significance of the difference between the measured and the theoretical Z cross-sections. Table A.2 shows the main sources of systematic uncertainty considered in this work. The reconstruction uncertainties are provided by the detector performance group, while efficiency systematics were produced in this analysis by varying the Scale Factors by $\pm 1\sigma$. The remaining uncertainties are extrapolated form the 2010 analysis [102] results. In the following the uncertainty on luminosity determination is not taken into account, since its study is among the aims of the present study.

A.2.5 Cross section measurement

The measurement of the cross section is essential to study the properties of the Standard Model and in particular of the Electroweak theory. Since the Z cross section at LHC is well understood, we can use the theoretical calculation for luminosity measurement and correlated values to study the performance of algorithms, detectors and sub-detectors.

	δN_Z
Muon trigger efficiencies	0.9
Muon reconstruction efficiencies	0.5
Muon isolation efficiencies	0.4
Muon p_T resolution	0.3
Muon p_T scale	0.03
QCD background	0.3
Electroweak+$t\bar{t}$ background	0.1
Pile-up modeling	0.3
Vertex position	0.1
C_Z theoretical uncertainty	0.3
Total experimental uncertainty	1.2
$A_{W/Z}$ theoretical uncertainty	2.0
Total excluding luminosity	2.3
Luminosity	3.9!!!

Table A.2: Main relative systematic uncertainty sources in the $Z \to \mu\mu$ analysis.

The cross section is measured using the formula:

$$\sigma = \frac{N - N_{bkg}}{L_{int} C_Z A_Z}, \tag{A.3}$$

where L_{int} is the integrated luminosity as provided by the ATLAS luminosity measurement, which was BCM for the 2012 data-taking, integrated over the whole run and N_{bkg} is the number of background events. The cross-section $\times$ branching ration(BR) measurement is performed run by run and compared in Figure A.4 with the same measurement performed using $C_Z(\mu)$ and the theoretical cross section. Although C_Z does depend on the $< \mu >$ value, the impact of this dependence on a whole run is mitigated since the different runs span approximately the same $< \mu >$ range. On the other hand, a dependence on time is already clear and requires additional studies, performed in the next section.

A.3 Luminosity measurement

In figure A.5 we show the luminosity as a function of the LB number for one of the 29 runs considered, measured using equation A.1.1 and displaying only statistical uncertainties. The beam degradation with time is clearly visible.

The total run per run integrated luminosity measured this way is shown in Figure A.6

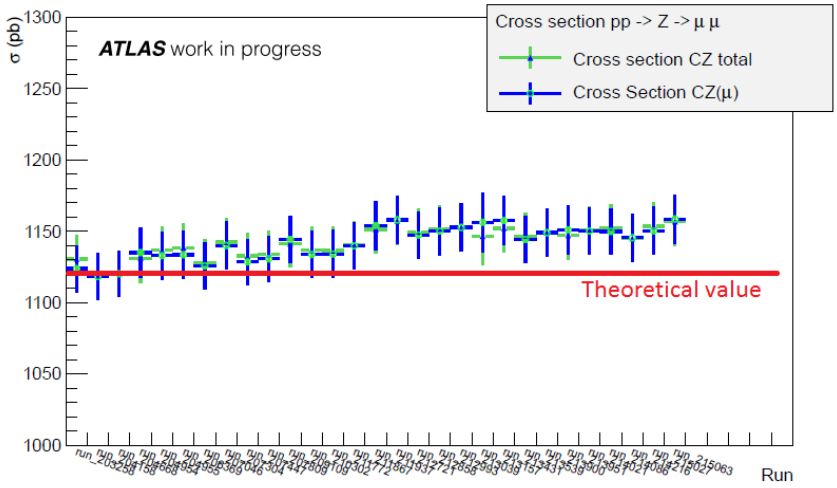

Figure A.4: Cross section $\sigma(pp \to Z \to \mu\mu)$ measured run-by-run using C_Z averaged over all values of $< \mu >$ and as a function of $< \mu >$.

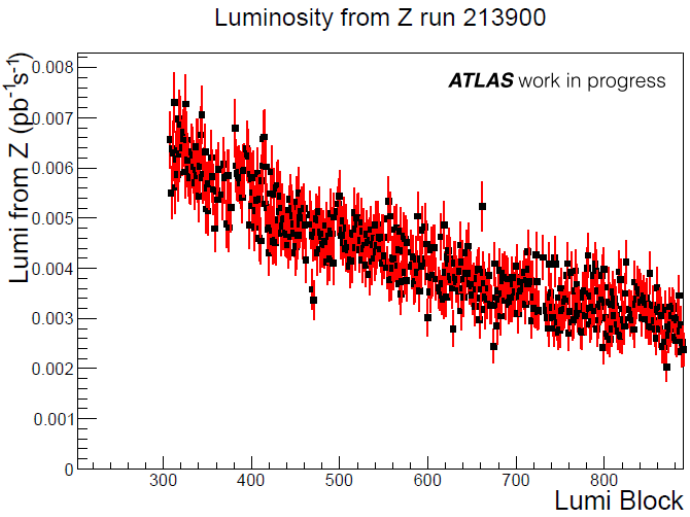

Figure A.5: Integrated luminosity, measured LB by LB using $C_Z(\mu)$ in teh sample run through Z counting, for a total of $134\,pb^{-1}$.

and can now be compared with the measurements taken with the reference detectors, which for most of the ATLAS Run I was the Beam Condition Monitor (BCM).

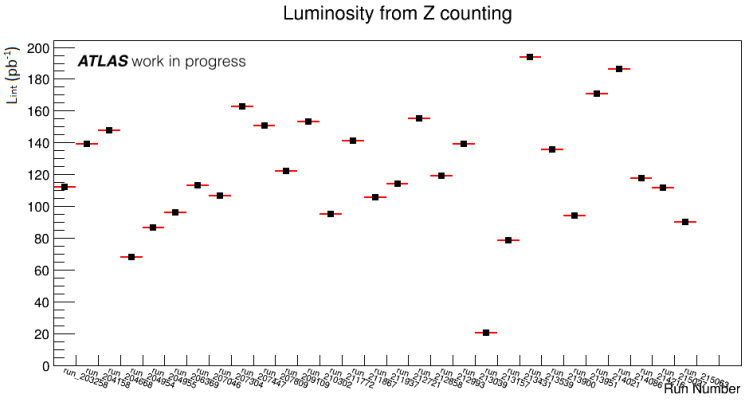

Figure A.6: Integrated luminosity, measured through Z counting for the 29 runs using $C_Z(\mu)$.

A.3.1 Luminosity measurement uncertainties

We can use these luminosity values calculated using the $Z \to \mu\mu$ channel to study two of the most important luminosity systematics: time-dependence and mu-dependence.

Time dependence

Studies made using different detectors and algorithms have shown that the Luminosity measurement is not constant with time (see figure A.1), due to a degradation of the BCM performance, that might get damaged or loose efficiency during the data-taking, due to the exposure to high radiation. Since the $Z \to \mu\mu$ physical channel is by definition not time-dependent and the performance of the different detectors used for muon detection and reconstruction is well understood, we can use it as an instrument to verify the BCM drift. Figure A.7 shows the relative difference between $L_{int,Z}$ and $L_{int,BCM}$, with only statistical errors displayed. From May to October we observe a time-drift effect of 2-3% , that partially confirms previous evaluations using different techniques [28].

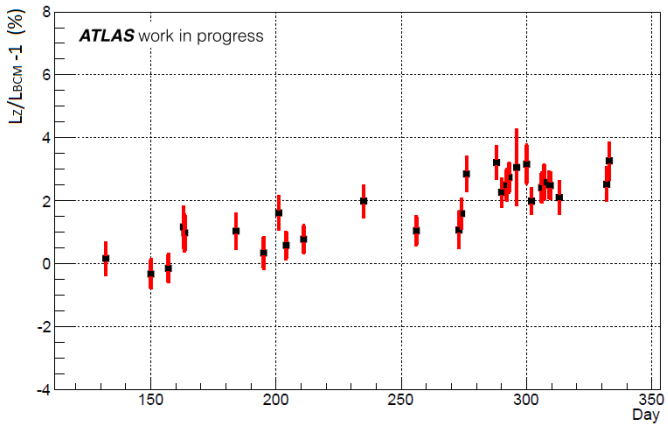

Figure A.7: Comparison of the luminosity measured with Z counting and by the BCM, ATLAS reference luminosity measurement. The comparison is displayed as a function of time.

μ-dependence

The analysis procedure uses refined reconstruction techniques and optimized selections to isolate the process of interest from any background. Luminosity detectors cannot do the same and could be influenced by the number of secondary interactions, called *pile-up*. Moreover, the saturation of the luminosity algorithms could lead to a loss in performance. The average number of interactions $< \mu >$ and its effect on luminosity detectors can be asserted using physics channels, intrinsically less dependent from it. Again, $Z \rightarrow \mu\mu$ is the ideal process to accomplish this.
We compare μ from Z counting with the same quantity as measured by BCM, as a function of μ_{BCM}. This is studied first on a run-per-run basis using a profile histogram[1] and then summing the contributions of all runs. In figure A.8 this comparison is shown two sample runs. No visible μ-dependence is observed within the statistical uncertainty.

When grouping all of the 29 selected runs, a new aspect must be taken into consideration: the time dependence might have an impact on this long-term μ-dependence

[1] In a profile histogram the bin values correspond to the average of the inputs in the bin range and the error corresponds to the deviation from the average.

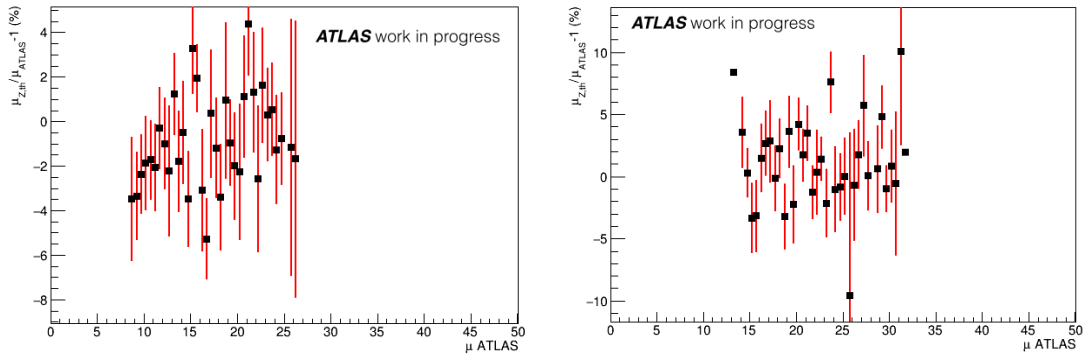

Figure A.8: $\Delta\mu_Z/\mu_{BCM}$ measured as a function of $< \mu >_{BCM}$ in two sample LHC runs gathered by the ATLAS experiment. The distributions are still dominated by the statistical uncertainty.

estimation, since later LHC runs tend to have a higher average $< \mu >_{run}$. Because of this, two measurements were performed, shown in figure A.9: one that uses all 29 runs (left) and one that uses only a restricted number of runs (right), selected as spanning the same range of average $< \mu >$. Both studies show a weak μ-dependence. In particular, in the second approach, which is the one that ensures the least biased result, the μ-dependence is compatible with 0 within 2 standard deviations. The result is therefore compatible with no μ-dependencein the BCM measurement.

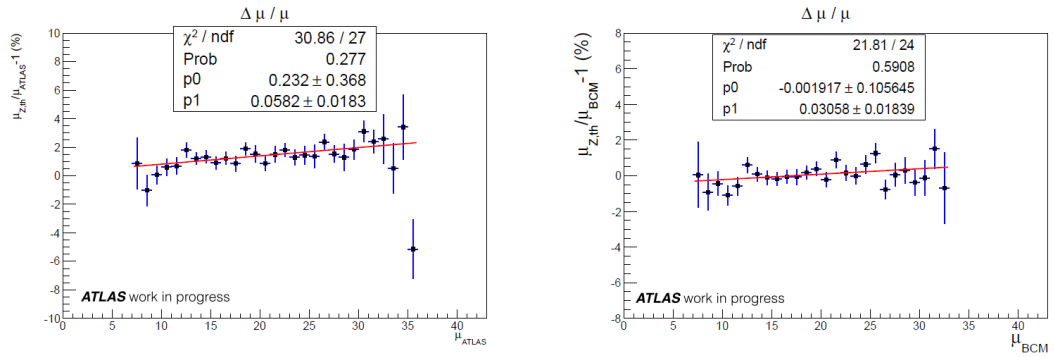

Figure A.9: $(\mu_Z - \mu_{BCM})/\mu_{BCM}$ measured as a function of μ_{BCM} in two sample LHC runs gathered by the ATLAS experiment.

Conclusions

In this appendix the luminosity measurement using the counting of Z boson events was described, starting from the analysis procedure and arriving to the study of the luminosity systematic uncertainties: time-drift and μ-dependence of the ATLAS preferred luminosity algorithm. A time-dependence of the ATLAS luminosity measurement of the order of $2-3\%$ is observed, confirming the indication given by the calorimeter luminosity measurement A.1. The dependence of the measurement on the average number of interactions per bunch crossing was also studied, decoupling it from the time-dependence. The deviation from the ATLAS value was shown to be small, compatible with 0 within $< 2\sigma$.

Appendix B

LUCID detector Run II upgrade

The measurement of luminosity is essential in any high-energy physics experiment for cross-section measurements. In ATLAS luminosity is measured on several levels and at different steps of the data-taking and data re-processing:

- online luminosity monitoring performed by the dedicated detectors, integrating signal over the short time-span $\Delta t \sim 1 - 2\,s$; only the fast hardware response of the luminosity algorithms used by the dedicated detectors can provide this measurement without significant delay;
- lumi-block by lumi-block luminosity, integrated over a time span during which the instantaneous luminosity is estimated to be approximately constant; this leads to a Δt that varies around $30 - 60\,s$;
- offline luminosity, measured by reprocessing data using more refined calibrations; this measurement can be performed using a great number of detectors and algorithms, providing a redundant approach.

Since the start of the Large Hadron Collider, LUCID (Luminosity Cherenkov Integrating Detector) has been the only dedicated luminosity monitor in the ATLAS experiment [19] [27], although other measurements have been used to compute luminosity algorithms, as shown in chapter 2 and appendix A. The intrinsically fast response of the Cherenkov detectors and the dedicated readout electronics make it ideal to measure the number of interactions at each bunch crossing.

In this section the LUCID for the ATLAS Run II is described. I worked on the upgrade of the detector, from development to installation and testing, focusing mainly on the firmware of the LUMAT board and the optical communication with the LUCROD board.

B.1 LUCID in Run I

LUCID [103] is and was made of two modules placed around the beam-pipe on both forward ends of ATLAS, at around $17\,m$ from the interaction point. Each side of the LUCID I, the detector used in Run I, is comprised of a conical aluminium vessel housing 20 mechanically polished aluminium tubes pointing to the interaction point. Each tube contains a photomultiplier tube (PMT).
The aluminium vessel is a gas tank filled with C_4F_{10}, a high refractive index ($n = 1.00137$, at standard temperature and pressure) Cherenkov radiator gas kept at a pressure of about $1.1\,bar$. When a charged particle enters a tube, Cherenkov light is emitted at an average angle of 3 degrees with respect to the particle trajectory. The light undergoes multiple reflections on the aluminium walls till it reaches the tube end. In 16 out of the total 20 tubes, the light is collected by a photomultiplier directly coupled with the tube. The others 4 tubes end up in a small aluminium cone concentrating the light on a fibre bundle ($5\,m$ long) that in turn brings the light to a lower radiation area, where a multianode photomultiplier reads out the signals. During the last part of the data-taking, the gas was removed because of the low performance, in particular due to the signal migration induced by the photon reflections in the tube. The ten-dynode PMT's produced by Hamamatsu, model R762, are configured with different resistances and different applied voltages to minimize the current while still providing the ability to detect the single photon.
The electronic system of LUCID I is composed of an array of amplifiers followed by constant fraction discriminators (CFD), where signals above threshold produce a *hit*. These CDF's are placed far from the PMT's ($\sim 100\,m$), requiring amplification and, thus, broadening the signal. The hit array is then sent to the LUMAT board, where the luminosity algorithms are performed combining the two sides of the detector. The algorithms are stored in dedicated VME registers that are read by the software data

acquisition (DAQ) system via VME communication.

B.2 LUCID in Run II

With the end of the Run I data-taking, it became immediately clear the LUCID required an upgrade before Run II, denominated LUCID II. There were several reasons for this:

- replacing damaged and useless hardware, in particular the empty gas tanks and the old PMT's, that had already sustained high currents and radiation doses;
- reducing the acceptance of the detector, so that when LHC provides high luminosity the algorithms do not saturate, loosing sensitivity;
- improving the response of the system with new electronics to implement a different acquisition and processing strategy, necessary to face the new running conditions and to obtain more information to plan further upgrades.

Each module of LUCID II is composed of 16 photomultipliers (PMT's) close to the beam-pipe and 4 quartz fibre bundles read by PMT's in a shielded location, as shown in Figure B.1. The PMT's detect charged particles crossing their quartz window, where Cherenkov light is produced. Light is produced in the fibres as well and carried to PMT's sitting behind shielding a few meters away [104]. A new calibration system for the PMT's allows frequent on-line calibration to compensate for possible yield variations due to ageing. A system of temperature probes and a cooling apparatus ensure that all the components are kept at the ideal working temperature.

A new electronic system reads and processes the detector data at the LHC clock frequency of $40\,MHz$, performing luminosity algorithms and preparing the results for the ATLAS data stream and the online luminosity monitoring.

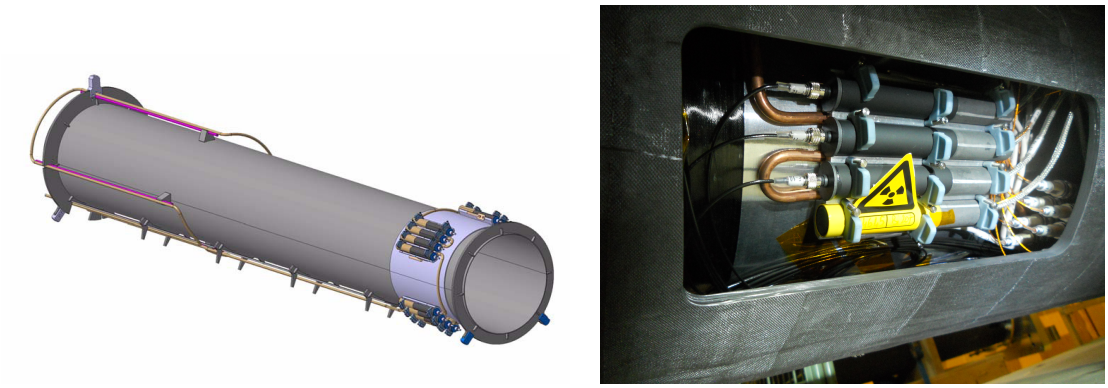

Figure B.1: The structure of one of the two sides of the active part of the LUCID II detector (left) and a real image on the PMT area (right), showing 4 PMT's installed there

B.2.1 Photomultiplier tubes

LUCID II uses R760 Hamamatsu PMT's, a smaller version of the previously used R762 model, shown in figure B.2. The new PMT's have been tested for gamma and neutron radiation hardness, ensuring stable results in ATLAS until 2018. Out of the

Figure B.2: Two images of the R760 PMT's in its modified form, showing the circular aluminium layer that reduces the active area and, thus, the acceptance

20 PMT's per side (thus including fibres), only 16 are switched on at any given time, leaving 4 inactive as a backup. The active ones are divided into 4 groups of 4 that are treated independently:

- *Bi207* bismuth-calibrated PMT's,

- *standard* LED-calibrated PMT's,
- *modified* PMT's, where an aluminium circular crown was deposited inside the quartz window to reduce the acceptance,
- *fibre* PMT's, reading the 4 fibre bundles.

All of the luminosity algorithms are applied to the 4 groups independently. The *Bi207* and *standard* PMT's are acquired by a full electronic system and the *modified* and *fibre* PMT's are processed by an identical independent system.

B.2.2 PMT Calibration

PMT calibrations have been performed with the goal of finding a good working point at low gain, to reduce the current produced in the PMT, thus reducing their ageing. The calibrations were accomplished using Bi-207 sources, that produce monochromatic electrons from internal conversion, which produce Cherenkov light with a spectrum similar to the one expected for particles in ATLAS. Shown in figure B.3 is the amplitude spectrum of the Bi-207 source as recorded by the new PMT's. A clear separation between signal and noise can be observed.

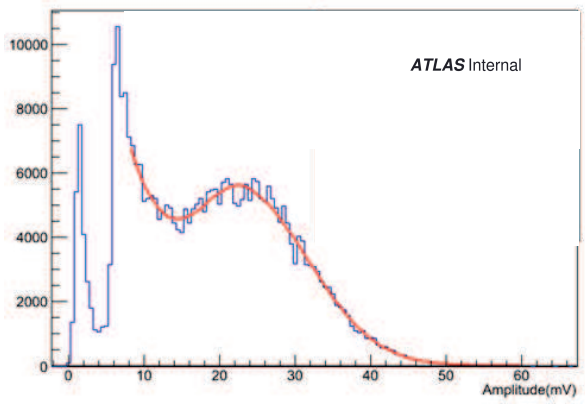

Figure B.3: Amplitude spectrum from a Bi-207 source using a R760 Hamamatsu PMT, with the baseline clearly visible to the left.

During operation, the PMT gain calibration is monitored by a redundant system made of:

- optical fibres carrying LED signals;
- optical fibres carrying LASER signals provided by the calibration system of the Tile calorimeter;
- radioactive sources (Bi - 207), with the advantage that these produce a more realistic Cherenkov signal with respect to LED input.

Optical fibre calibration is used for 12 PMT's per side, including the modified ones, and for the 4 fibre PMT's. 4 PMT's per side are, instead, equipped with the radioactive source.

B.3 Electronics

The old LUCID electronics could not fully cope with the 25 ns bunch-spacing, since the electronic front-end system was far from the detector, resulting in pulses with tails beyond the 25 ns. Early signal digitization performed by new front-end electronics placed next to the PMT's avoids this effect.
The electronic system is, thus, composed of two different boards: the first that acquires the data and starts processing it and a second that receives the data from both sides of the detector and combines the information to measure luminosity.
Both boards store their output on registers that are read through the VME interface by the TDAQ software.

B.3.1 The LUCROD board

The LUCROD boards are new VME boards, placed close to the detector, that perform early signal digitization as well as PMT-charge integration over each bunch crossing time (25 ns), together with a first set of luminosity algorithms.
The LUCROD board is a 9U VME custom board featuring 16 analog lemo input channels connected to PMT's and control pin diodes, 16 analog lemo outputs for the amplified signal, 4 digital lemo input/output connectors for debugging purposes and two optical link transceivers. On the board each channel is connected to a low noise amplifier

and a 320 MHz Flash Analog-to-Digital Converter (FADC), which is used for charge digitization. Eight "channel" Cyclone IV FPGAs (one every two input channels) receive the input signals and perform several tasks:

- Charge accumulation, per BCID, over each Luminosity Block (charge is evaluated as the integral of the digitized signal over one BCID period, which is 25 ns, or 8 samples in the current implementation) ;
- Hit discrimination; whenever the digitized signal exceeds a programmable threshold, a "hit" is counted;
- Hit counting, per BCID, over each Luminosity Block;
- Signal storage in 64-samples-deep FIFO's, readable via VME for signal shape monitoring

Separate thresholds and amplification factors are set for each input in order to reduce the noise and optimize the signal gain. Two "communication" FPGA's manage the communication protocols with the VME connector, used by the TDAQ software, and the optical link to the LUMAT. At every bunch crossing, the pattern of over-threshold PMT's, the "hits", is sent to the LUMAT board via optical link communication. Samples of the input signals can be collected for monitoring purposes, too. All FPGA's operate at the 40 MHz LHC clock rate, except for the section dedicated to the acquisition of the FADC's.
Optical communication is handled by a transceiver that operates at a clock frequency of 50 MHz, sending the serialized words coming from the communication FPGA denominated "V". Inside the FPGA, the optical communication is handled by the *OptoLinkInterface* block and in particular by the *ElasticBuffer* entity.
The *ElasticBuffer* entity contains the interface between clock domains; the 32-bit input hit patterns are written synchronously with the main experiment clock (40 MHz) inside a true dual-port First-In First-Out (FIFO); the words are read at the 50 MHz clock generated from the transceiver PLL. In order to balance the read/write clock slack, an almost-empty/-full logic introduces special padding words starting with a k28.5 character (a special control sequence of the 8b/10b protocol). These control sequences placed in the data-flow are also used to align the byte boundaries on the receiver counterpart.

The built-in transceiver is able to manage words with a maximum width of 16 bits, so a word chopper is used, running at twice the elastic buffer read clock speed. The Data-out bus, running at 100 MHz, moves data from this entity towards the sub-entity responsible for data serialization and it directly drives the optical transceiver towards the LUMAT board. The system also receives data in the same way, a function that can be used to get feedback to the board. The optical fibre link has a speed of 2 Gbit/s (40 bits at 50 MHz).

The luminosity algorithms performed are single-channel hits, two OR of the channel hits (event and hit counting) and charge integration of the two channels present on the FPGA. These are read via VME protocol through the board backplane and stored for luminosity conversion. Figure B.4 shows two of the luminosity algorithms performed by the LUCORD board: single-channel hit counting (left) and total collected charge integration (right). The samples are taken from a physics run and are displayed as a function of the Bunch Crossing ID (BCID), integrated over the Lumi-Block.

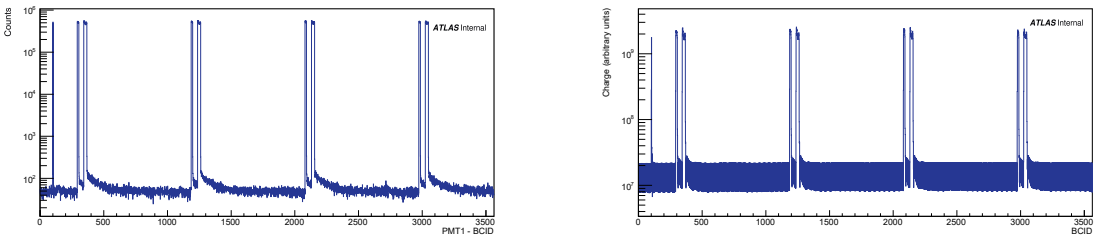

Figure B.4: LUCROD PMT-1 hit counts (left) as a function of bunch crossing number a selected LB taken from physics runs; the constant background is given by the calibration Bi-207 source. The sum of the charges (right) collected by the 4 PMT's calibrated using Bi-207 in the same LB, as a function of the BCID.

B.3.2 The LUMAT board

The LUMAT boards are 9U VME boards developed by the Bologna INFN research team, shown in figure B.5 to be composed by:

1 A 9U motherboard, featuring connectors for the VME bus and the FPGA (Cyclone II) used to manage the bus communication protocol.

2 A main mezzanine based on a Stratix II (Altera) FPGA, with 1508 pins, placed in the middle of the board, entitled with the task of managing incoming data from EPMC's and handling the subsequent elaboration stages. This board is the most important part of the elaboration process of the information received from the LUCROD boards.

3 Two mezzanine boards called EPMC (Edro Programmable Mezzanine Cards) host a couple of Spartan VI (Xilinx) FPGA's, which manage bidirectional optical channels. These boards are used to receive data sent from the LUCROD boards using the 8b/10b protocol implemented in the FPGA's. The input connectors of the board are characterized by four optical fibre links; input bit-rate is 25 Gbit/s, while the total input/output rate is 12.4 Gbit/s.

4 A S-Link LSC (Link Source Card) mezzanine is used both to transmit elaborated data towards subsequent PC acquisition stages and to record data on disk using a clock optical link (40 MHz) able to send 160 MByte/s.

5 A small TTCrq mezzanine receives global signals at $40\,MHz$ clock, used also to correct the board's clock phase and synchronize it with the LHC clock.

The board is entitled with the task of combining data from the two detector sides to produce on-line and off-line luminosity measurements. The resulting patterns are sent to the main FPGA mounted on the board, a Stratix II, for luminosity algorithm implementation.

In the EPMC mezzanines the de-serialized words are sent to the two (one is for backup) Xilinx Spartan VI FPGA's, where the alignment is performed:

- bit alignment locks the incoming signal to the correct bit starting point;
- word alignment uses the extra words to locate the beginning bit of the words in each data stream and removes them to bring the clock back to the reference LHC $40\,MHz$ clock; in the case of mis-ordered words, a rearranging operation is performed;

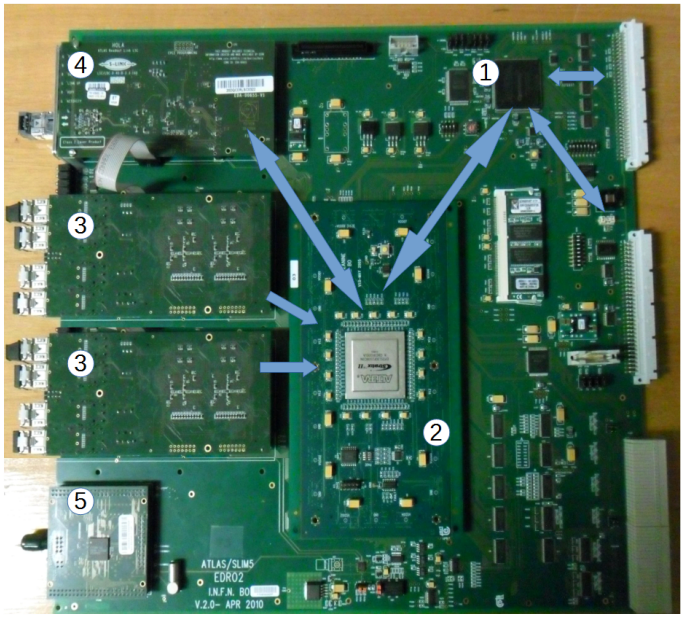

Figure B.5: All of the components of the LUMAT board

- stream alignment synchronizes the two data streams using a dedicated "orbit" bit, which marks the start of the first bunch crossing; the streams are stored in two shift registers that are read starting from the element containing an "orbit" bit with value 1.

A set of quality and debug words is stored in the VME registers, counting the number of successful and failed alignments, as well as the BCID distance between the "orbit" signals from the two sides (see figure), ensuring accurate quality assessment and quick problem solving.

An important part of the FPGA code consists in a random hit pattern generator, which is configured through VME registers to reproduce particular beam structures with variable degrees of intensity and randomization. This entity is essential to test new features and components without the necessity for detector input, that is available mostly during physics runs that cannot be disrupted by hardware tests. The EPMC mezzanine communicates with the Stratix II FPGA on the main board through a Hamming code that ensures single error correction and double error detection.

Algorithm	Function	Hits
EventOR	OR	≥ 1/side
EventAND	AND	≥ 1/side
EventORA	OR	≥ 1 on side A
EventORC	OR	≥ 1 on side C
HitOR	OR	sum hits on any side
HitAND	AND	sum hits on any side
Single Channel	-	-

Table B.1: The SM Higgs boson production cross sections or $m_H = 125\,GeV$ in pp collisions, as a function of the centre of mass energy, $\sqrt{s}$ [51]

The main Stratix II FPGA decodes the incoming hit and control patterns and selects the stream coming from the appropriate EPMC and FPGA, since a total four input streams are connected to it. A *SpyBuffer* entity stores the last hit patterns received, making them accessible for VME read-out to get an immediate visual feedback of the hit behaviour. Twelve different algorithms are performed in the *Algorithm* entity using the hit patterns received from the LUCROD boards, 6 per PMT type (two types) received by each LUMAT board, with 16 additional single-channel algorithms available for debugging and specific measurements through VME configuration, as shown in table B.1. The used set of algorithms is established through database configuration at the start of the data-taking.

Every algorithm is performed as a function of the BCID and is processed in parallel at every clock tick, storing it in the FPGA RAM blocks thanks to operation pipe-lining: read the old value for the bin, add the algorithm value to it, store the updated value. This way each bin is integrated over the LB, at the end of which they are frozen and read through the VME interface; at the same time a loss-less swapping function to a new algorithm array allows to immediately start the data-taking for the new incoming LB. Each algorithm also has a version integrated over both all BCID's and the LB and another version integrated over BCID's but only on a shorter Δt. This latter measurements are read by the ATLAS software to provide online luminosity monitoring. An example of the

luminosity algorithm histograms produced by the LUMAT board is displayed in figure B.6, taken from a 2015 physics run.

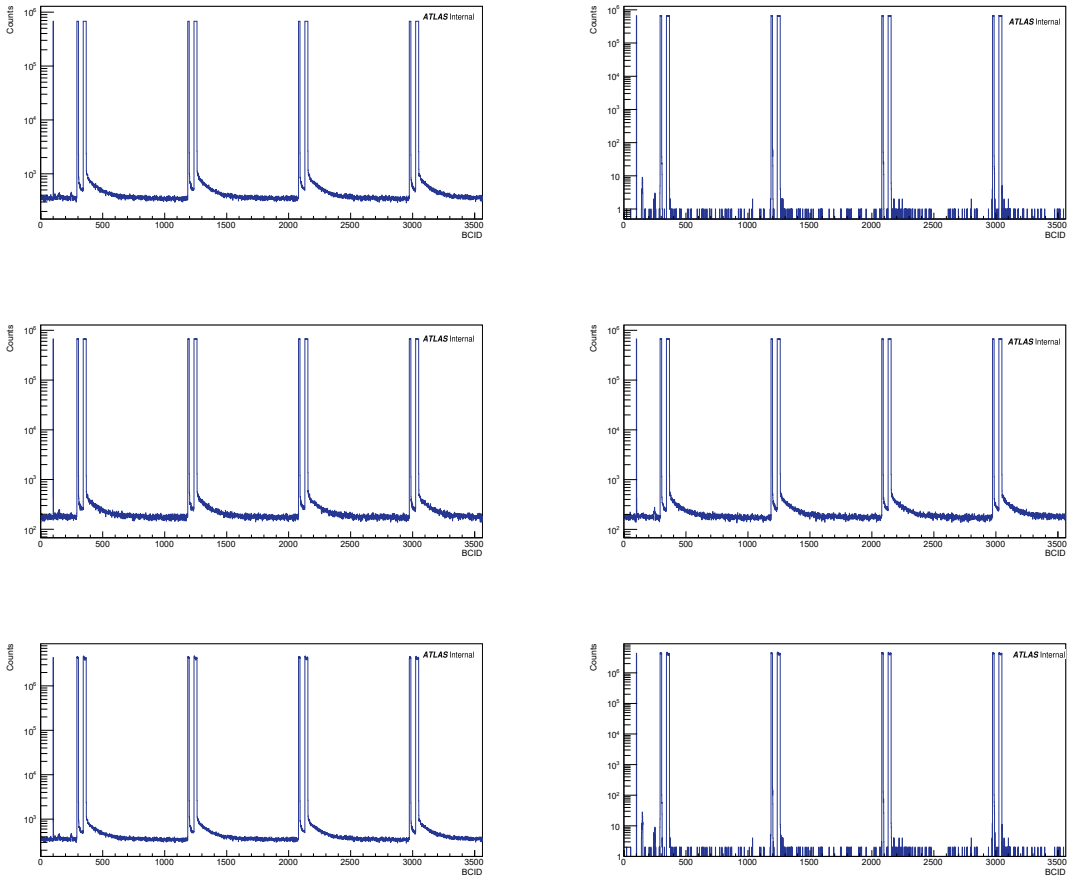

Figure B.6: The output of the luminosity algorithms detailed in table B.1, in the same order, for the LUCID *Bi-207* PMT's. The counts are measured as a function of the BCID number inside the same LB.

B.3.3 Data acquisition software

The Trigger and Data Acquisition (TDAQ) is the system that manages the interface with the hardware. It is composed of:

- databases and configuration files;

- a graphical user interface (GUI) for control and monitoring;
- a main state machine that manages protocols and plug-ins;
- a series of protocols an plug-ins that manage the configuration procedures (VME protocol), hardware out-put read-out, monitoring and storage.

Hereby we focus only in the part more closely related to my work, which is the communication with the electronic boards.
The LUMAT and LUCROD boards have a large number of 32- and 16-bit registers dedicated to VME communication. In these registers, the data words can be stored and read by the software and firmware. To configure the boards, the configuration words are written by the software on the dedicated registers (via VME protocol), which are in turn read immediately by the firmware. During runs, the firmware stores the processed results in the dedicated registers, making it available for the software to read in periodic polling or after a user input. The reading can be done addressing a specific register of through block transfer of an array of registers.
The software decodes the register contents and translates them to meaningful signals, such as performance numbers and results, in numeric and graphical form.

B.4 LUCID calibration

The LHC was turned on after the shut-down period in April and LUCID successfully registered the first events, showing its ability to measure luminosity on a bunch-by-bunch basis. In August 2015 the luminosity calibration using the Van der Meer scans technique was performed, as explained in chapter 2. Figure B.7 shows the scan shape as measured by the LUCID detector, together with the background processes involved.

The calibration (see section 2.9) uncertainties are the main contributions to the uncertainties in luminosity determination: table B.2 summarizes the main contribution to the systematic uncertainty on luminosity measurements. A 3.8% uncertainty is assigned to the van der Meer calibration based on the August 2015 scans. The largest contributions arise from the precision of the length scale calibration determined by measuring

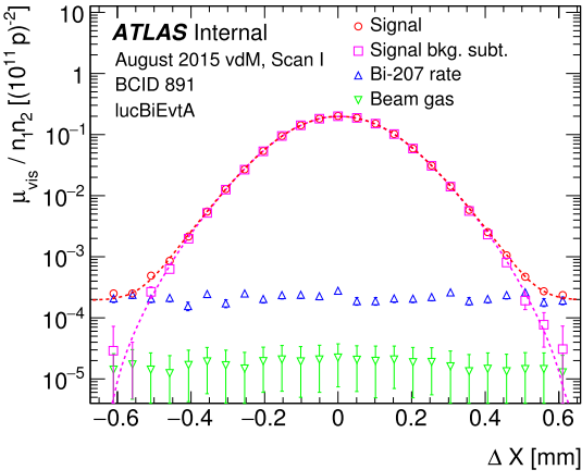

Figure B.7: Visible interaction rate for the LUCID algorithm LUCORD *Bi-207* EventAND, that provides the ATLAS luminosity, in one bunch crossing and per unit bunch population, versus nominal beam separation during horizontal scan 1 in the August 2015 luminosity-calibration session. The background is dominated by random counts from the radioactive Bismuth source used for phototube gain calibration (blue triangles), as estimated from the rate measured in the preceding unfilled bunch slot. The background subtracted rate is fitted by a Gaussian multiplied by a sixth-order polynomial (dashed curve). The error bars are statistical only.

the displacement of collision vertices reconstructed in the inner detector, the estimation of potential non-factorisation biases during beam-separation scans, the scan-to-scan reproducibility of the visible cross sections of the LUCID algorithms, orbit drifts measured by the beam position monitors during the scans and corrections for beam-beam effects. Sources of uncertainties leading to sub-percent errors, such as the bunch population product (0.3%) are not listed in the table, but are included in the total uncertainty. A 3.2% uncertainty is assigned to the luminosity monitoring throughout the data taking. This error is dominated by the run-to-run consistency of luminosity measurements comparing LUCID bunch-by-bunch rates, bunch-average particle flux monitoring in the calorimeters and track counting in the inner detector. Another significant component is the estimated upper limit on the calibration transfer correction, i.e. the change of the LUCID response between the low-luminosity regime of van der Meer scans and the high-luminosity data taking conditions.

Source	Uncertainty [%]
van der Meer calibration	3.8
Dominant components:	
Length scale calibration	2.1
Non-factorisation effects	2.0
Scan-to-scan reproducibility	1.4
Orbit drifts	1.2
Beam-beam effects	1.0
Luminosity monitoring	3.2
Dominant components:	
Run-to-run consistency	2.5
Calibration transfer	2.0
Total luminosity uncertainty	5.0

Table B.2: Total uncertainty on the preliminary luminosity determination in the 2015 proton-proton dataset at $\sqrt{s} = 13\,TeV$.

B.5 Integrated luminosity

The LUCID counting algorithms need to be converted to a luminosity measurement. This conversion is different for every kind of algorithm used [105]. The average instan-

taneous luminosity in each bunch L_b can be written as:

$$L_b = \frac{\mu_{vis} f_r}{\sigma_{vis}}, \tag{B.1}$$

where (defining ϵ as the efficiency at detecting an inelastic pp collision) $\mu_{vis} = \epsilon\mu$ is the average number of visible inelastic interactions per BC, $\sigma_{vis} = \epsilon\sigma_{inel}$ and f_r is the revolution frequency of each bunch (fixed by the accelerator parameters). Once σ_{vis} is measured through calibration, we need to convert the counting algorithm outputs to μ_{vis} to measure luminosity. In event-counting algorithms we get:

$$\mu_{vis} = -\ln\left(1 - \frac{N_{OR}}{N_{BC}}\right), \tag{B.2}$$

where N_{OR} is the number of countings obtained using the OR algorithm in a given Δt and N_{BC} is the total number of crossings registered in the BCID in analysis in the same Δt. The formula is exact only for OR algorithms. For hit-counting algorithms, instead, the following equation applies:

$$\mu_{vis}^{HIT} = -\ln\left(1 - \frac{N_{HIT}}{N_{BC} N_{CH}}\right), \tag{B.3}$$

where N_{HIT} is the number of registered hits and N_{CH} is the number of detector channels used for the algorithm. The formula is a rough approximation, because it doesn't take into account the correlations between hits.

The integrated luminosity measured by the LUCID detector is compared with the measurement of other detectors to test the stability of all luminometers in 2015. The calorimeter (Tile, FCal, EMEC) and track counting algorithms are cross-calibrated to a LUCID measurement of the integrated luminosity in a reference fill, as shown in figure B.8.

Future Developments and Conclusions

The main features of the LUCID detector are fully functional and have already proven to be working correctly. New features and improvements are under development to provide better linearity of the luminosity measurements and additional information to the ATLAS detector.

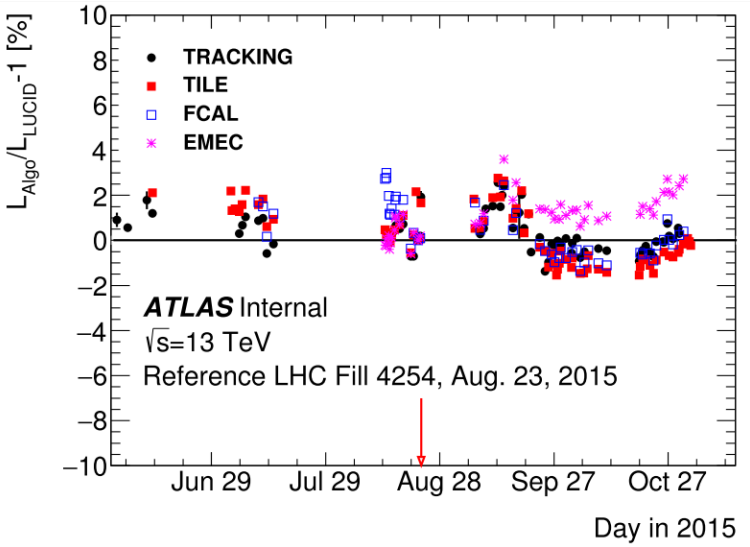

Figure B.8: Run-to-run stability of ATLAS luminometers for the 2015 proton-proton dataset at $\sqrt{s} = 13\,TeV$, excluding dedicated low luminosity data taking periods. Each point shows the mean fractional difference in integrated luminosity for a single ATLAS run, between the indicated algorithm and the reference LUCID luminosity algorithm.

Since the start of the 2015 data-taking, LUCID has been the official ATLAS luminosity monitor, thanks to its precise measurements, its fast response and its reliability, obtained through an intrinsically fast and redundant system, continuous calibration, fast electronics and functional control systems. We expect it to remain essential throughout the whole Run II data-taking thanks to the continuous work put into it by the LUCID team.

Bibliography

[1] F. Halzen and A.D. Martin, *Quarks and leptons: an introductory course in modern particle physics*. Wiley, 1984.

[2] S. Braibant, G. Giacomelli, and M. Spurio, *Particelle e interazioni fondamentali: Il mondo delle particelle*. UNITEXT, Springer, 2012.

[3] R.P. Feynman and A.R. Hibbs, *Quantum Mechanics and Path Integrals*. International series in pure and applied physics, McGraw-Hill, 1965.

[4] Sheldon L. Glashow, "Partial-symmetries of weak interactions," *Nuclear Physics*, vol. 22, no. 4, pp. 579 – 588, 1961.

[5] Jeffrey Goldstone, Abdus Salam, and Steven Weinberg, "Broken symmetries," vol. 127, p. 965, Aug 1962.

[6] F. Englert and R. Brout, "Broken symmetry and the mass of gauge vector mesons," *Phys. Rev. Lett.*, vol. 13, p. 321, 1964.

[7] Peter W. Higgs, "Broken symmetries and the masses of gauge bosons," *Phys. Rev. Lett.*, vol. 13, p. 508, 1964.

[8] ATLAS Collaboration, "Observation of a new particle in the search for the Standard Model Higgs boson with the ATLAS detector at the LHC," *Phys. Lett. B*, vol. 716, p. 1, 2012.

[9] P. de Aquino, *Beyond Standard Model Phenomenology at the LHC*. PhD thesis, Université Catholique de Louvain, 2012.

[10] S. P. Martin, "A Supersymmetry primer," 2010.

[11] Plank Collaboration, "Planck 2013 results. XVI. Cosmological parameters," *Astron. Astrophys.*, vol. 571, p. A16, 2014.

[12] V. C. Rubin and W. K. Ford, Jr., "Rotation of the Andromeda Nebula from a Spectroscopic Survey of Emission Regions," *Astrophysical Journal*, vol. 159, p. 379, Feb. 1970.

[13] R.D. Peccei and H. R. Quinn, "CP Conservation in the Presence of Instantons," vol. 38, pp. 1440–1443, 1977.

[14] J. Elias-Miro, et al., "Higgs windows to new physics through d=6 operators: constraints and one-loop anomalous dimensions," *JHEP*, vol. 1311, p. 066, 2013.

[15] O. S. Bruning, et al., "LHC Design Report," Tech. Rep. CERN-2004-003, CERN, 2004.

[16] European Organization for Nuclear Research, "LEP design report," Tech. Rep. CERN-LEP-84-01, 1984.

[17] K. Kleinknecht, *Particle Detectors.* Physics reports, North-Holland Publishing Company, 1982.

[18] W.R. Leo, *Techniques for Nuclear and Particle Physics Experiments: A How-To Approach.* Springer-Verlag, 1994.

[19] ATLAS Collaboration, "The ATLAS Experiment at the CERN Large Hadron Collider," vol. 3, p. S08003, 2008.

[20] ATLAS Collaboration, *ATLAS magnet system: Technical Design Report, 1.* Technical Design Report ATLAS, Geneva: CERN, 1997.

[21] ATLAS Collaboration, "ATLAS inner detector: Technical design report. Vol. 1," 1997.

[22] M. Aharrouche, "The ATLAS liquid argon calorimeter: Construction, integration, commissioning and combined test beam results," *Nucl.Instr.Meth. A*, vol. 581, p. 373, 2007.

[23] M.S. Alam et al., "Atlas pixel detector: Technical design report," Tech. Rep. CERN-LHCC-98-13, CERN, 1998.

[24] P. Adragna, et al., "The ATLAS hadronic tile calorimeter: From construction toward physics," *IEEE Trans.Nucl.Sci.*, vol. 53, p. 1275, 2006.

[25] B. Dowler et al., "Performance of the ATLAS hadronic end-cap calorimeter in beam tests," vol. A482, p. 94, 2002.

[26] A. Artamonov, et al., "The ATLAS forward calorimeters," *JINST*, vol. 3, p. P02010, 2008.

[27] ATLAS Collaboration, "Improved luminosity determination in pp collisions at $\sqrt{s} = 7$ TeV using the ATLAS detector at the LHC," *Eur. Phys. J.*, vol. C73, no. 8, p. 2518, 2013.

[28] ATLAS Collaboration, "Luminosity Determination in pp Collisions at $\sqrt{s} = 8$ TeV using the ATLAS Detector at the LHC." arXiv[hep-ex]1302.4393, 2015.

[29] ATLAS Collaboration, "Measurement of the total cross section from elastic scattering in pp collisions at $\sqrt{s} = 7$ TeV with the ATLAS detector," *Nucl. Phys. B*, vol. 889, p. 486, 2014.

[30] UA1 Collaboration, "Experimental observation of isolated large transverse energy electrons with associated missing energy at $\sqrt{s} = 540$ GeV," *Physics Letters B*, vol. 122, p. 103, 1983.

[31] UA2 Collaboration, "Observation of single isolated electrons of high transverse momentum in events with missing transverse energy at the CERN pp collider," *Physics Letters B*, vol. 122, p. 476, 1983.

[32] UA1 Collaboration, "Experimental observation of lepton pairs of invariant mass around 95 GeV/c^2 at the CERN SPS collider," *Physics Letters B*, vol. 126, p. 398, 1983.

[33] D0 Collaboration, "Observation of Single Top Quark Production," *Phys. Rev. Lett.*, vol. 103, p. 092001, 2009.

[34] CDF Collaboration, "First Observation of Electroweak Single Top Quark Production," *Phys. Rev. Lett.*, vol. 103, p. 092002, 2009.

[35] Thomas Schucker, "Higgs-mass predictions." arXiv[hep-ph]0708.3344, 2007.

[36] Benjamin W. Lee, C. Quigg, and H. B. Thacker, "Weak interactions at very high energies: The role of the Higgs-boson mass," *Phys. Rev. D*, vol. 16, p. 1519, Sep 1977.

[37] Dario Buttazzo, et al., "Investigating the near-criticality of the Higgs boson," *JHEP*, vol. 12, p. 089, 2013.

[38] European Organization for Nuclear Research, "LEP design report: Vol.2 The LEP Main Ring," Tech. Rep. CERN-LEP-84-01, CERN, 1984.

[39] TeVI Group, "Design Report Tevatron 1 project," 1984.

[40] A. Ferroglia, et al., "Simple formulae for $\sin^2\theta_{\rm eff}^{\rm lept}$, M_W, Γ_l, and their physical applications," *Phys. Rev. D*, vol. 65, p. 113002, 2002.

[41] ALEPH Collaboration, DELPHI Collaboration, L3 Collaboration and OPAL Collaboration, "Search for the standard model higgs boson at lep," *Nucl. Phys. B*, vol. 565, p. 61, 2003.

[42] CDF and D Collaborations, "Updated combination of cdf and d searches for standard model higgs boson production with up to 10.0 fb^{-1} of data." arXiv:1207.0449, 2012.

[43] Henning Flacher, et al., "Revisiting the Global Electroweak Fit of the Standard Model and Beyond with Gfitter," *Eur. Phys. J.*, vol. C60, p. 543, 2009. [Erratum: Eur. Phys. J.C71,1718(2011)].

[44] Ringaile Placakyte, "Parton Distribution Functions," in *Proceedings, 31st International Conference on Physics in collisions (PIC 2011)*, Physics in Collisions, 2011.

[45] "HERA - A Proposal for a Large Electron Proton Colliding Beam Facility at DESY," 1981.

[46] Richard D. Ball et al., "Parton distributions with LHC data," *Nucl. Phys. B*, vol. 867, p. 244, 2013.

[47] G. Altarelli and G. Parisi, "Asymptotic freedom in parton language," *Nucl.Phys. B*, vol. 126, p. 298, 1977.

[48] A. D. Martin, et al., "Parton distributions for the LHC," *Eur. Phys. J. C*, vol. 63, p. 189, 2009.

[49] Sayipjamal Dulat, et al., "The CT14 Global Analysis of Quantum Chromodynamics." arXiv[hep-ph]1506.07443, 2015.

[50] W. Beenakker, et al., "NLO QCD corrections to t anti-t H production in hadron collisions," *Nucl. Phys. B*, vol. 653, p. 151, 2003.

[51] K. A. Olive et al., "Review of Particle Physics," *Chin. Phys. C*, vol. 38, p. 090001, 2014.

[52] CMS Collaboration, "Observation of a new boson at a mass of 125 GeV with the CMS experiment at the LHC," *Phys. Lett. B*, vol. 716, p. 30, 2013.

[53] ATLAS Collaboration, "Combined coupling measurements of the Higgs-like boson with the ATLAS detector using up to 25 fb^{-1} of proton-proton collision data," 2013.

[54] J R Andersen et al., "Handbook of LHC Higgs Cross Sections: 3. Higgs Properties," Tech. Rep. CERN-2013-004, FERMILAB-CONF-13-667-T, CERN, 2013.

[55] ATLAS Collaboration, "Search for $H \to \gamma\gamma$ produced in association with top quarks and constraints on the Yukawa coupling between the top quark and the

Higgs boson using data taken at 7 TeV and 8 TeV with the ATLAS detector," *Phys. Lett.*, vol. B740, p. 222, 2015.

[56] ATLAS Collaboration, "Search for the Standard Model Higgs boson produced in association with top quarks and decaying into $b\bar{b}$ in pp collisions at $\sqrt{s} = 8$ TeV with the ATLAS detector," *Eur. Phys. J. C*, vol. 75, p. 349, 2015.

[57] A. Feindt and Universitat Karlsruhe, "A neural bayesian estimator for conditional probability densities." Technical Report,IEKP, 2008.

[58] ATLAS Collaboration, "Search for the associated production of the Higgs boson with a top quark pair in multilepton final states with the ATLAS detector," *Phys. Lett.*, vol. B749, p. 519, 2015.

[59] J. Alwall, et al., "The automated computation of tree-level and next-to-leading order differential cross sections, and their matching to parton shower simulations," *JHEP*, vol. 2014, no. 7, 2014.

[60] JohnM. Campbell and R.Keith Ellis, "$t\bar{t}W^{\pm}$ production and decay at NLO," *JHEP*, vol. 2012, no. 7, 2012.

[61] M.V. Garzelli, et al., "$t\bar{t}W^{\pm} + t\bar{t}Z$ hadroproduction at NLO accuracy in QCD with parton shower and hadronization effects," *JHEP*, vol. 2012, no. 11, p. 56, 2012.

[62] Johan Alwall, et al., "Madgraph 5: going beyond," *JHEP*, vol. 2011, no. 6, 2011.

[63] JohnM. Campbell, R.Keith Ellis, and Ciaran Williams, "Vector boson pair production at the LHC," *JHEP*, vol. 2011, no. 7, 2011.

[64] Michał Czakon and Alexander Mitov, "Top++: A program for the calculation of the top-pair cross-section at hadron colliders," *Computer Physics Communications*, vol. 185, no. 11, p. 2930, 2014.

[65] Y. Li and F. Petriello, "Combining QCD and electroweak corrections to dilepton production in FEWZ," *Phys. Rev. D*, vol. 86, p. 094034, 2012.

[66] Adam Kardos and Zoltán Trócsányi, "Hadroproduction of t anti-t pair with a b anti-b pair using PowHel," *J. Phys. G*, vol. 41, p. 075005, 2014.

[67] Paolo Nason, "A new method for combining NLO QCD with shower Monte Carlo algorithms," *JHEP*, vol. 2004, no. 11, p. 040, 2004.

[68] G. Bevilacqua, et al., "Helac-nlo," *Computer Physics Communications*, vol. 184, no. 3, p. 986, 2013.

[69] Hung-Liang Lai, et al., "New parton distributions for collider physics," *Phys. Rev. D*, vol. 82, p. 074024, 2010.

[70] Torbjorn Sjöstrand, Stephen Mrenna, and Peter Skands, "A brief introduction to PYTHIA 8.1," *Computer Physics Communications*, vol. 178, no. 11, p. 852, 2008.

[71] Jonathan Pumplin, et al., "New generation of parton distributions with uncertainties from global qcd analysis," *JHEP*, vol. 2002, no. 07, p. 012, 2002.

[72] ATLAS Collaboration, "ATLAS tunes of Pythia 6 and Pythia 8 for MC11." ATL-PHYS-PUB-2011-009, ATL-COM-PHYS-2011-744, 2011.

[73] Manuel Bähr, et al., "Herwig++ physics and manual," *The European Physical Journal C*, vol. 58, no. 4, p. 639, 2008.

[74] T. Gleisberg, et al., "Event generation with sherpa 1.1," *JHEP*, vol. 2009, no. 02, p. 007, 2009.

[75] T. Binoth, N. Kauer, and P. Mertsch, "Gluon-induced qcd corrections to pp→ ZZ → $\ell\bar{\ell}\ell'\bar{\ell}'$," in *Proceedings, 16th International Workshop on Deep Inelastic Scattering and Related Subjects*, DIS, 2008.

[76] Peter Z. Skands, "Tuning Monte Carlo generators: The Perugia tunes," *Phys. Rev. D*, vol. 82, p. 074018, Oct 2010.

[77] Michelangelo L. Mangano, et al., "Alpgen, a generator for hard multiparton processes in hadronic collisions," *JHEP*, vol. 2003, no. 07, p. 001, 2003.

[78] S. Agostinelli et al., "Geant4: a simulation toolkit," *Nucl. Instr. Meth. A*, vol. 506, no. 3, p. 250, 2003.

[79] R. E. Kalman, "A new approach to linear filtering and prediction problems," *ASME Journal of Basic Engineering*, 1960.

[80] ATLAS Collaboration, "Performance of the ATLAS Inner Detector Track and Vertex Reconstruction in the High Pile-Up LHC Environment," Tech. Rep. ATLAS-CONF-2012-042, CERN, 2012.

[81] ATLAS collaboration, "Electron efficiency measurements with the ATLAS detector using the 2012 LHC proton-proton collision data." ATLAS-CONF-2014-032, 2014.

[82] ATLAS Collaboration, "Electron reconstruction and identification efficiency measurements with the atlas detector using the 2011 lhc proton–proton collision data," *Eur. Phys. J. C*, vol. 74, p. 2941, 2014.

[83] ATLAS Collaboration, "Measurement of the muon reconstruction performance of the atlas detector using 2011 and 2012 lhc proton-proton collision data," *Eur. Phys. J. C*, vol. 74, p. 3130, 2014.

[84] D C O'Neil, "Tau identification using multivariate techniques in atlas," in *Journal of Physics: Conference Series*, vol. 368, p. 012029, 2012.

[85] ATLAS Collaboration, "Identification and energy calibration of hadronically decaying tau leptons with the atlas experiment in pp collisions at $\sqrt{s} = 8$ tev," *Eur. Phys. J. C*, vol. 75, p. 303, 2015.

[86] Matteo Cacciari, Gavin P. Salam, and Gregory Soyez, "The anti-k_t jet clustering algorithm," *JHEP*, vol. 2008, no. 04, p. 063, 2008.

[87] Matteo Cacciari and Gavin P. Salam, "Dispelling the myth for the jet-finder," *Phys. Lett. B*, vol. 641, no. 1, pp. 57 – 61, 2006.

[88] Matteo Cacciari, GavinP. Salam, and Gregory Soyez, "FastJet user manual," *The European Physical Journal C*, vol. 72, no. 3, 2012.

[89] ATLAS Collaboration, "Calibration of the performance of b-tagging for c and light-flavour jets in the 2012 ATLAS data." ATLAS-CONF-2014-046, 2014.

[90] ATLAS Collaboration, "Improved luminosity determination in pp collisions at $\sqrt{s} = 7$ TeV using the ATLAS detector at the LHC," *The European Physical Journal C*, vol. 73, no. 8, 2013.

[91] Glen Cowan, et al., "Asymptotic formulae for likelihood-based tests of new physics," *The European Physical Journal C*, vol. 71, no. 2, 2011.

[92] CMS Collaboration, "Search for the associated production of the higgs boson with a top-quark pair," *JHEP*, vol. 2014, no. 9, 2014.

[93] ATLAS Collaboration, "Measurement of the top quark-pair production cross section with ATLAS in pp collisions at $\sqrt{s} = 7$ TeV," *Eur. Phys. J.*, vol. C71, p. 1577, 2011.

[94] ATLAS Collaboration, "Search for supersymmetry using final states with one lepton, jets, and missing transverse momentum with the ATLAS detector in $\sqrt{s} = 7$ TeV pp," *Phys. Rev. Lett.*, vol. 106, p. 131802, 2011.

[95] ATLAS Collaboration, "Reconstruction, Energy Calibration, and Identification of Hadronically Decaying Tau Leptons in the ATLAS Experiment for Run-2 of the LHC," Tech. Rep. ATL-PHYS-PUB-2015-045, CERN, Geneva, Nov 2015.

[96] ATLAS Collaboration, "Properties of Jets and Inputs to Jet Reconstruction and Calibration with the ATLAS Detector Using Proton-Proton Collisions at $\sqrt{s} = 13$ TeV," Tech. Rep. ATL-PHYS-PUB-2015-036, CERN, Geneva, Aug 2015.

[97] ATLAS Collaboration, "Tagging and suppression of pileup jets with the ATLAS detector," Tech. Rep. ATLAS-CONF-2014-018, CERN, Geneva, May 2014.

[98] S. Hassani, et al., "A muon identification and combined reconstruction procedure for the ATLAS detector at the LHC using the (MUONBOY, STACO, MuTag) reconstruction packages," in *Proceedings, 10th Pisa Meeting on Advanced Detectors*, Frontier detectors for frontier physics, 2006.

[99] A. Sherstnev and R. S. Thorne, "Parton Distributions for LO Generators," *Eur. Phys. J.*, vol. C55, p. 553, 2008.

[100] Piotr Golonka and Zbigniew Was, "PHOTOS Monte Carlo: A Precision tool for QED corrections in Z and W decays," *Eur. Phys. J.*, vol. C45, p. 97, 2006.

[101] ATLAS Collaboration, *Measurement of the muon reconstruction performance of the ATLAS detector using 2011 and 2012 LHC proton–proton collision data*, vol. C74. 2014.

[102] ATLAS Collaboration, "Measurement of the inclusive $W^{\pm}$ and Z/γ cross sections in the electron and muon decay channels in pp collisions at $\sqrt{s} = 7$ TeV with the ATLAS detector," *Phys. Rev. D*, vol. 85, p. 072004, 2012.

[103] S. Valentinetti, *Luminosity measurements with the LUCID detector in the ATLAS experiment*. PhD thesis, Università di Bologna, 2011.

[104] F. Lasagni Manghi, "LUCID upgrade - ATLAS luminosity monitor for the 2015 LHC," Technology and Instrumentation in Particle Physics, p. 317, PoS, 2014.

[105] G. Cabras, "Luminosity determination for the measurement of the proton-proton total cross-section at 8 TeV in the ATLAS experiment," 2014.